To the Graduate Council:

I am submitting herewith a dissertation written by Robert Daniel Reviere entitled " Ductilization of Single Phase TiAl via Ternary and Quaternary Additions ." I have examined the final copy of this dissertation for form and content and recommend that it be accepted in partial fulfillment of the requirements for the degree of Doctor of Philosophy, with a major in Metallurgical Engineering.

Ben F. Oliver, Major Professor

We have read this dissertation
and recommend its acceptance:

Accepted for the Council:

Associate Vice Chancellor
and Dean of The Graduate School

Ductilization of Single Phase TiAl Via Ternary and Quaternary Additions

A Dissertation

Presented for the

Doctor of Philosophy

Degree

The University of Tennessee, Knoxville

Robert Daniel Reviere

December 1992

ACKNOWLEDGMENTS

The author is indebted to many persons for their help and guidance in the pursuit of this research. He will always be thankful to Dr. and Mrs. Calvin Reviere for their support and guidance.

The author is indebted to the staff in the electronics shop, machine shop, and the secretaries in both the Chemical Engineering and Materials Science and Engineering offices for their help.

He would also like to thank NASA Lewis, Oak Ridge National Laboratories, and the Materials Science and Engineering Department for their financial support of this work. Dr. Ron Noebe, of NASA Lewis, helped in getting the chemical analysis performed. He also was instrumental in getting some of the ingots dropped cast. For this, the author is greatly appreciative.

Mr. Bob McGill's assistance in the SEM examinations was of great help in this research. Discussions with Mr. David Johnson, Mr. Steve Joslin, Mr. Ron Johnson, and Mr. Greg Jones was of great help. Thanks is extended to these persons. Ms. X. F. Chen's electron microscopy work using the ALCHEMI technique was instrumental in the determination of alloying element substitution behavior. Her efforts are greatly appreciated.

Dr. C. Brooks was instrumental in helping decipher some of the results of this thesis. He was also always there to answer any questions and his help is greatly appreciated.

Dr. A. Mathew's was of great help in working out the problems with four point bend testing. The author is greatly appreciative of his help.

Dr. C. McHargue posed many theoretical questions that stimulated the author. For this and his

agreeing to be on the author's committee, the author is very appreciative.

Dr. B. Oliver was instrumental in all aspects of this research. The author is greatly indebted to him for his help, guidance, and support.

ABSTRACT

One goal of this research was to expand the single phase γ-TiAl phase field to lower Al contents by microalloying TiAl with ternary and quaternary additions. This was done to examine whether or not lower Al single phase alloys would have improved ambient ductility. To this end, a series of ternary TiAl based alloys, with additions of Ag, Cr, Ga, Mn, and Zr, were arc melted and homogenized. Based upon this work, Mn and Ga appear to expand the γ phase field to lower Al contents. Zirconium and Cr appear to shift this phase field to higher Al contents. Silver was found to embrittle TiAl. Both Ag and Cr have limited solubility in TiAl. The homogenized microstructures of the ternaries were observed and the number and composition of the phases present determined. This information was used to determine the ternary TiAl phase boundaries at room temperature. These data along with estimates of ternary ambient properties were used to decide which combination of solutes would yield the most promise for quaternary compositions. The main guideline that was followed for all these alloys, was to produce single phase, high purity, low Al content alloys. The properties of the quaternary alloys were compared to the properties for the stoichiometric binary alloy and the binary alloy having the best reported ambient ductility, 48 a/o Al. These quaternaries, as well as the binaries, were zone processed and four point bend specimens were electrically discharge machined from their processed regions. These specimens were subjected to four point bending. The outer fiber strain was measured with strain gages and this value along with the fracture stress used to compare properties between alloys. Based upon these test results, a Cr/Mn quaternary had the highest strength and ductility. However, this enhanced fracture stress and ductility was not substantial, 470 MPa and 0.6 percent, respectively. Although all of the quaternary alloys considered were slightly two phase, the variation in the extent of the γ single phase field was still determined.

TABLE OF CONTENTS

CHAPTER	PAGE
I. INTRODUCTION	1
BINARY TiAl	2
BINARY Ti-Al PHASE DIAGRAM	6
BINARY TWO PHASE MECHANICAL PROPERTIES	10
ALLOY ADDITIONS	12
SILVER	13
CHROMIUM	14
GALLIUM	15
MANGANESE	15
ZIRCONIUM	17
II. EXPERIMENTAL APPROACH	18
III. RESULTS	33
IMPURITY ANALYSIS	33
ATOM LOCATION	34
BINARY TiAl PHASE BOUNDARY	38

TERNARY PHASE BOUNDARIES 40

HOT WORKING 44

HOMOGENIZED HARDNESS 46

QUATERNARY COMPOSITIONS 47

BEND TEST AND MICROSTRUCTURAL RESULTS 50

THE Ti-50/Al-50 ALLOY 52

THE Ti-52/Al-48 ALLOY 55

THE Ti-49.5/Al-49.5/Cr-1 ALLOY 57

THE Ti-48.5/Al-48.5/Cr-1/Mn-2 ALLOY 58

THE Ti-48.5/Al-49.5/Cr-1/Zr-1 ALLOY 59

THE Ti-48/Al-48/Ga-2/Mn-2 ALLOY 61

THE Ti-48/Al-48/Mn-2/Zr-2 ALLOY 62

EVIDENCE OF DUCTILITY 64

COMPARISON OF CURRENT RESULTS TO THOSE GIVEN IN LITERATURE 64

IV. SUMMARY OF RESULTS AND CONCLUSIONS 66

REFERENCES 68

APPENDIX 73

VITA 156

LIST OF TABLES

TABLE	PAGE
Table 1. Properties of Titanium Aluminides, Titanium-Base Conventional Alloys, Super alloys, and 4340 Steel	74
Table 2. Ternary Alloy Compositions Studied Assuming Different Substitution Behaviors	75
Table 3. Estimate of Accuracy of EDX Analysis on Single Phase TiAl Alloys	76
Table 4. Estimate of Resolution of EDX Analysis on TiAl Alloys	77
Table 5. Dissolved Impurity Analysis of Homogenized Alloys	78
Table 6. K Factor Relative to Silicon for Elements Analyzed using ALCHEMI	79
Table 7. Site Occupancy Behavior in TiAl for Cr, Mn, and Zr. Determined from ALCHEMI Results Using Multivariant Analysis.	80
Table 8. Phase Boundary Compositions for a Ti-45Al Alloy Homogenized at 1100 C for 100 hr. Followed by Cooling to 600 C and Holding for Various Times Before Quenching to Room Temperature.	81
Table 9. Four Point Bend Test Results for Zone Processed and Homogenized Alloys	82
Table 10. Average Percent Plastic Strain Determined by a Linear Offset Method for Zone Processed and Homogenized Alloys Subjected to Four Point Bending.	83
Table 11. Literature Four Point Bend Data for Arc Melted and Homogenized Alloys.	84

LIST OF FIGURES

FIGURE	PAGE
Figure 1. Unit Cell of Stoichiometric TiAl Showing a Typical Slip Plane and Some Physical Properties	85
Figure 2. Binary Ti-Al Phase Diagram	86
Figure 3. Schematic CCT Diagrams for Both 45 Al and 48 Al Representing the Decomposition of the High Temperature α Phase.	87
Figure 4. A Comparison of Observed and Calculated Tensile Ductility as a Function of Grain Size or Colony Size for Ti-48.4/Al-47/Nb-2.6/(Cr+V)-2.	88
Figure 5. The Dependence of Fracture Toughness on Grain Size or Colony Size for Various TiAl Alloys [25].	89
Figure 6. AB Structure Map [26].	90
Figure 7. Typical Bend Contour Showing Locations of EDX Analysis.	91
Figure 8. Plots of Impurity Counts (Cr, Mn, and Zr) Versus $\Sigma\alpha_i N_i$ Showing Linear Fit to Model Assumed by the Mutivariant Analysis Technique Used to Calculate ALCHEMI Data.	92
Figure 9. Experimental 1100 C TiAl+Ag Ternary Phase Diagram.	93
Figure 10. 800 C TiAl+Ag Ternary Phase Diagram Proposed by Hashimoto et al. [46].	94

Figure 11. CBED Image Showing Small Second Phase in Ti-50/Al-48/Ag-2 Homogenized Alloy. 95

Figure 12. Experimental 1100 C TiAl+Cr Ternary Phase Diagram. 96

Figure 13. Experimental 1100 C TiAl+Mn Ternary Phase Diagram. 97

Figure 14. 1000 C TiAl+Mn Ternary Phase Diagram Proposed by Hashimoto et al [55]. 98

Figure 15. Experimental 1100 C TiAl+Zr Ternary Phase Diagram. 99

Figure 16. 1000 C TiAl+Zr Ternary Phase Diagram Proposed by Hashimoto et al. [55]. 100

Figure 17. Homogenized Hardness versus Alloying Addition for Single Phase TiAl Ternary Alloys. 101

Figure 18. Hardness and Tensile Elongation versus Aluminum Content for Binary TiAl Alloys [7]. 102

Figure 19. Typical Optical Microstructure and Fractograph for Arc Melted and Homogenized Ti-50/Al-50. 103

Figure 20. Typical Optical Electro Polished Microstructures and Fractographs for Drop Cast and Homogenized Ti-50/Al-48/Ag-2. 104

Figure 21. Typical Optical Microstructures and Fractographs for Arc Melted and Homogenized Ti-48.5/Al-48.5/Cr-3. 105

Figure 22. Typical Optical Microstructures and Fractographs for Arc Melted and 106

Homogenized Ti-50/Al-48/Ga-2.

Figure 23. Typical Optical Electro Polished Microstructures and Fractographs for Arc Melted and Homogenized Ti-48/Al-50/Mn-2. 107

Figure 24. Typical Optical Electro Polished Microstructures and Fractographs for Drop Cast And Homogenized Ti-49.5/Al-49.5/Zr-1. 108

Figure 25. Fractograph of Drop Cast and Homogenized Ti-50/Al-46/Ag-4 Showing a Ag-Al Solid Solution Along a Grain Boundary. 109

Figure 26. Typical Optical Electro-polished Microstructures for Arc Melted and Homogenized Ti-50/Al-50, Etched. 110

Figure 27. Macro of Zone Melted Ti-50/Al-50. 111

Figure 28. Microstructure of Zone Processed Ti-50/Al-50. 112

Figure 29. Optical Microstructure of Zone Processed and Homogenized Ti-50/Al-50. 114

Figure 30. SEM Fractographs of Zone Processed and Homogenized Ti-50/Al-50. 115

Figure 31. Macro of Zone Melted Ti-52/Al-48. 118

Figure 32. Microstructure of Zone Processed Ti-52/Al-48. 119

Figure 33. Homogenized Microstructure of Zone Processed Ti-52/Al-48. 120

Figure 34. SEM Fractographs of Zoned Processed and Homogenized Ti-52/Al-48. 122

Figure 35. Zone Melted Ti-49.5/Al-49.5/Cr-1. 123

Figure 36. Homogenized Microstructure of Zone Processed Ti-49.5/Al-49.5/Cr-1. 125

Figure 37. SEM Fractographs of Zoned Processed and Homogenized Ti-49.5/Al-49.5/Cr-1. 127

Figure 38. Macro of Zone Melted Ti-48.5/Al-48.5/Cr-1/Mn-2. 128

Figure 39. Microstructure of Zone Processed Ti-48.5/Al-48.5/Cr-1/Mn-2. 129

Figure 40. Homogenized Microstructure of Zone Processed Ti-48.5/Al-48.5/Cr-1/Mn-2. 130

Figure 41. SEM Fractographs of Zoned Processed and Homogenized Ti-48.5/Al-48.5/Cr-1/Mn-2. 132

Figure 42. Macro of Zone Melted Ti-48.5/Al-49.5/Cr-1/Zr-1. 133

Figure 43. Microstructure of Zone Processed Ti-48.5/Al-49.5/Cr-1/Zr-1. 134

Figure 44. Homogenized Microstructure of Zone Processed Ti-48.5/Al-49.5/Cr-1/ Zr-1. 135

Figure 45. SEM Fractographs of Zoned Processed and Homogenized Ti-48.5/Al-49.5/Cr-1/Zr-1. 137

Figure 46. Macro of Zone Melted Ti-48/Al-48/Ga-2/Mn-2 Transverse and Longitudinal Section. 139

Figure 47. Microstructure of Zone Processed Ti-48/Al-48/Ga-2/Mn-2. 140

Figure 48. Homogenized Microstructure of Zone Processed Ti-48/Al-48/Ga-2/Mn-2. 141

Figure 49. SEM Fractographs of Zoned Processed and Homogenized Ti-48/Al-48/Ga-2/ Mn-2. 143

Figure 50. Zone Melted Ti-48/Al-48/Mn-2/Zr-2. 144

Figure 51. Homogenized Microstructure of Zone Processed Ti-48/Al-48/Mn-2/Zr-2. 146

Figure 52. SEM Fractographs of Zoned Processed and Homogenized Ti-48/Al-48/Mn-2/ Zr-2. 148

Figure 53. Engineering Stress (MPa) versus Percent Engineering Strain for Four Point Bending of Ti-50/Al-50. 149

Figure 54. Engineering Stress (MPa) versus Percent Engineering Strain for Four Point Bending of Ti-52/Al-48. 150

Figure 55. Engineering Stress (MPa) versus Percent Engineering Strain for Four Point Bending of Ti-49.5/Al-49.5/Cr-1. 151

Figure 56. Engineering Stress (MPa) versus Percent Engineering Strain for Four Point Bending of Ti-48.5/Al-48.5/Cr-1/Mn-2. 152

Figure 57. Engineering Stress (MPa) versus Percent Engineering Strain for Four Point Bending of Ti-48.5/Al-49.5/Cr-1/Zr-1. 153

Figure 58. Engineering Stress (MPa) versus Percent Engineering Strain for Four Point Bending of Ti-48/Al-48/Mn-2/Zr-2. 154

Figure 59. Engineering Stress (MPa) versus Percent Engineering Strain for Four Point Bending of Ti-48.5/Al-48.5/Ga-2/Mn-2. 155

I. INTRODUCTION

Binary Ti and Al base intermetallics, in the range of 45 a/o to 56 a/o Al, are being investigated for possible high temperature applications. These materials are attractive because of their low density, attractive high temperature properties, favorable room temperature fracture toughness relative to ceramics, and good oxidation resistance. However, they have seen little use, because of their lack of room temperature ductility. The best tensile room temperature ductility of 2.7% was obtained on a 48 a/o Al binary alloy possessing a small grain size of 10 μm. This alloy consists of an ordered DO_{19} phase, α_2-based on Ti_3Al, and an ordered $L1_0$ phase, γ-based on stoichiometric TiAl.

Published results indicate that the two phase 48 a/o Al alloy is more ductile than single phase alloys [1]. However, the two phase alloys are limited in operating temperature, because of a eutectoid transformation that occurs at 1125 C. In addition, two phase alloys lack the high temperature strength of single phase γ alloys. These two phase alloys also lack the high ordering temperature, 1450 C, which the single phase alloys possess.

There are many explanations in the literature for the lack of room temperature single phase ductility. These range from the absence of five independent slip systems required by the Von Mises criterion for polycrystalline deformation to a cleavage strength that is low in comparison to the critical resolved shear stress. These problems have been attributed to:

1) pinning of a/6[112] type partial dislocations, by an unknown mechanism;

2) anisotropy of Peierls stress, as a consequence of the ordered structure;

3) the non-cubic structure of γ;

4) dissolved impurities like N, C, and O ,which can

embrittle γ; and

5) a strong covalent nature to the Al/Ti bonding, which is high for higher Al contents.

Huang and Kawabata show that the fracture strain decreases with increasing Al content for TiAl based alloys [3,4]. This supports the above claim that higher Al alloys are more brittle. From the work on a 48 a/o Al, two phase, fine grained binary alloy, the tensile ductility changes from 2% to 2.7% when the dissolved O level is reduced from 800 ppm to 370 ppm [5]. Dissolved O, an $\alpha 2$ stabilizer, is known to embrittle γ when the dissolved O levels are in excess of 400 to 500 ppm. Consequently, one objective of this research is to attempt to expand the γ single phase field to lower Al contents by microalloying while maintaining low dissolved O levels. This is in an attempt to try to improve room temperature ductility of single phase TiAl. To achieve this objective, TiAl was alloyed with 0.5 to 5 a/o ternary and quaternary alloying additions. These additions were chosen not only to attempt to shift the boundary to lower Al, but to improve the strength and ductility as well. As a consequence of the known embrittlement effect interstitials have on TiAl, the processing methods were chosen such that the impurity levels were held to a minimum.

1. BINARY TiAl

Binary TiAl (γ) has an $L1_0$ structure consisting of alternating layers of Al and Ti atoms, Figure. 1* . Stoichiometric γ has a density of 3.76×10^3 kg/m^3 and a Young's Modulus and Shear Modulus of 178 GPa and 71.4 GPa, respectively [5,6]. For single phase γ alloys at off-stiochiometric compositions, excess Ti and Al occupy antisites without creating vacancies [7]. A comparison of properties of single phase TiAl to other Ti alloys is given in table 1* [1]. Gamma based alloys have the lowest density, high modulus, moderate yield and tensile strength, and excellent creep and oxidation resistance in comparison to super alloys, Ti based

* All figures and tables are found in the APPENDIX.

alloys, and Ti_3Al based alloys.

The interest in TiAl based materials is the result of the excellent high temperature properties of these alloys. At elevated temperatures, significant ductility is seen. At 900 C the single phase stoichiometric binary alloy has as much as 55% elongation. The 900 C fracture stress, 192 MPa, is approximately half that of the room temperature value, 486 MPa [8]. The ductile brittle transition temperature is composition dependent and is approximately 700 C. Above 900 C, the oxidation and strength properties of TiAl alloys degrade. In this temperature range, TiAl shows signs of dynamic recrystallization which possibly relates to the rapid strength loss [9].

TiAl is face-centered tetragonal with a slight tetragonality in the C-direction. Stoichiometric TiAl has A and C lattice parameters of 0.4005 nm and 0.4070 nm, respectively [10]. The lattice parameters and the C/A ratio vary with composition. The minimum C/A occurs at the stoichiometric alloy and has a value of 1.02 [5].

Single crystal TiAl has a preferred growth direction of a few degrees off the [001] [11]. These crystals show significant compressive ductility at room temperature, as much as 12% when oriented appropriately (e. g., [123]) with the loading axis [12]. The yield stress is temperature dependent and shows an abnormality by having a maximum yield stress of 250 MPa at 600 C for the [123] orientation. Single crystals show a low strain rate sensitivity when tested below the ductile brittle transition temperature (DBTT) of 700 C [13,1]. However, above this temperature, the strain rate sensitivity parameter increases rapidly with temperature [12].

For polycrystalline, single phase materials, at room temperature, the ductility drops off and the yield strength remains constant with increases in Al content [4,3]. The fracture toughness is the same as that of slightly two phase (3 to 15 volume percent), fine grained alloys (i. e., 48 a/o Al) with a value of 10 to 16 MPa$\sqrt{m}$ [5]. This value is much lower than alloys with

fully lamellar microstructures, 43 a/o to 45 a/o Al, which have a K1c of 20 to 30 MPa$\sqrt{m}$. However, these latter materials have null ductility [5]. Single phase materials have tensile ductilities of 0.5 to 1% [3]. Room temperature compressive testing has yielded up to 8% strain in these materials [12]. Microhardness testing indicates that single phase TiAl hardens with increasing Al content, from a value of 170 DPH for the stoichiometric binary alloy to 210 DPH for the 54 a/o Al alloy. The room temperature tensile yield and fracture strengths are relatively constant with increasing Al content, 370 MPa and 425 MPa, respectively [3]. These values decrease rapidly above the DBTT to values of 225 MPa and 250 MPa at 900 C, respectively, while the plastic fracture strain increases up to 30% [3].

The character of the fracture surface is as dependent upon the temperature as with all other properties. The fracture mode is predominantly cleavage at room temperature. As the DBTT is reached, a mixed fracture mode of cleavage and intergranular fracture prevails, with the amount of intergranular fracture being pronounced [13]. Signs of ductility appear at temperatures above the DBTT.

Plastic deformation for single crystalline and polycrystalline TiAl occurs via the following systems:

i) slip due to a/2 <110> type ordinary dislocations on {111},

ii) superdislocation slip of the appropriate type of a/2<112>, a <011> or its equivalent a<101>, all on {111},

iii) slip due to partials of the type a/6<112>, and

iv) twinning using <112>{111} type system [14,15].

The predominate operative system below 600 C is mode i). All of the above modes are operative above 700 C. The dislocations of the type a/2<110> theoretically may break into the partials a/6<211> and a/6<121> via the reaction

$$a/2\langle 110\rangle \Rightarrow a/6\langle 211\rangle + CSF + a/6\langle 121\rangle, [15]$$

where CSF is a complex stacking fault. The CSF has an energy approximately that of the stacking fault (SF) energy plus the antiphase boundary (APB) energy. The APB energy for the {111} slip planes was estimated using a quasichemical approach to be 47×10^{-2} J/m^2 [12]. This high value makes disassociation of $a/2\langle 110\rangle$ type partials unlikely [16]. The superdislocation $a/2\langle 112\rangle$ type may break into partials by way of the following reaction:

$$a/2\langle 112\rangle \Rightarrow a/6\langle 112\rangle + SF + a/3\langle 112\rangle [15].$$

There are several possible reactions which $a\langle 101\rangle$ type superdislocations may undergo:

$$\langle 101\rangle \Rightarrow a/2\langle 101\rangle + APB + a/2\langle 101\rangle,$$

$$\langle 101\rangle \Rightarrow a/6\langle 112\rangle + SF + a/6\langle 514\rangle, \text{ and}$$

$$\langle 101\rangle \Rightarrow a/2\langle 110\rangle + a/2\langle 112\rangle [15].$$

The splitting of the $a\langle 101\rangle$ type dislocation appears to be 1×10^{-9} m, hence, it may be difficult to observe [17].

The a/2[011] and a[101] type dislocations have been determined to cross slip onto the cube planes. This may indicate that the mechanism operating is similar to the Kear–Wilsdorf mechanism, which is associated with cross slip of screw dislocations from {111} to {100}. Dislocations on the {100} are difficult to move because of the high Peierls stress. This mechanism has been observed to operate and may relate to the yield stress abnormality in single crystalline materials [16]. If this is true, this mechanism may be one explanation for pinning of the a/6[112] type partials which is proposed to control the plasticity [13].

The a/6[112] type partial is also the twinning dislocation. Hence, if this dislocation was to

become pinned, then it would be expected to see reduced activity of both twinning and slip of the superdislocation. This is exactly what occurs for room temperature deformation processes. The predominate dislocations seen, are of the type a/2[110] with very few twins and superdislocations being observed [12]. The mobility of a/6[112] type partial controls 2/3 of the dislocations in TiAl as well as thickening of [112](111) type twins [13]. The a/6[112] type partials are no longer pinned once the DBTT is achieved. An increase in the activity of both twinning and slip of the superdislocations is observed [13]. In a very narrow temperature range near the DBTT, cross twinning is observed. This involves the [112](111) type twin, twinning onto another (111) plane of the same family when it intersects another twin of the same kind [13]. Twinning becomes the main deformation mode at 800 C.

The typical cleavage planes are {010}, {001}, {110}, {101}, and {111} [10]. Kawabata et al. explain cleavage fracture based on a fracture mechanism which deals with two gliding dislocations meeting at the junction of their respective slip planes. These dislocation interact producing a sessile dislocation of lower energy, which absorbs the following piled up dislocations creating microcracks. The fracture planes observed are consistent with this mechanism.

2. BINARY Ti-Al PHASE DIAGRAM

The Ti-Al phase diagram has undergone many changes since its first publication. These changes are attributed to differences in methods of phase determinations, impurity contents, heat treatments, and misinterpretation of microstructure. There are many conflicting results in literature concerning the $\gamma + \alpha 2$ boundaries as well as the details of the high temperature reactions. Figure 2 shows a composite diagram composed from excerpts of phase diagrams in the literature . This figure shows two reactions which determine if a zone processed 48 a/o Al to 52 a/o Al alloy will be single phase at room temperature, the peritectic reaction at 1440 C

and the $\gamma + \alpha 2$ boundary position [18].

The peritectic reaction has been the source of a great deal of controversy. Literature indicates that the peritectic solidus and liquidus are approximately 50 a/o and 54 a/o Al, respectively. The peritectic composition appears to be at least 52 a/o Al [18,19].

The shape of the $\gamma + \alpha 2$ boundaries is also a subject of some arguments. The low temperature (e. g., 600 C) $\alpha 2 + \gamma / \gamma$ boundary has been reported to be from 49 a/o to 51 a/o Al [20,3]. This boundary has a minimum composition of 48 a/o Al at 1115 C, the eutectoid temperature, and shifts toward higher Al contents as the temperature is lowered.

The boundaries of the two phase field, $\alpha 2 / \alpha 2 + \gamma$ and $\alpha 2 + \gamma / \gamma$, have been extensively studied by Jones and Kaufman [21]. They investigated the effects of cooling rate, composition, and heating rate on binary two phase alloys containing low dissolved oxygen and nitrogen levels (400–700 ppm and 40–150 ppm, respectively). These alloys were cooled from and heated to the single phase α field and the resulting microstructure interpreted. They developed schematic continuous-cooling-transformation (CCT) diagrams for alloys with compositions ranging from 40 a/o to 50 a/o Al. They found that γ precipitation could be completely suppressed in alloys of less than 45 a/o Al by quenching from the α field. However, this was not the case in higher Al content alloys, 48 a/o and above. In these alloys γ tended to be either lamellar or massive in nature. A sluggish dissolution and precipitation of γ was observed. The γ which formed tended to have a semi-coherent or coherent interface with the parent α or α_2, which leads to high strains being produced. Early studies indicated that γ nucleated at both grain boundaries and stacking faults in α_2. The nucleation of γ on stacking faults yielded the above mentioned orientation relationship between α_2 and γ and the coherency between the phases. This orientation relationship leads to a lamellar structure, the fineness of which depends on the thermal history. Later microstuctural studies have shown that heterogeneous

grain boundary nucleation does not appear to be a major mode for nucleation of γ. Hence, stacking fault nucleation is the predominate nucleation mode. Preferential nucleation does appear near grain boundaries. However, this may be attributed to the discontinuous coarsening of $\alpha 2$, α, and γ that occurs in the vicinity of grain boundaries, leading to the formation of jagged interlocking grain boundaries.

One of the more interesting facts that resulted from the work of Jones and Kaufman was the idea that the eutectoid reaction occurring at 1115 C and approximately 39.5 a/o Al is suppressed under normal cooling rates. They suggest that α can transform into $\alpha 2$ rather rapidly, since α_2 is an ordered version of α. However, the formation of γ from α is more difficult owing to the structure difference and the sluggish nature of the α_2 to $\alpha_2 + \gamma$ reaction. They express that due to the difference in precipitation kinetics, it seems unlikely that the eutectoid reaction is kinetically possible under normal cooling rates. They contend that the lamellar structure that forms is the result of combinations of temperature and composition producing comparable growth rates of α_2 and γ resulting in a eutectoid like structure. Jones et al. support these claims with microstructural observations for low Al (40a/o Al) samples furnace cooled from the α region. The microstructure that results consists of large equiaxed α_2 grains containing fine, irregularly spaced γ plates, which is not indicative of a eutectoid reaction.

They also contend that the precipitation of γ from α is similar to that from α_2, nucleation of γ on stacking faults. The microstructural evidence on a 42 a/o Al alloy heated in single phase α region and furnace cooled to the $\alpha + \gamma$ phase field (1130 C) supports their argument. The structure, after water quenching from 1130 C, consists of serrated grain boundaries where adjacent γ plates appear coarser than those inside the prior α grain. They found that γ appears to undergo an unusual coarsening process. In this process, γ plates coarsen by thickening and/or spreading process as they grow into the neighboring grains.

For the higher Al alloys, 45 a/o Al and 48 a/o Al, the cooling rate has a different effect on the microstructure. Water quenching from the α region for these alloys suppresses γ in the 45 a/o Al alloy, but not in the 48 a/o Al alloy. The γ which forms in these two alloys shows anti-phase boundaries (APB) produced in γ by the ordering reaction which occurs for the α to γ transformation. Thin deformation twins are also seen in these alloys. Since APBs are produced from the transformation of α to γ and not by an intermediate disordered phase reaction and deformation twins are formed, Jones et al. suggest that this is a massive reaction. They indicate that the nucleation of massive γ occurs on stacking faults in α, which is similar to the mechanism which occurs for nucleation of lamellar γ.

Figure 3 shows some of the CCT curves resulting from their work. For high Al content alloys (48 a/o Al), the decomposition of α depends greatly on the cooling rate. At fast cooling rates, water quenching, the reaction of α to γ is massive in nature. At slower cooling rates, air cooling, the structure is mostly lamellar with some signs of massive reaction of α to γ. For the lower 45 a/o Al alloys, α transforms to $\alpha 2$ when water quenched. For slower cooling rates with these low Al alloys, α precipitates γ followed by the remaining α ordering to become $\alpha 2$.

Upon heating single phase γ into the $\alpha + \gamma$ region, α is seen to precipitate at the grain boundaries and in the γ matrix. Intergranular α has the same orientation as was observed for γ precipitation from either $\alpha 2$ or α. Additionally, there are four {111} type habit planes in any grain.

From the complicated nature of precipitation and decomposition of α, $\alpha 2$, and γ, care must be taken to properly identify the correlation of microstructure to the phase diagram. This causes an added complication when trying to extend the $\alpha 2 + \gamma / \gamma$ boundary to lower Al contents, which is an objective of this research.

3. BINARY TWO PHASE MECHANICAL PROPERTIES

Since the two phase 48 a/o Al alloy has the best ductility for the binary alloys, it was used as a base line to which the ternary and quaternary alloys were compared. A brief survey of two phase alloy properties is presented.

There are two classes of two phase alloys based on TiAl, lamellar and duplex. The lamellar alloys are of low Al content and consist mainly of lamellar colonies, grains, composed of $\alpha 2$ and γ platelets. A small amount, 5 volume percent, of fine γ grains exist at the colony boundaries. Fully lamellar microstructures exhibit poor tensile properties and ductilities, but excellent creep properties and favorable fracture toughness with K1c values from 20 to 30 MPa$\sqrt{m}$ [22]. The fracture mechanism in lamellar structures consists of crack deviation, crack bridging, and ligament toughing. In this case, ligament toughening refers to the process whereby mismatched microcracks ahead of the main crack joined via shear ligaments. Duplex alloys (e. g. 48 a/o Al binary alloy) consist mostly of γ with a small amount of the lamellar structure at the grain boundaries. As previously mentioned, these alloys show the best combination of strength and ductility. However, the fracture toughness is not as high as that of the lamellar class. The fracture toughness of the duplex class of alloys is similar to that of single phase γ alloys with K1c values from 10 to 16 MPa$\sqrt{m}$. The fracture mechanism of duplex and γ alloys is generally intergranular fracture and cleavage.

The mechanical properties of both the lamellar and duplex structures are dependent upon the orientation of the microstructure and the amounts and distribution of the phases. From tests on single grain lamellar structures, the most favorable orientation for ductility is when the lamellae are near 45^{0} to the loading axis. With this orientation, slip occurs in the γ phase on the $\{111\}$ planes, which are parallel to the lamellar boundaries. In this situation, slip never crosses the lamellar boundaries. As this orientation is changed, slip and/or twinning occurs on

other {111} planes and is now no longer confined to the gamma phase. Consequently, slip is impeded by the lamellar boundaries increasing the strength and decreasing the ductility [23]. 13% tensile elongation and a yield stress of 100 MPa were achieved at room temperature in a 51° orientation. The maximum strength occurs when the lamellae and loading axis are at 90°. There appears to be a Hall-Petch relationship between the lamellar spacing and the yield strength [23]. These materials were produced by zone processing, which resulted in the major constituent phase γ, of the lamellar structure, containing a large number of thin twins parallel to the lamellar boundaries. " Since this phenomenon and polysynthetic twinning, which is often observed in mineral crystals, are analogous, these crystals are called polysynthetically twinned crystals" [24].

The grain size or colony size has a large effect on the ductility and fracture toughness of these alloys [25]. Figures 4 and 5 illustrate this. The best value of ductility is obtained at grain sizes less than 100 μm. The fracture toughness improves with increase in grain size up to 500 μm, after which it appears to level off. For two phase binary alloys the best ductility occurs when the volume fraction of $\alpha 2$ is between 3 and 15 percent [5]. Below this amount, grain growth becomes a problem when these alloys are heated into the two phase region. Above 15 volume percent, the brittle $\alpha 2$ phase starts to control the properties creating a brittle alloy. The ratios of lamellar $\alpha 2 + \gamma$ colony size to γ grain volume, $\alpha 2$ to γ plate thickness, and $\alpha 2$ to γ grain volume are also very important with respect to improving the ductility. For best ductility, these should be 30 to 50 %, 25 to 40 %, and 5 to 15 %, respectively [1]. The grain/colony size is also very important. For best ductility, this should be held to a minimum. In fact, the Japanese have produced, in TiAl two phase ternary alloys with Cr and Mn, superplasticity of better than 300% when tested at 1200 C for ultra fine grained alloys [24].

4. ALLOY ADDITIONS

As an attempt to improve the room temperature ductility of TiAl, alloying elements were added such that the $\alpha 2 + \gamma / \gamma$ boundary was shifted to lower Al contents. In addition, elements were chosen which showed promise for improving the ductility and strength of the γ phase. The alloying additions chosen were based up on literature information and structure map considerations. The elements chosen were Ag, Cr, Ga, Mn, and Zr.

The theoretical basis used for the choice of alloying elements were structure maps for AB compounds. These were derived by Pettifor, who assigned a Mendeleev number for each element in the periodic table such that common experimentally determined structure types were grouped together [26]. These numbers were assigned based not only on the periodicity of elements in the periodic table, but also from considerations based upon atom valence and atom size. By using known structures for AB compounds, and the Mendeleev number of the A and B elements in these compounds, he found that similar structures fell within the same region on these maps. Figure 6 shows the structure map for AB compounds. The Mendeleev numbers for the elements considered in this research are: Ti (51), Al (80), Mn (60), Cr (57), Zr (49), Ag (71), and Ga (81). TiAl forms an $L1_0$ compound. From plotting the Mendeleev number of Ti versus that of Al, an $L1_0$ compound is predicted on the structure map. By plotting the number for Ga versus that for Ti, the map shows that an $L1_0$, slightly tetragonal ordered FCC, structure is found. This indicates that Ga additions to TiAl will replace Al and eventually form an $L1_0$ compound. Manganese and Cr are thought to substitute randomly in TiAl. Hence, if these are plotted individually versus the Mendeleev numbers for Ti and Al, the structures one finds for TiMn, AlMn, TiCr, and AlCr are CsCl structure types. This is a B2, ordered BCC, structure which has many more slip systems than the $L1_0$ structure. Consequently, as more Mn or Cr is added to TiAl the structure could possibly approach B2 and

have an improvement in ductility. It is possible that small additions to the $L1_0$ structure will allow it to still remain stable, but will shift $L1_0$ toward a more cubic, B2-like, structure, which could be more ductile.

There is evidence in literature that a structure change to a more ductile cubic phase can be achieved by alloying. By use of alloying and the A_3B structure maps, the tetragonal Al_3Zr was transformed into a cubic $L1_2$ structure which was more ductile [26]. The additions to Al_3Zr were determined by using the Mendeleev number for prediction of the structure. It is possible that this technique could be as successful on TiAl as it was for Al_3Zr.

Gallium is considered to substitutes for Al, and consequently could shift the γ phase boundary to lower Al contents. Manganese and Cr are known to improve ductility of two phase alloys. This trend may continue to the single phase γ alloys, especially since from structure map considerations, both Mn and Cr form B2 compounds with Ti and Al. These B2 compounds may have more active slip systems due to the higher symmetry. Small additions of Zr are known to increase the strength as well as the ductility of the binary alloy, hence, this alloy addition was examined to take advantage of this. Published word indicates that Ag is thought to improve the formability of TiAl and consequently, may improve the ductility. This motivated the consideration of Ag additions. The following sections further explain the experimental considerations of the alloying elements chosen.

5. SILVER

Published work indicates that Ag additions to TiAl improve its formability. Large additions, 4 a/o to 15 a/o, have been shown to improve the room temperature ductility at the expense of the high temperature strength [27]. Silver additions show ductility in compression for ternary alloys with Al contents of 50 a/o to 51 a/o. Silver is considered to substitute for Al in TiAl.

Hence, the $\alpha 2+\gamma/\gamma$ boundary could be shifted toward higher Ti contents, which is what has been observed to occur [28]. As additions of Ag increase both the C and A axes of γ increase and the C/A ratio increases [29]. Silver additions are known to soften the binary alloy. There is a reported maximum solubility of 2.7 a/o Ag in TiAl [29]. When the solubility is exceeded, a low melting point Ag solid solution is formed at the grain boundaries [27].

6. CHROMIUM

The solubility of Cr is much higher in Ti_3Al than it is in TiAl [30]. Also, Cr appears to be an $\alpha 2$ stabilizer. Hence, most of the work that has been reported is for two phase alloys [30]. Results in the literature indicate that Cr additions increase the yield and fracture stress of TiAl. With 3 a/o Cr, the ternary alloy strength doubles [4]. For additions greater than this, the strength drops off. Chromium additions decrease the C/A ratio and have been determined to substitute randomly in TiAl [28]. For two phase alloys, Cr additions cause a decrease in grain size and an increase in intergranular fracture area at room temperature [4]. The fracture toughness (greater than 30 MPa$\sqrt{m}$) for Cr ternary two phase alloys is comparable to that of the fully lamellar binary alloys. However, this is much higher than the 10 to 16 MPa$\sqrt{m}$ fracture toughness for single phase binary alloys [30]. The oxidation resistance with Cr additions is greatly reduced in comparison to binary TiAl [31]. The most attractive quality of Cr additions is that the propensity for annealing and deformation twins to form is greatly increased. In addition, the DBTT appears to be reduced. This may be the reason that a 4% room temperature tensile strain was obtained for a fine lamellar Ti-53/Al-46/Cr-1/Si-0.2 alloy*. For this alloy, the plastic strain does not change much until the temperature is 800 C. At this temperature, 35% plastic strain is obtained. By 1000 C, 100% plastic strain can be achieved.

---

* All compositions are in atomic percent unless otherwise indicated.

The type of dislocations operating in compression at room temperature are: a/2[110], a[011], and a/2[112] all on the corresponding {111}. It is interesting to note that the 1/2[112] is only active at temperatures above 700 C in binary TiAl, but is seen in Cr alloys at room temperature. At temperatures above 600 C, another slip system,[001]{110}, starts to operate [30]. This slip system is not observed in the binary alloys.

7. GALLIUM

Gallium forms an $L1_0$ compound with Ti, and this argues for Ga substitution for Al. Literature indicates that Ga does substitute for Al and has a maximum solubility of 7 a/o in TiAl [32,33]. Gallium additions, up to 5 a/o, soften TiAl. The C/A ratio decreases toward unity as the Ga content is increased [33]. Gallium additions increase the amount of intergranular failure at room temperature. Gallium appears to ductilize polycrystalline single phase TiAl. This is evidenced by signs of wavy slip produced in compression and by the 1.2% outer fiber strain at fracture produced in a thin, 1.5 mm, Ti-52/Al-43/Ga-5 alloy [33,34]. At high compressive loads, twinning becomes the predominate deformation mode. The deformation is mainly associated with slip of a/2[110] dislocations and twinning. However, the superdislocations a[011] and a/2[112] are also observed [33].

8. MANGANESE

Manganese additions of less than 1 a/o soften TiAl. Above this amount, Mn hardens TiAl. Additions of Mn are thought to decrease the C-axis while leaving the A-axis unchanged. Hence, the C/A decreases with additions of Mn [35]. Babu et al. state that Mn substitutes for Ti in TiAl up to 2 a/o Mn [36]. Beyond this amount, substitution is random. However, Tsujimoto et al. state that Mn substitutes solely for Al in TiAl [37]. Kasahara et al. also finds that Mn additions extend the $\alpha 2 + \gamma / \gamma$ boundary toward lower Al contents. Manganese

additions decrease the oxidation resistance in comparison to the binary alloys [31].

The best bend ductility of 5% occurred for Ti-50.6/Al-48.4/Mn-1 alloy. This was a two phase polycrystalline alloy with a sample thickness of 0.8 mm. The yield strength of this alloy increased with temperature, from 312 MPa at room temperature to 360 MPa at 800 C, compared to the polycrystalline stoichiometric binary alloy's yield strength remaining approximately constant with temperature [37]. Manganese additions increase the work hardening rate over that of the binary alloys [38]. The ductility is slightly improved. From Hashimoto's et al. compression data, it is interesting to note that the ductility is a maximum at 2.5 a/o Mn for alloys with an Al content of 48.5 a/o, which contained 10% by volume α_2. This is compared to having a maximum at 1 a/o for 50 a/o Al alloys containing 1 volume percent $\alpha 2$ [39]. The single phase alloys with 51 a/o Al showed increasing ductility with additions of Mn. However, the best ductility for this Al series was still far lower than any of the series that contained $\alpha 2$ [39]. For two phase binary alloys the best ductility occurs when the volume fraction of $\alpha 2$ is between 3 and 15 percent [5]. Below this amount grain growth becomes a problem when these alloys are heated into the two phase region. This appears to indicate that Mn additions may be a potent grain refiner, which is consistent with what Xiang'yan et al. report for two phase ternary Mn alloys [40]. Above 15 volume percent, the brittle $\alpha 2$ phase starts to control the properties creating a brittle alloy.

Manganese additions to TiAl increase the propensity to form both annealing and deformation twins suggesting a reduction in the SF and APB energies. The annealing twins that form are thermally stable [41,42]. Manganese alloys are thought to deform predominantly by twinning at room temperature [37]. The a/6<112> partial might have become more mobile as a result of Mn additions, since this partial is responsible for twinning [40]. With the increase of plastic strain, the number and size of twins increases rapidly [40].

There are three main types of dislocations active when TiAl+Mn is deformed at room temperature. These are the 1/2{112}, 1/2{110}, and {011} or its equivalent {101} [43]. It is interesting to note that the 1/2{112} is only active at temperatures above 700 C in the binary alloys; however, it is seen in Mn alloys at room temperature. Cross twinning is also observed with no indication of dislocation pileup. The cross twin plane is reported to be the {110}, which sees no activity in the binary alloys. This extra twin plane may be the source for the improved ductility, because of the increase in the number of deformation modes [43].

9. ZIRCONIUM

Zirconium is reported to occupy Ti sites in TiAl [37]. Additions of Zr shift the $\alpha 2 + \gamma / \gamma$ boundary toward higher Al [37]. Zirconium expands the A-axis while leaving the C-axis unchanged; consequently, the C/A ratio decreases [37]. Additions of Zr harden TiAl. For ternary TiAl alloys, an increase in the Al content with a fixed Zr content decreases the hardness. In contrast, as the Al content is increased for binary TiAl the hardness increases. Zirconium additions decrease the ductility in compression. However, increases in strength are obtained for both compression and bending [39]. In bending, the ductility goes through a maximum at Ti-50.5/Al-47/Zr-2.5. This is a two phase alloy.

II. EXPERIMENTAL APPROACH

The elements for microalloying additions to TiAl were chosen to address one or more of the previously mentioned possible causes of γ single phase brittleness. The elements considered are Ag, Cr, Ga, Mn, and Zr. For each of these elements, a series of 15 TiAl ternary alloys were arc melted and homogenized. The fifteen melts in each series were made with compositions assuming different substitution behaviors in TiAl. Five of these fifteen compositions assumed random substitution, five assumed Al substitution, and five assumed Ti substitution. Table 2 shows, in atomic percent, the composition ranges for each series.

The number and composition of phases in each of the above alloys were determined. This information was used to map the 600 C $\alpha 2 / \alpha 2 + \gamma$ and $\alpha 2 + \gamma / \gamma$ ternary phase boundaries for each series of the five alloying additions. A property evaluation was determined on each of the alloys from the five series. From each of these series, the composition of the alloy with the best perceived ductility was used to determine the quaternary alloy compositions. Ingots of these quaternary alloy compositions were zone processed, homogenized, and bend specimens sectioned from the processed ingots. The ternary alloy with the most promise for improved properties was also zone processed as well as two binary compositions, Ti-52/Al-48 and Ti-50/Al-50. These alloys also had bend specimens produced from the homogenized zone processed ingots. The bend specimens from the quaternary, ternary and binary alloys were subjected to four point bending. The strain and stress in the outer fiber were then determined. The bend test results were compared to determine if any property improvement had occurred as a result of alloying. Results were compared to the Ti-52/Al-48, a two phase binary alloy, and to the Ti-50/Al-50, a single phase binary alloy. The Al-48 alloy has the best ductility, for binary γ based alloys. The Al-50 alloy has the best single phase ductility and is the lowest

Al content for single phase γ. Both alloys were used as a base line for comparison. In addition, notched four point bend specimens from two quaternary alloys and the Ti-50/Al-50 binary alloy were used to determine K1, plane strain fracture toughness, values for each composition. Again, these values were compared to the Ti-50/Al-50 binary alloy to see if any improvement had resulted from alloying. After testing was completed, a microstructural characterization was performed using both optical and SEM techniques in order to correlate mechanical properties with microstructure. Two additional tests were performed to better understand the relationship between the mechanical properties and the alloyed structure. These were an impurity analysis and the determination of the substitution behavior of the alloying additions.

The above alloys were arc melted with a non-consumable tungsten electrode under flowing Ar. They were cast in a water cooled copper hearth enclosed in an atmosphere controlled chamber which was evacuated to 1 μm before being flushed with flowing Ar at a rate of 13 liter/min. This flow rate was maintained throughout the melting and casting process. After the consolidation of the base elements, the specimen was inverted and remelted at least five times in order to insure all base elements had been melted and that the alloy had no gross segregation. After casting, the button was examined for signs of excessive oxidation. If such signs were present then the alloy was discarded. After successful casting, the ingot was reweighed and that weight compared to the weight of the original charge. If the weight loss was greater than 0.1% , then the alloy was rejected and a new alloy was made. Once the alloy had passed this test, it was sectioned into halves with a diamond cut off saw. One half was examined for cast properties and the other was used to determine the properties of the homogenized samples.

The Zr and Ag ternary alloys were drop cast at NASA Lewis into 15x15x70 mm^3 rectangular ingots. These ingots appeared to have a minimum surface oxide and no unmelted particles

were observed. Minimum weight loss was assumed. A specimen from these ingots was used for property evaluations of the homogenized samples.

The half of the alloy to be homogenized was encapsulated in quartz tubing prior to homogenization. Encapsulation was performed in order to minimize oxidation of the sample. The encapsulation involved evacuating the quartz tubing to 0.13 Pa (1 μm). This tubing was flushed several times with Ar. After the final flush, the tubing was back filled to 790 Pa Ar pressure and sealed. At 1100 C, this pressure is approximately $1x10^5$ Pa (1 atm).

The heat treating scheme employed was to homogenize these alloys at 1100 C for 100 hrs. The cooling procedure involved cooling to 800 C , holding for 3 hrs, cooling to 600 C, holding for 3 hrs, and water quenching to room temperature. The heat treating times and temperatures were determined from the work of Hashimoto et al. [39]. They observed changes in hardness as a function of annealing time at 1000 C for stoichiometric TiAl and ternary alloys based on TiAl. For all cases, after approximately 72 hours, the hardness had leveled off indicating that a homogenized structure had been achieved. Based up on these results, if homogenization was performed at 1100 C for 100 hours, the cast structure would be completely removed. If phase transformations were going to occur between 600 C and 1100 C, then this step cooling procedure could allow enough time for transformations. After homogenization, the samples' surfaces had a very thin layer of surface oxide.

The microstructure characterization involved normal metallographic procedures. Once the sample had been polished through 1 μ Al_2O_3 slurry, the number of phases and their compositions were determined by using electron backscattering and energy dispersive analysis (EDX) in a Cambridge S-360 scanning electron microscope (SEM). The area percent of the phases present was determined from analysis of the backscattered (BS) image using a computer program of the SEM. This program produced a histogram analysis of the intensity

distribution of the BS image. From this analysis, the amounts of phases with a certain intensity levels were estimated. The composition of each phase was determined using EDX. EDX involved using an atomic number, absorption, and fluorescence (ZAF) correction program in conjunction with a Link AN 10000 analyzer. This program contained spectra written for real TiAl standards as opposed virtual Ti and Al standards. The real standards were employed because of excessive fluorescence and absorption problems in TiAl alloys. When these standards were not used, the EDX results on the binary alloys indicated low Al readings by at least 10 a/o. By using a 52 a/o Al splat quenched TiAl standard, supplied by Dr. David Snow of United Technologies, the Ti and Al profiles were rewritten. Adjustments were made to the ZAF program to account for the standard now being an alloy instead of an elemental standard. The updated ZAF program and the new Ti and Al profiles were used as the basis for the EDX analysis. This technique corrected the problem of low Al readings on the binary alloys. Using this new technique, the accuracy and resolution for binary alloys in the γ range were estimated to be better than +/- 1 a/o and approximately +/- 0.2 a/o, respectively. See tables 3 and 4 for these values. The accuracy was determined by performing EDX on several single phase homogenized binary alloys of known compositions. At least three spectra were run on each alloy and an average and standard deviation determined. The maximum composition difference, and a conservative estimate of accuracy, was determined by subtracting the extremes of the measured and actual compositions. The lowest accuracy was for the Ti-50/Al-50 alloy and was +/- 0.9 a/o Al. The resolution was determined by running EDX on the same sample three separate days. For each day, at least three spectra were run and the average and standard deviation determined. The resolution was determined by calculating the average and standard deviation of all the data run on the three different days. The average and standard deviation were 47.1 a/o Al and 0.2, respectively.

An estimate of the accuracy and resolution of the EDX measurement was needed for the

binary alloys, since the 600 C $\alpha 2 / \alpha 2 + \gamma$ and $\alpha 2 + \gamma / \gamma$ boundaries were determined. This is discussed in the results section.

After the SEM analysis, these samples were then subjected to electropolishing technique in order to remove any false structures, which often result when Ti alloys are mechanically polished. This technique involved using 44 ml N-butyl alcohol, 8 ml 60% perchloric acid, and 75 ml methanol as an electrolyte. The electrolyte was cooled to -70 C with a mixture of dry ice and methanol. A DC voltage source provided the current. The cathode was a platinum sheet with a surface area of approximately 3213 mm^2. The cathode was placed approximately 20 mm from the specimen surface. The typical polished surface area was 200 mm^2. Polishing times and voltages were determined by trial and error. Typically these were 70 volts for 3 minutes. Once polishing was completed, the samples were etched, in a solution of 5 vol./o HF, 5 vol./o HNO_3, and water. This etch attacks TiAl more aggressively than Ti_3Al as observed by noticing a polished, unetched, two phase, TiAl alloy's surface in the backscatter mode on the SEM and comparing it to the same area after etching. The TiAl phase is severely attacked and the Ti_3Al phase is slightly attacked. After SEM characterization, optical evaluations were performed and grain sizes estimated.

Microhardness determination involved the use of a Leco automated microhardness tester using a diamond pyramid indenter with a load of 200 grams and a dwell time of 10 seconds. This load was chosen in order to allow the indent to be contained inside the grains while still being heavy enough to be load independent. Originally the hardness of the individual phases was to be tested. However, after testing many samples in this manner, it proved to be too tedious and time consuming. Consequently, bulk hardness measurement were made by taking hardness readings at random areas on the specimens. Ten readings were taken and corrected using calibration blocks. An average and 1σ standard deviation were determined. This average was quoted as the hardness of the material. The hardness indents were observed for signs of slip.

Since hardness indentation produces a complex stress state with both compressive and tensile components, slip lines around the indents indicate possible tensile ductility. The number of indents for a given sample with slip lines was used as a qualitative estimate of tensile ductility. This was used in helping to determine the quaternary alloy compositions.

Slices of approximately 1.4 mm were cut from the homogenized ternary alloy buttons using a diamond cut off saw. These slices were clamped into a vice and bent to fracture. Care was taken to note the tension side of the slice. The slice remaining in the vice was observed for signs of cracks occurring around the compression marks. This gave an indication of the compressive behavior. The fracture surface was characterized in the SEM. The tension side of the fracture surface was used to qualitatively rate the ternary alloys based on the perceived ductility.

By observing the fracture surface for signs of ductility, the hardness indents for signs of slip bands, and determining the number of phases present, a rough qualitative system for comparing ductility of the ternary alloys was derived. From this system, to be discussed later, eight compositions were decided to merit further investigation. These eight were zone processed, homogenized, and sectioned into four point bend specimens. These specimens were then tested in four point bending on a 2500 Kip Interlaken Testing machine.

Levitation zone processing was employed in order to produce ultra pure, completely sound, bend specimens. Zone processing has the added attribute of producing a uniform composition once steady state has been achieved. This was another advantage of producing bend specimens via zone processing. In addition, zone processing involves a very slow cooling rate in comparison to traditional casting techniques. This encourages an equilibrium structure to form during zone processing. Because of the ordering that results in γ based materials, non equilibrium structures often appear in traditional casting procedures.

The zone processing conditions for all eight ingots were the same. These entailed an extremely pure atmosphere and a controlled solidification rate. The atmosphere was ultra pure He. The solidification rate was controlled at 19 mm/hr. The levitation zone processing unit employed in this research is computer controlled and involves controlling the shape of the liquid zone [44]. For this research, all tuning parameters, in the computer control program, were held constant in order to minimize the introduction of any unknown variables as a result of differences in processing. The final manipulated variables for this zone processing unit were the rotation rate of the freezing solid/liquid interface and its rotation direction. The rotation rate was chosen to be 100 R.P.M. in the counter clockwise direction (CCW). This rotation rate produced added mixing of the liquid zone which encouraged a more uniform melt composition, and consequently, a more uniform solid composition. The rotation direction was chosen because it was observed that in the CCW direction the two phase lamellar structure, which was present in all alloys upon zone processing, aligned parallel to the length of the ingot. When the zone was rotated clockwise the lamellae had a spiral orientation. It was felt that this spiral orientation might introduce an unwanted variable. The processed portion of these ingots was 25.4 mm in diameter and 70 mm in length. This allowed approximately six rectangular bend specimens with dimensions of 40x8x6 mm^3 to be electrically discharged machined (EDM) from the processed region. These specimens were tested in the 6 mm direction in order to minimize constraint caused by specimen size. The specimen size was chosen to yield a more representative bulk property measurement. Most measurements in the literature are performed on thinner samples, less than 1.5 mm. In addition, this larger size allowed easier polishing and handling as well as enough material to get below any EDM damage. After polishing, the typical specimen dimensions were 40x7x4 mm^3.

The bend specimens were heat treated according to the heat treatment described above. After heat treating, they were polished through 2400 grit SiC. A final polish with 240 grit paper was

used making sure that the polishing direction was parallel to the tensile axis. The polish through 2400 grit was used to get below the EDM damage and the critical flaw size, which was estimated to be approximately 40 μm. This corresponds to roughly to the width of the scratches produced by 14 μm diamond paste (equivalent to 600 grit SiC). Consequently, if the scratches are below this level, failure should not occur due to critical flaw size. The critical flaw size was estimated by using the K1 equation for four point bending, the minimum reported K1 value for TiAl, 10 MPa$\sqrt{m}$, the sample size, and the fracture load previously determined on TiAl based samples. The final polishing step was employed because it was observed that the strain gages remained glued to the specimen only if the surface roughness was of this level.

The strain gages were glued to the middle of the polished specimen on the surface which was subjected to the maximum tensile stress. Before installation, these surfaces were properly cleaned, degreased, and neutralized as per the instruction of the gage manufacturer [45]. The gluing procedure also followed the manufacture's instructions. Gluing and surface cleanliness were the most important factors in successful strain gage bonding. The strain gages chosen had a gage length of 6.35 mm, an overall width of 4.57 mm, and an overall length of 11.43 mm. This size was chosen because it was within the inner span length of the four point bend jig and fit the specimen dimensions. The resistance of these gages was 350 ohms. This resistance was chosen upon the advice of the strain gage manufacturer. They indicated that higher resistance gages produced a lower rate of heat generation for a given applied voltage when compared to a smaller resistance gage. In addition, the manufacturer's information indicated that larger resistance gages produced a decrease in leadwire effects as well as an improvement in the signal to noise ratio, when these were compared to smaller resistance gages. Once the gages were affixed, leads to a bridge completion module were installed. Leads from this module to the Interlaken completed the circuit. This balanced bridge yielded a voltage

signal which represents resistance changes in the strain gage. These voltage signals were read by the Interlake's computer system and converted into a change in length measurement for the strain gage. Once a given gage was installed in the unstrained condition, the measured length change on the Interlaken was zeroed. Next, shunt calibrated resistors, which corresponded to a known percent strain measurement, were individually placed in parallel with the strain gage to simulate a resistance change. This was converted by the Interlake's computer to a length change. This length change and the gage length of the strain gage were used to calculate the measured percent strain for a given shunt. By using 1.0% , 0.5%, 0.1%, and 0.05% strain calibrated shunt resistors and their corresponding measured percent strain, a plot of measured strain versus actual percent strain was made. The percent strain measured by the strain gages was corrected for system error, from the equation of this plot.

The test specimens were subjected to four point bend testing with a 2200 Kip Interlaken testing machine using a four point bend jig on loan from the High Temperature Materials Laboratory at the Oak Ridge National Laboratory. The Interlaken was equipped with a 2500 lb. calibrated load cell. The testing machine was hydraulic and computer controlled. For this testing, the control scheme involved the use of a proportional controller to control crosshead movement. Strain rate control was what was ultimately desired. However, this was extremely difficult to implement on this equipment. Consequently, crosshead control was used to approximate strain rate control. The jig used was designed such that the specimen was self aligning with the loading axis. The inner span width was 15 mm and the outer span width was 30 mm. The lowest practical crosshead movement rate was used. The strain rate, as determined from the plots of percent strain versus time, was from 0.00001 to 0.00009 ε/sec. The load and change in length of strain gage (ΔL) were recorded. The percent strain was calculated from $\% \varepsilon = (\Delta L / L_0)\ 100$, where Lo was the gage length of the strain gage, 6.35 mm. The outer fiber stress was calculated from a simple beam equation for four point

bending. This equation is

$$\sigma_f = 3/4 * load * span / [b^2 * w]$$

σ_f = outer fiber stress at fracture in psi

load = load at fracture in lbs.

span = span width = 1.2 in (30 mm)

b = specimen dimension in loading direction

w = specimen width perpendicular to the plane of loading

A minimum of three samples for each composition was used to determine an average outer fiber fracture stress and an outer fiber fracture strain. A 1σ standard deviation was also calculated for these values. The percent fracture strain and outer fiber fracture stress were used to evaluate which alloys had the best combination of ductility and strength.

Three of the ingots zone processed in this research produced enough extra bend specimens to also perform fracture toughness testing. The specimens used for this test were of the same dimensions as that of the four point bend test specimens. However, these specimens were tested in the direction 90^0 to that of the four point bend test specimens (i. e., in the 8mm direction). These dimension do not conform to ASTM E-399, which is the K1c testing standard. The specimens required in this standard are too large to be feasibly produced by zone processing, (i. e., thickness and width greater than 10 and 23 mm, respectively) using the current equipment. Consequently, this test yielded K1 values and not K1c values. A notch of approximately 2mm was cut into the center of each of the specimens with a diamond cut off saw equipped with a wafer which had a 2 mm smaller radius than the diamond blade. The actual notch size was measured after fracture using the filar eye piece on a microhardness

tester. The same four point bend jig was used for this test. The load and the machine displacement, corrected for machine deflection, were recorded. The outer fiber stress was calculated in the same manner as above. The outer fiber strain was calculated using an equation derived for four point bending assuming elastic behavior and assuming that the machine displacement is measured at the span/4 points (i. e., at the inside rollers). This equation is

$$\varepsilon_{max} = 6*w*Defl / span^2$$

w = the testing dimension = 8 mm

Defl = machine deflection measured at span/4 points

span = outer span dimension = 30 mm.

A plot of outer fiber stress verse outer fiber strain was made and observed for any signs of deviation from non-linearity. Non-linearity would indicate that not enough constraint was involved to insure that the specimen failed under plane strain conditions. Consequently, this would not be a fracture toughness measurement. In all cases, these plots showed only linear behavior. This supports the argument that these samples failed under plane strain conditions and thus a valid K1 value resulted. The fracture surfaces were also observed to make sure no signs of ductility were seen. Again, for all cases the fractures were fully brittle. Three specimens were tested for each composition and a K1 value calculated. An average and a 1σ standard deviation were also determined. K1 was calculated from the following equations which assumed four point bend loading.

$$K1 = Y \{ [6*M*a^{1/2}] / b* w^2 \}$$

$$Y = 1.99-2.47(a/w)+12.97(a/w)^2-23.17(a/w)^3+24.8(a/w)^4$$

M = maximum bending moment

b = 6 mm

w = 8 mm

The fracture toughnesses were compared to literature values and to that of the binary composition. This was used to see if alloying improved the fracture toughness.

After mechanical testing and polishing, an SEM characterization was performed on each sample with the best ductility from each of the eight alloys. The number, volume fraction, and composition of each phase present was determined via the above described SEM procedure on the polished tensile surface of these samples. The EDX analysis on these samples was not as accurate as for the binary alloys, since standards for the ternary and quaternary alloys were not available. Consequently, the compositional EDX analysis of the ternary and quaternary alloys was at best +/- 1 a/o. The polished surface of each of these samples was then etched and an optical characterization performed. Special attention was paid to the structure at the fracture surface in order to correlate the fracture surface with the microstructure. The fracture surface of the halves, whose polished surface had not already been analyzed, were examined in the SEM. Attention was paid to the tension side of the fracture surface for signs of ductility. An attempt was made to correlate the fracture surface with the microstructure.

Since small amounts of impurities affect the mechanical properties of TiAl based alloys, an analysis was performed at NASA Lewis to determine the dissolved carbon (C), nitrogen (N), and oxygen (O) levels in representative homogenized samples. Compositions produced by each of the three casting techniques arc melting, drop casting, and zone processing, were analyzed. The sample from the zone melted ingot was taken from the same region where the bend bars were sectioned, in the middle of the ingot's length, in order to have a representative

measurement of impurity content in the bend specimens. The analyses were obtained in order to estimate the typical impurity levels produced upon casting and homogenizing. O and N were determined in a LECO gas chromatograph. In this technique, samples, which weighed from 0.1 to 1 gram, were reacted with carbon via a helium carrier gas by heating in a graphite crucible to temperatures in excess of 2700 C [46]. The nitrogen, hydrogen, and carbon monoxide formed pass through a copper oxide furnace where hydrogen and carbon monoxide were converted to water and carbon dioxide, respectively. This water was then removed by a drying agent, while the nitrogen and carbon dioxide were separated by a chromatographic column and passed through a thermistor detector. The thermal conductivity difference of helium, nitrogen, and carbon dioxide are proportional to the nitrogen and oxygen content in the sample. This results in a determination of the dissolved nitrogen and oxygen levels in the sample. This technique had the advantage of being able to simultaneously determine the N and O levels. These levels can be determined regardless of chemical species in which they were a form. The technique can detect concentrations from 1 to 1000 ppm by weight and has an accuracy of +/- 5 to +/- 20 percent for levels above 10 ppm. The dissolved C levels were determined by a combustion technique using an infrared cell for analysis of the evolved gas. The analyzed samples, weighing from 0.1 to 2 grams, were combusted in an alumdum crucible in flowing oxygen. Carbon was converted to carbon dioxide (CO_2) and carried by the oxygen carrier gas through an infrared detection cell where the amount of CO_2 was measured. This technique can detect levels from 3 ppm to 35 % . For a 1 gram sample, the accuracy is +/-0.002 for C exceeding 10 ppm.

In order to better understand the effects of alloying on the mechanical properties of TiAl, a study was undertaken to determine the substitutional behavior of the ternary additions. This involved a technique developed in the mid 1980's called ALCHEMI. Atom Location by Channeling Enhanced Microanalysis (ALCHEMI) involves the phenomena of electron channeling which

results from the dynamic interaction of an incident beam of electrons with a periodic crystal potential. For orientations near the strong diffraction conditions, the incident plane wave of electrons sets up standing Block waves in the crystal lattice. By assuming that the incident plane wave can be represented by a two beam condition, superposition of the beams produces a Block wave with the maximum always occurring at either the atom planes or halfway between the atom planes; which location depends upon the orientation of the incoming electron beam. By choosing the appropriate reflections, the wavelength can be chosen such that its maximum always occurs at every other atom plane, either Al or Ti planes only. These standing wave maxima enhance x-ray fluorescence of one plane relative to the other. By observing the x-ray spectra for trends between the peaks for the alloying element, Ti, and Al, the substitutional behavior of the alloying element was determined. In order to enhance channeling effects, axial channeling was employed as opposed to planar channeling. Axial channeling involved the incident electron beam being directed along a zone axis (e. g., [001]). For this condition strong variations in characteristic x-ray intensity are observed for small changes in crystal orientation. These effects are much larger for axial channeling than with planar channeling, consequently leading to higher sensitivity levels for the axial channeling condition [47].

The ALCHEMI technique involved used EDX on a 200 KeV H-800 scanning transmission electron microscope (STEM) equipped with an LaB_6 filament. X-ray spectra were obtained in the exact and few degrees off of the exact channeling conditions. These spectra were corrected for background and used to calculate the fractional Al and Ti site occupancy of the alloying element. The calculation employed involved a statistical method which uses a standard multivariant analysis. This analysis assumes that the counts of the alloying element are a linear combination of the counts of Al and Ti. The analysis yields a best fit and an uncertainty in fit of the data.

Three arc melted and homogenized alloys were analyzed using ALCHEMI: a Zr ternary alloy, a Cr ternary alloy, and a Mn ternary alloy. The remaining ternary additions, Ga and Ag, were not analyzed. The Ga ternary alloy was not analyzed because the substitution behavior of Ga in TiAl is well documented. The Ag alloy was too brittle to section STEM samples; therefore, it was not analyzed. The ternary alloys analyzed had a composition of Ti-50/Al-48/Zr-2, Ti-48/Al-49/Cr-3, and Ti-47/Al-51/Mn-2, in atomic percent, as determined by EDX on the SEM. These compositions were used to represent the substitution behavior of Zr, Cr, and Mn. Each sample was observed in BS to determine the number of phases present. The Zr and Mn alloy were determined to be single phase. The Cr alloy was slightly, 1 volume percent, two phase. However, it was felt that this would not offer too much of a complication as long as the STEM specimens analyzed were single phase. Several thin discs were sectioned from each of the above alloys using a diamond cut off saw. These discs were ground using standard polishing techniques and electropolished in a twin jet unit until perforation occurred. The polishing solution employed was composed of 10% perchloric acid and 90 % acetic acid, held at 25 C. Each specimen was observed in a transmission electron microscope (TEM) and the orientation indexed. Low index specimens were used for the channeling experiments. These specimens were observed in an STEM using an LaB_6 filament at an accelerating voltage of 200 KeV. The LaB_6 filament was utilized because for the same voltage it produced a smaller spot size in comparison to a tungsten filament. EDX spectra were produced for the exact and slightly off the exact conditions. The counting times of 400 seconds or longer were employed to produce counts for the alloying elements above 1000. The alloying element's counts had to be above this level to minimize the background to signal ratio. Once at least 12 spectra were taken for each composition, the spectra were analyzed according to the previously described scheme.

III. RESULTS

The results of this research will be discussed in sections. These sections are:

1. Impurity Analysis,
2. Atom Location,
3. Binary Phase Boundary,
4. Ternary Phase Boundary,
5. Hot Working,
6. Homogenized Hardness,
7. Quaternary Compositions,
8. Bend Test and Microstructural Results,
9. Evidence of Ductility, and
10. Comparison of Current Results to Those Given in Literature.

1. IMPURITY ANALYSIS

The dissolved impurities of O, C, and N are known to affect the mechanical properties of TiAl. Additional, α_2 is stabilized by dissolved O and N [46]. Since the objective of this research was to produce low Al single phase alloys of improved ductility, it was decided that the impurity levels should be determined in representative samples in order to insure that the properties were due to alloying and not to impurity content. As previously stated, these samples were analyzed after homogenization. A sample from each of the three casting techniques was analyzed. The results are shown in table 5. These analyses are low compared to published values [5].

The C and O levels produced in arc melting are the highest of the three techniques. This may

be attributed to the atmosphere for the arc melter not being as pure as that of the other processes due to machine limitations. However, these levels are of the order of those reported in literature. The O levels produced in the other techniques are much lower than those reported in literature, 370 to 500 ppm [5]. Since O in TiAl is an α_2 stabilizer at levels above 400 ppm and all bend specimens were produced by zone processing, the second phase that results in these samples (discussed later) was probably not due to the O levels. All of the C levels were less than 100 ppm. There is no published evidence that suggest that at these levels the mechanical properties will be affected. The N levels in all these samples were extremely low. These levels are below those for which the literature indicates will cause nitride precipitation (i. e., 40 ppm for single phase γ alloys [45]) and the associated effects on mechanical properties.

2. ATOM LOCATION

ALCHEMI was employed to determine the site occupancy behavior of Cr, Mn, and Zr in single phase TiAl. Published work indicates that Ag and Ga substitute for Al in TiAl and that the substitution behavior for Mn in TiAl is not obvious [47,48]. Hashimoto et al. report that in TiAl Mn substitutes for Al [49]. While Babu et al., report that up to 1.8 a/o Mn, substitution is for Ti in TiAl, beyond this amount random substitution behavior is reported [50]. Published data indicates that Cr and Zr substitute randomly and for Ti, respectively [51,49]. Because of the discrepancies over Mn substitution and the promise of ductility showed by alloys of Cr and Zr, verification of the substitution behavior of Cr, Mn, and Zr was determined on representative alloys produced in this research. In all of the above references, the ALCHEMI data were calculated by a ratio technique, which involved differences in counts between channeling and nonchanneling orientations. According to Rossouw, this calculation technique amplifies errors when channeling effects are small and is more sensitive to delocalization effects [52].

Delocalization is an effect which occurs when the maxima of the standing wave does not coincide exactly with a lattice plane, resulting in changes in x-ray generation. Additionally, delocalization occurs when x-ray generation is nonlocalized to specific lattice planes resulting in spurious x-ray transmission. Both delocalization and error amplification can lead to significant errors. The multivariant technique, employed in this research, is less sensitive to delocalization and numerical propagation errors than the ratio method [52]. In addition, this method yields a measure of " experimental uncertainties in both the impurity concentration and in the distribution of the impurity (Cr, Mn, and Zr) over lattice sites " [52]. In all of the reported literature results no indication was given of the data scatter, standard deviation, so that an estimate of true trend could not be determined. In the multivariant technique, the data scatter is given as the experimental uncertainty and allows a better handle to be derived on the substitutional behavior. In this technique, the counts of the impurity are assumed to satisfy a χ^2 distribution and are a linear combination of the counts for Al and Ti

$$N_{imp} = \Sigma \alpha_i N_i$$

where N_{imp} is the impurity count and α_is are the coefficients and their errors determined by the multivariant analysis for each EDX spectra [53]. N_is are the counts of Al and Ti for each spectra. For m separate EDX spectra and v {(number of site locations)*(number of impurity species)} fitted α_is, the criterion v < m must be satisfied [53]. The α_is are determined by a standard χ^2 minimization technique, after which, the concentration of the impurity, c_p, and the fractional occupancy, f_i, are determined by the following:

$$c_p = \Sigma \left[\alpha_i n_i / k_i\right] / \left[1 + \Sigma \alpha_i / k_i\right]$$

$$f_i = 1/c_p \left[\alpha_i n_i / k_i\right] / \left[1 + \Sigma \alpha_i / k_i\right]$$

where n_i and k_i are the number of host sites, 2 (Ti and Al), and the k factor ratio,

respectively. The k_i factor ratio is the ratio between the unknown, i, and standard x-ray intensities determined for the STEM used. This is given by the following:

$$k_i = C_{Si} * I_i \; / \; I_{Si} * C_i$$

where C_{Si} and C_i are the concentration of a silicon standard and the unknown, respectively [54]. I_{Si} and I_i are the intensities of the silicon and the unknown, respectively. The theoretically calculated k_i values using the H-800 STEM are given in table 6.

For each STEM specimen analyzed, an [001] direction was located with the aide of bend contours and the corresponding diffraction pattern. Figure 7 shows typical bend contours. Sites A, B, C, and D are locations where EDX analyses were performed for the off channeling condition. Site E is the location where the exact EDX analysis was performed for the channeling condition. For a given composition, at least three STEM specimens were analyzed. The intensities for Ti, Al, and the impurity element for each spectra, A-E, where corrected for background and the ratios of the intensity for the Ti kα peak to the Al kα peak were determined. If the ratio Ti_k/Al_k for the off channeling condition is not greater than approximately 30% of that of the channeling condition, then there is not enough difference between the channeling and off channeling conditions to employ the ALCHEMI technique (i. e., the delocalization effects are too large). For these cases, the data set would be ignored. Once at least 12 acceptable spectra were obtained, the intensity data were analyzed using the above equations to determine the site occupancy behavior and the concentration of the impurity element. Table 7 gives the results for the three compositions considered and the corresponding standard deviations. The compositions as determined from SEM EDX are given in atomic percent as Ti-48/Al-49/Cr-3, Ti-48/Al-50/Mn-2, and Ti-49/Al-49/Zr-2.

The standard deviation indicates not much scatter in the readings. The calculated composition of these alloys is in agreement with the composition as determined by SEM EDX. Figure 8

shows plots for impurity x-ray counts versus $\Sigma\alpha_i N_i$. These graphs show a linear relationship between impurity counts and Al and Ti counts, in agreement with the assumptions used with the multivariant analysis. The lack of data scatter, the agreement in calculated and measured compositions, and the agreement of x-ray counts with the model assumed by the multivariant technique yields credibility to the results from the multivariant analysis. From these results, Cr has a tendency to occupy Al sites, Mn substitutes randomly, and Zr occupies only Ti sites. The Zr trend compares well with literature values. Both the Mn and Cr data conflict somewhat with the literature values. All of the literature results employed a ratio technique and did not quote standard deviations. Therefore, there is no way to determine the variation in results. Additionally, the work of Hashimoto and Babu were performed using x-ray diffraction with a diffractometer [49,50]. Because of the size of the specimens used in this technique, bulk values are generated as compared to specimens analyzed in the STEM. When bulk samples are analyzed, they encounter florescence and adsorption problems, which are not present in thin STEM specimens. These bulk florescence and absorption problems have been seen in binary TiAl alloys when SEM EDX analyses were performed. The lack of standard deviation data and the known problem with florescence and absorption may be another cause for the difference between this work and that of Hashimoto and Babu.

The work by Mohandas and Beaven employed axial channeling techniques to analyze the substitution behavior of Mn and Cr in TiAl [51]. They employed the ratio technique to determine that for a Ti-45/Al-53/Mn-2 alloy, 97% of the Mn substituted in the Al sites. For a Ti-47/Al-51/Cr-2 alloy, 57% of the Cr substituted for the Al sites. This is extremely puzzling, since when the raw data in this report was recalculated using the ratio technique, it was found that the substitution behavior of Mn and Cr was 37% (+/- 5%) and 65% (+/- 5%) in the Al sites, respectively. This data is in line with the 50% (+/- 3%) and 75% (+/- 2%) determined by the multivariant technique, but is inconsistent with the Mohandas et al.

work. This discrepancy is probably not due to the slight composition difference between the Mohandas work and this research, because, there is no indication either in literature or from this research that composition has a significant result on substitution behavior of alloying elements so long as the alloy remains single phase. Spence et al. warns that if the impurity is not statistically uniform throughout the depth of the specimen, then ALCHEMI may lead to incorrect results [55]. Since the samples in this research were homogenized for 100 hours at 1100 C, they most likely have a uniform composition and the problem Spence et al. warns of is not present. This seems true especially since all evidence of the cast structure has been removed as determined by optical and SEM examinations. When the Mn and Cr work was first examined, a 150 second counting time was used to determine the EDX spectra. Using this counting time and the ratio technique to calculate the fraction of Al sites occupied by the alloying additions, the averages (standard deviations) for Mn and Cr were 37% (+/- 30%) and 58% (+/- 30%), respectively. With such a short counting time, the intensity peaks for Cr, Mn, and Zr were too close to the background intensity for statistically correct measurements to be determined, as seen by the large standard deviation for these numbers. Once the counting time was increased to 400 seconds, the statistical variation reduced, to +/- 5% for Mn and Cr. Mohandas et al. did not indicate the counting times used to determine their EDX spectra. If it was as low as 150 second, they possibly could have too much noise in there answers to see a true pattern.

3. BINARY TiAl PHASE BOUNDARY

Because of the controversy over the $\alpha 2 + \gamma / \gamma$ phase boundary, a study was performed to determine its location under the conditions used in this research (i. e., cooling rate, processing nature, and impurity content). This was accomplished by trying to produce a near-equilibrium, two phase structure at 600 C. The alloy chosen for study had a nominal

composition of 45 a/o Al. This alloy was arc melted and homogenized according to the previously described procedures. The cooling procedure consisted of furnace cooling to 800 C and holding for three hours followed by further furnace cooling to 600 C and holding for three hours. The encapsulated sample was next quenched in air to room temperature. Three specimens were sectioned from this sample and each reencapsulated in quartz tubing with a 790 Pa Ar pressure. These specimens were placed in a 600 C furnace for 7, 97, and 997 hours, respectively. Each of these samples was at 600 C for a total of 10, 100, and 1000 hours. It was originally felt that diffusion in ordered alloys would be slow at temperatures below 600 C; therefore, the 600 C boundary information, given by these four alloys, would be indicative of the phase compositions at room temperature. The resulting structures ($\alpha 2$ and γ) and compositions for these homogenized alloys were analyzed using EDX and backscattered imaging on the SEM. Table 8 gives the compositions and volume fractions of the phases present in these homogenized alloys. The volume fractions were determined using two techniques: a simple lever rule using the nominal composition of 45 a/o Al and a histogram technique previously described (pg. 29).

From the data in table 8, it is seen that the boundary does not change with time at 600 C and has a composition of 47.2 a/o Al (+/- 0.9%) and 39.0 a/o Al (+/- 0.9%) for the $\alpha 2 + \gamma$ / γ and $\alpha 2$ / $\alpha 2 + \gamma$ boundary, respectively. The volume fractions as determined from the two techniques is fairly consistent. This too does not change appreciably with time at 600 C. The maximum solubility of Al in α_2 and γ at the eutectoid (1115 C) is given in literature as 38 a/o Al and 48 a/o Al, respectively [21]. This is extremely close to the value obtained from this heat treating study of 39.0 a/o Al (+/- 0.9%) and 47.2 a/o Al (+/- 0.9%), respectively. It can either be concluded that the $\alpha 2 + \gamma / \gamma$ boundary is vertical or that diffusion is so slow in these alloys at temperatures below 1115 C that for all practical purposes phase transformations have stopped. If diffusion is too sluggish for phase

transformations below 1115 C, the phase boundaries given by this 600 C heat treating study are really those at 1115 C and not those at 600 C. Diffusion data for Ti in single phase TiAl indicates that diffusion is extremely sluggish at temperatures below 1100 C [56]. According to data from the work of Mehrer et al. , the diffusion coefficient for Ti in TiAl at 1100 C and 600 C is $1x10^{-15}$ m^2/s and $6x10^{-22}$ m^2/s, respectively [56]. As an estimate of diffusion distances traveled at 1100 C and 600 C the general diffusion equation of $x=\sqrt{Dt}$ is employed, where x is the diffusion distance, D is the diffusion coefficient, and t is the time. At 1100 C, Ti will diffuse 20 μm in 100 hours TiAl. This distance is approximately ten times the distance (2 μm), estimated from the cast microstructures, for Ti atoms to move in order to remove the segregation caused by casting. At 600 C, for 1000 hours the diffusion distance is approximately $5x10^{-2}$ μm. This small distance at 600 C suggest that diffusion is too sluggish for phase transformations to have occurred at 600 C.

The C, N, and O analysis of this alloy has been previously given in table 5 as 86, 13, and 603 ppm, respectively. The O level is above that given in literature, 400 ppm, to cause precipitation of $\alpha 2$ [5]. This does not appear to have appreciably occurred, because if this were the case, the $\alpha 2 + \gamma$ field would have been extended to higher Al contents. If anything, the $\alpha 2 + \gamma / \gamma$ field is lower in Al than the quoted literature composition of 48 a/o Al for this phase boundary [21].

4. TERNARY PHASE BOUNDARIES

The goal of this research was to try to extend the γ single phase field to lower Al contents by alloying TiAl with ternary solute additions. To this end, the elements chosen to make the ternary alloys were Ag, Cr, Ga, Mn, and Zr. The effects of the alloying addition, x, and Al content on the γ boundary were determined by observing the number and composition of the phases that resulted after arc melting and homogenizing. The homogenizing scheme employed

was that previously described. These ternary alloys were subjected to the same heat treatment as that used in the binary phase boundary study described above. From the results of this latter study, it was determined that below 1115 C phase transformations have essentially ceased. Even though the binary alloy was subjected to a cooling rate which took 6 hours to achieve room temperature, the structures present are most likely those at 1115 C. The samples shown in figures 9, 12, 13, and 15, were also cooled in the same manner as described above. Hence, the phase compositions of these alloys represent approximately the 1115 C ternary phase boundaries for Ag, Cr, Mn, and Zr. The number of phases and their compositions were determined via backscattering and EDX on the SEM. For a given ternary alloy, these phases, their number, and composition were used to construct an isothermal section. The tie lines, dotted lines in figures 9-10 and 12-16, for a two phase field were constructed between the matrix and the second phase. This allowed the phase fields to be sketched out.

Figure 9 shows the ternary 1100 C isotherm for the TiAl+Ag series as a result of this work. This figure shows that Ag additions do not shift the $\alpha 2 + \gamma / \gamma$ boundary appreciable. Additionally, it is seen that Ag has less than 3 a/o solubility in TiAl. Once this solubility is surpassed, an FCC Ag-Al solid solution is formed. This phase precipitates mainly at the grain boundaries of the gamma matrix. This ternary isotherm is consistent with that published by Hashimoto et al. for a 800 C isotherm, figure 10 [47]. The 1100 C diagram shows the γ phase field does not extend to as low Al contents as the 800 C γ field does. This is not necessarily an inconsistency since the solubility could decrease with increasing temperature. Both diagrams show that a Ag-Al solid solution forms at Ag levels higher than approximately 3 a/o. Hashimoto et al. indicate that the maximum solubility of Ag in TiAl is approximately 3 a/o. At first glance, this was consistent with the result of approximately 2 a/o Ag found from this research. However, two alloys of the same composition, Ti-50/Al-48/Ag-2, but different

hardnesses { 171 DPH (+/-20) and 225 DPH (+/-30)} were determined to be single phase by backscattering. Because of the hardness differences, these samples were analyzed using convergent beam electron diffraction (CBED). Fine second phase particles, as seen in figure 11, were observed. The alloy with the higher hardness had a higher concentration of second phase particles. During homogenization the higher hardness alloy experienced a +/- 40 C temperature oscillation due to temperature controller problems. This oscillation put this sample in a temperature range where the solubility of Ag in TiAl was lower; consequently, resulting in more precipitates being formed. In order to determine if these particles were produced upon cooling or as a result of the homogenization, a specimen from the cast alloy of each of these samples was heat treated again at 1100 C for 100 hours, but was water quenched after heat treating. Again these samples were observed in CBED and the second phase was observed. In order to determined if these particles would ever coarsen large enough to be seen in backscattering, a heat treating study at 600 C was under taken. At the time when this study was undertaken, it was still felt that at 600 C diffusion was still occurring at a fast enough rate to produce coarsening and phase transformations. In this heat treating study, the homogenized alloy with the most precipitates was sectioned into four samples. Each sample was held at 600 C for different times (3, 10, 100, and 1000 hours) and water quenched to room temperature. The samples were analyzed in the SEM for composition and number of phases. From backscattering, all samples were still single phase, even after being held at 600 C for 1000 hours. This again supports the argument that diffusion is too sluggish at 600 C for coarsening or phase transformations to occur. These particles were not seen in backscattering, even after being homogenized at 1100 C for 100 hours, suggesting that Ag is practically insoluble in TiAl.

Figure 12 shows the effects of Cr additions on TiAl. Cr like Ag has limited solubility in TiAl. Even at levels as low as 0.4 a/o a small precipitate forms. This precipitate is basically α_2

with dissolved Cr and forms mainly at the grain boundaries. Cr additions appear to shift the $\alpha 2 + \gamma / \gamma$ boundary toward higher Al contents as judged by the tie lines for the $\alpha 2 + \gamma$ phase field. This trend suggests that Cr substitutes for Ti, (i. e., more effective Ti present). The ALCHEMI results refute this point by determining that Cr substitutes mainly for Al. Indicating that relying solely on the phase boundary trends to predict substitution behavior is unreliable.

The Ga ternary phase diagram was not fully investigated because of time constraints. Based on the few single phase ternary alloys that were produced, Ti-51/Al-47/Ga-2 and Ti-49/Al-46/Ga-5, the $\alpha 2 + \gamma / \gamma$ boundary was observed to shift to lower Al contents. This is seen because the binary $\alpha 2 + \gamma / \gamma$ phase boundary has an Al content of 49 a/o compared to ternary compositions being single phase with Al contents of 47 and 46 a/o Al, respectively. This boundary shift is consistent with the substitution behavior of Ga for Al in TiAl [48].

Figure 13 shows the phase boundary relationships for TiAl + Mn alloys. Mn additions appear not to effect the $\alpha 2 + \gamma / \gamma$ boundary as judged by the tie lines for the $\alpha 2 + \gamma$ field. This is consistent with the ALCHEMI results which indicate random substitution. Figure 14 shows the Mn ternary isotherm determined by Hashimoto et al. [57] for 1000 C. The $\alpha 2 + \gamma / \gamma$ and $\alpha 2 / \alpha 2 + \gamma$ boundaries are consistent with this work. However, the Hashimoto reports that a Al rich third phase ζ forms at Mn levels around 5 a/o and Al levels less than 50 a/o. For this work, at these composition levels, it was found that a Ti rich phase, Ti-56/Al-30/Mn-15, was formed. Unfortunately, there is not enough data in this region to investigate this discrepancy.

Figure 15 shows the experimental results for the additions of Zr to TiAl. Zr additions shift the $\alpha 2 + \gamma / \gamma$ boundary to higher Al content, more effective Ti, as perceived from the $\alpha_2 + \gamma$ field tie lines. This boundary shift is consistent with the substitution behavior found from

ALCHEMI, Zr replaces Ti. The experimental work compares well with the work by Hashimoto et al. for 1000 C, figure 16 [57]. Both the $\alpha 2 + \gamma / \gamma$ and the $\alpha 2 / \alpha 2 + \gamma$ boundaries are consistent with this research.

5. HOT WORKING

An attempt was made to hot work these samples in order to reduce the grain size. Small grain sizes are known to favor improved ductility in TiAl based alloys. The first approach consisted of encapsulating a Ti-49/Al-49/Zr-2 cast alloy in a stainless steel container, which was sealed by vacuum welding. This sample was soaked at 900 C until the sample assembly had a uniform temperature. The 900 C temperature was chosen because this temperature is approximately 60% of the absolute melting temperature, 1500 C. Typically, in this temperature range, significant recrystallization occurs. 900 C is also above the ductile-brittle transition temperature (DBTT). This sample was hammer forged between two cold platens. This was unsuccessful because for this piece of equipment there was no way to control the amount of deformation to the sample. This sample was reduced by 90% in the center and 60% at the edges. Because of the excessive non-uniform deformation and the presence of cracks, no bend sample could be machined. The cracks may have been caused by a synergistic effect of the extreme deformation and rapid heat loss due to the cold platens. Because of the non-uniform deformation produced by hot forging, hot rolling was employed. Hot rolling is a more uniform and controlled deformation process. A cast Ti-49/Al-46/Ga-5 alloy was wrapped in stainless steel foil and encapsulated under vacuum in an Inconel 750x container via electron beam welding. Inconel 750x was used as a container instead of stainless because at 900 C the yield strength of Inconel 750x is approximately that of TiAl based alloys, 150 MPa [13]. There was no noted problem with the stainless steel, but in order to minimize possible problems the inconel was used. The Ga alloy was soaked in a 900 C furnace for 3 hours to

insure a uniform temperature. The first several passes did not impart much deformation to the assembly and were only used to level the surfaces. After the sample's surfaces had been leveled, the next few passes reduced the thickness less than 0.1%, which started breaking down the original structure. After each pass the sample was rotated 90° to the previous rolling direction and rolled again. The rolls were then moved closer to one another for the next set of rolling passes. Between each pass the sample was placed in the 900 C furnace until the color was again uniform, approximately 10 minutes. After the initial passes, the sample was reduced approximately 0.6% per set of passes (i. e., rolled twice, rotating 90° each time, with the same roller setting). A total reduction of 10% was achieved. When the sample was examined metallographically, the cast structure had started to break down; however, it was not fully removed. The cast structure was much finer than the structure resulting from rolling. Typically, when the amount of deformation is small, excessive grain growth problems occur due to too few nuclei, recrystallized grains, being present to compete with one another. Another problem, making it difficult to produce a fine grain structure, is the presence of dynamic recrystallization, which occurs in these alloys. Since strain free grains form quickly, they will start growing sooner, thus minimizing competition between nuclei. In order to fully remove the cast structure and produce a fine grain size, it is estimated that a least 30% thickness reduction is needed; typically, below this amount, excessive grain growth is still a problem.

A macroscopic examination of the rolled surface revealed large surface cracks. Because of the cracking, rolling should have been performed at higher temperatures. The reason is two fold. Firstly, for higher rolling temperatures, TiAl alloys are more ductile. Consequently, larger reductions per rolling pass set can be employed resulting in more deformation, higher nucleation of recrystallized grains, and a finer grain size. Secondly, since the rolls are cold and remove heat rapidly from the sample, a higher starting temperature may be high enough that the specimen does not cool below the DBTT before the sample passes completely through the

rolls. This latter problem may have been the cause of the cracks which developed when rolled at 900 C. Rolling at temperatures above 900 C was impractical at the facility where rolling was performed, because it was felt that above 900 C the rolls would become damaged. There was no other means available for hot working; consequently, the hot rolling process was discontinued.

6. HOMOGENIZED HARDNESS

The homogenized hardness of each of the ternary alloys was determined in order to possibly correlate with mechanical properties or substitutional behavior of the solute. Figure 17 gives the hardness data for the ternary alloys with an effective ratio (a/o Ti) / (a/o Al), "Ti"/"Al", equal 1. The effective ratio is determined for each alloy by using the substitution behavior of the alloying addition, x. For Ag, Cr, and Ga, the substitution behavior assumed is for Al. For Mn the substitution behavior is assumed to be random. Zirconium is assumed to substitute for Ti. As an illustration the "Ti"/"Al" ratio for Mn equals Ti + 0.5 Mn / Al + 0.5 Mn. All of the hardness values reported are for single phase alloys. The typical standard deviation for the DPH measurements is +/- 20 DPH.

The stoichiometric binary alloy hardness is consistent with that given in literature, 173 DPH +/- 21. All alloying additions except Ag increase the hardness relative to the stoichiometric binary alloy. Mn and Zr appear to harden the binary alloy at a faster rate than Ag, Cr, and Ga. Figure 18 shows a plot of hardness and ductility versus Al content for binary TiAl alloys [5]. The alloy with the best ductility has an intermediate hardness value indicating no clear trend between hardness and ductility. When the hardness of each of the ternary alloys was replotted, assuming a different substitution behavior than the one assumed above, there was no clear trend indicating substitution behavior. The hardness data for the Ag alloy is consistent with that found in literature [27]. The sharp increase in hardness, from 171 DPH (+/- 17) to 228

DPH (+/- 11), for the 3 a/o Ag alloy probably is associated with the formation of an extremely fine precipitate, similar to the ones discussed in the above section dealing with the Ag ternary phase diagram. Backscattering results on this alloy showed that it was single phase; however, if this alloy were observed by CBED, it may possibly be two phase as was the case with the previously discussed Ag alloys. The trends for Mn and Zr are the same as those in the literature, that is these additions harden TiAl [37]. The hardness data for 2 a/o Ga is slightly lower than that found in literature [33]. Kad et al. report a value of 220 DPH for 2 a/o Ga alloy that this research shows to be 187 DPH (+/-18 DPH). The discrepancy may be attributed to a purity difference between the two alloys. Kad's samples were produced in the same arc melter; however, the alloy with a 187 DPH hardness was cast after the arc melter had been upgraded to produce a consistently higher vacuum. Impurities are known to greatly effect the mechanical properties of TiAl alloys and hence the hardness [5]. The hardness for the 5 a/o Ga is consistent with this research.

7. QUATERNARY COMPOSITIONS

One objective of this research was to expand the γ single phase field to lower Al contents by microalloying. This was an attempt to improve the single phase room temperature ductility. The quaternary compositions were chosen with this objective in mind and based on conclusions drown from the results of the ternary alloys. The ternary results consisted of analysis of all the ternary alloy fracture surfaces, observation for slip bands around the hardness indents, and determination of number of phases using optical and SEM techniques. The compositions were chosen such that the effective ratio of Ti to Al was unity.

Figures 19-24 show typical optical microstructures and fracture surfaces for the 50 a/o Al binary alloy and ternary alloys of Ag, Cr, Ga, Mn, and Zr . These are all single phase alloys. The optical micrographs of these alloys are very similar. The grains are all equiaxed and fairly

identical in size from one alloy to the next. They all show many large and small annealing twins. The fracture surfaces are a mixture of intergranular and transgranular fracture. The Ag alloy, figure 20, has the highest amount of intergranular fracture. This could be associated with grain boundary embrittlement due to the formation of a Ag-Al solid solution at the grain boundaries. Figure 25 shows the fracture surface for a higher Ag two phase alloy. A sheet of Ag-Al can be seen along the grain boundary. The Cr alloy, figure 21, has the largest amount of cleavage. The fracture surfaces for the binary, Mn, and Zr alloys' are very similar, all showing a mixed fracture surface. There was no significant difference in ductility of these samples based on the fractographs. However, figure 24 does show what may possibly be a grain which bent before fracturing. This may be a slight indication of ductility. Consequently, based on the fracture surfaces the only alloy which shows promise is the 1 a/o Zr alloy.

The vice bend test was a crude estimate of ductility of the ternary alloys. From this test, the only obvious conclusion was that the Ag alloys are more brittle than any of the other alloys. They required little effort to fracture in bending. Consequently, none of the quaternary compositions had Ag as an addition. These alloys were also easily crushed in the vice and showed no signs of compressive ductility. All other ternary alloys showed signs of compressive ductility as evidenced by slip bands around the compression indents produced by the vice. Polished surfaces of both the Cr and Zr ternary alloys were compressed in a vice and the surface reexamined. The surface showed extensive slip bands suggesting appreciable compressive ductility.

The Mn, Cr and Zr ternary alloys all showed slip bands around the majority of the hardness indentations. Since hardness indentations produce a complex tension and compression force, slip bands around these indents may be a sign of tensile ductility. Almost all of the indents for the Cr alloys showed profuse slip bands. Based upon this observation, Cr alloys show the most promise for room temperature ductility. To test this hypothesis several quaternary alloys of Cr

and Ag were drop cast and the hardness indents observed. In every case, the DPH indents showed slip bands. This was an improvement in ductility since for the Ag ternary alloys very few indents showed slip bands. In addition, these quaternary alloys did not shatter when placed in the vice and bent. This is an improvement compared to the Ag ternary compositions, which shattered when clamped in a vice.

Based on the above observations, Cr, Mn, and Zr appeared to show the most promise for quaternary compositions. Therefore, quaternaries alloys of Cr/Mn, Cr/Zr, and Mn/Zr were drop cast. Published work indicates that ternary alloys of Mn and Ga show significant tensile ductility. A Ga/Mn quaternary was made to see if there was some synergistic effect of Ga and Mn on the tensile ductility. For ternary Cr alloys, additions higher than 1 a/o caused precipitation of $\alpha 2$. Therefore, all Cr quaternary alloys had 1 a/o Cr as a base. Since the Ti-50/Al-49/Zr-1 alloy showed what may have been a bent grain upon vice bending, this composition was used as a base for the Zr quaternary compositions.

The compositions of the quaternary alloys were chosen such that the effective ratio of Ti to Al was unity. A minimum amount of alloying additions were used in order to preserve the $L1_0$ single phase structure. The stoichiometric binary has the smallest lattice parameter ratio and the highest ductility of the single phase binary alloys [5]. This may be associated with the minimum in the lattice parameter ratio. Consequently, the effective ratio for the quaternary alloys was maintained at unity in an attempt to minimize the lattice parameter ratio and possibly improve the ductility. The nominal compositions for these alloys which were zone processed, homogenized, and four point bend tested were:

Ti-48.5/Al-48.5/Cr-1/Mn-2,

Ti-48.5/Al-49/Cr-1/Zr-1,

Ti-48/Al-48/Mn-2/Zr-2,

Ti-48/Al-48/Ga-2/Mn-2.

8. BEND TEST AND MICROSTRUCTURAL RESULTS

The above compositions along with two binary alloys, used for comparison purposes, were zone processed, homogenized and tested in four point bending. Three of these alloys were also subjected to K1 fracture toughness testing. These test results are given in table 9. This table shows for the homogenized samples the fracture stress, percentage strain at fracture, the fracture stress determined for a notched sample, the stress intensity factor, the average two phase colony or grain size on the tensile surface, and the percentage of α_2 present. The percent α_2 present is a rough estimate of the volume fraction determined by using a SEM histogram technique. It is used solely to illustrate the small amount of second phase present. All values, except for the percent α_2 present, have standard deviations given in parentheses.

Comparing the fracture stress and the percent fracture strain, the alloy TiAl+Cr+Mn shows the most promise. This alloy shows the highest fracture stress of 468 (+/- 22) MPa, when compared to either the ternary Cr alloy or either of the binary alloys. Literature indicates that the 48 a/o Al binary alloy has the highest ductility and strength [5]. However, this is very dependent upon microstructure and the amount of α_2 present; consequently, the best combination of strength and ductlity may not have been achieved. The percent fracture strains were not substantially different. TiAl+Cr+Mn had the highest value. However, when considering the standard deviation, this value was not substantially different from either of the binary alloys, the Cr ternary alloy, or the Ga/Mn quaternary alloy. Consequently, from a ductility stand point, there does not appear to be any overall improvement.

The fracture stress for the K1 test is higher for the Cr/Zr quaternary alloy in comparison to that of the binary alloy or the TiAl+Mn+Zr alloy. The Mn/Zr alloy precusor ingot was

accidentally contaminated with copper. Based upon SEM EDX and backscattering experiments, it was determined that all of the copper, approximately 4 a/o, resided in a third phase; no copper was seen in either $\alpha 2$ or γ. This suggests that there is essentially a null solubility of Cu in Ti_3Al and TiAl. For this alloy, the amount of α_2 present was approximatley 4 volume percent. This phase precipitated at the grain boundaries. The large standard deviation on the fracture stress may possibly suggest that Cu embrittles and weakens the grain boundaries, since this alloy has a comparable average grain size and amount of second phase to that of the Cr/Zr alloy. This latter alloy has a lower K1 fracture stress and a third of the standard deviation. The size of the individual test specimens were not substantially different between the Mn/Zr and Cr/Zr quaternary alloys. Because of the small volume percent present of this Cu phase, some of these samples may have had these contaminated boundaries oriented appropriately for premature failure to occur. The Mn/Zr alloy also had the largest variation in K1 value. Both the large variation in K1 fracture stress and the large variation in K1 suggest that this data should not be used for mechanical properties comparison purposes. Neglecting the data for TiAl+Mn+Zr, the fracture toughness of the Mn/Zr alloy is slightly improved relative to that of TiAl. Both the K1 fracture stress and the K1 value are also slightly higher than that of the binary alloy. This improvement may be associated with the quaternary alloy having a smaller grain size, the quaternary alloy's second phase being present only at the boundaries, or the strengthening caused by alloying.

The average grain size does not vary much among the quaternary alloys. However, the colony size is slightly larger for the Ti-50/Al-50 alloy and substantially larger for the Ti-52/Al-48 alloy. The 48 a/o Al binary alloy appears to have slightly more second phase than any of the other alloys. However, this is a very crude estimate of volume percent and the phases are extremely fine; consequently, it is difficult to be certain of the exact amounts. The α_2 that forms in the quaternary alloys does so only at the grain boundaries. The exception to this is

for the Cr/Mn alloy. In this alloy, α_2 is present at the grain boundaries and in the form of a lamellar structure inside the grains. The binary alloys are completely lamellar with a small amount of γ present at the colony boundaries.

In order to fully understand the mechanical properties of the alloys given in table 9, the microstructure and fracture surfaces must be examined. In the following sections, the arc melted and homogenized microstructure, the as zone processed structure, the zone processed and homogenized structure, and the fracture surfaces are compared.

(a) THE Ti-50/Al-50 ALLOY

Figure 26 shows the homogenized arc melted structure for the 50 a/o Al binary alloy. This microstructure consists of large equaxed grains with large and small annealing twins. This alloy was determined to be single phase by SEM backscattering. The homogenized composition as derived from SEM EDX was Ti-50.5/Al-49.5.

Figure 27 shows a low magnification photograph of the zone processed ingot. In figure 27a the external surface of the processed alloy illustrates what appears to be large grains on the surface. These are actually large packets of a lamellar structure of $\alpha 2$ and γ. 27 b shows the transverse and longitudinal cuts. The longitudinal cut shows a very large packet size with an extremely fine lamellar structure.

This zone processed alloy was two phase even after homogenization at 1100 C for 100 hours. SEM EDX performed on two different areas of this homogenized alloy, revealed that the γ phase composition was 49.4 (+/-0.1)and 50.2 (+/-0.2) a/o Al. The α_2 phase was 36.1 (+/-0.2) a/o Al and 38.6 (+/-0.4) a/o Al. Within the experimental accuracy of EDX and due to the proximity of this alloy's Al content with that of the minimum content for the single phase γ field, 48 a/o Al, the Al content of this alloy may have been insufficient enough to

enter the single phase γ field. Both the zone processed alloy and the arc melted alloy have compositions which are extremely close to the $\alpha 2 + \gamma / \gamma$ boundary. If the arc melted alloy was actually higher in Al than 48 a/o and the zone processed alloy was slightly lower than 48 a/o Al, the arc melted alloy would be single phase after homogenization and the zone processed alloy would be two phase.

The two phase structure resulting from zone processing is extremely fine as evidenced by figure 28. This shows a backscattered image of the homogenized zone melted alloy. The fine white precipitate is α_2. The fineness of this phase makes it difficult to see in the optical micrographs, figures 28b and 28c. In 28b, the microstructure is almost entirely lamellar with α_2 and γ showing an orientation relationship. In the higher magnification micrograph, 28c, a small amount of blocky proeutectoid single phase γ, is seen at the prior α grain boundaries (see arrows). The grain boundary γ has an orientation relationship with both neighboring grains suggesting that it formed prior to the lamellar structure.

Jones et al. published schematic CCT diagrams for two phase TiAl binary alloys [21]. Figure 3 shows the CCT diagram for a 48 a/o Al alloy. From this diagram, the slow cooling process of zone refining should produce a lamellar structure of γ and α_2 with some proeutectoid γ being present. They claim that γ nucleates preferentially at stacking faults in α and that heterogeneous grain boundary nucleation is not a major nucleation mode. Additionally, they report that the eutectoid reaction does not occur. Instead a lamellar structure results with phases not given by the eutectoid reaction. They contend that this structure results because of the orientation relationship which exists between γ, α, and α_2. Figures 28b and 28c show that the microstructure is partially consistent with the CCT diagram. That is, proeutectoid γ and a lamellar structure form. The proeutectoid γ appears to preferentially nucleate at the prior α grain boundaries. Theoretically, a large number of stacking faults should exist at the prior α grain boundaries because of lattice mismatch. However, whether or not γ is nucleating

at boundary stacking faults or just at the grain boundary is unclear. In addition, knowing whether or not the lamellar structure resulted from the eutectoid reaction or not is difficult to determine. The reason that the eutectoid composition, 39 a/o Al, is in close proximity to the composition of α_2 at the eutectoid, 37 a/o Al. From the $\alpha 2$ EDX values, 38.6(+/−0.4) and 36.1 a/o(+/−0.2) Al, and the proximity of the eutectoid to the α_2 composition at the eutectoid temperature, it is difficult to conclude whether or not the eutectoid reaction has occurred.

Figure 29 shows the homogenized microstructure near the fracture surface of one of the bend specimens. The surface of this sample was polished and etched after testing. Comparing the structure of this sample to that of the zone processed structure (figure 28b), it is seen that the γ plates have thickened. According to the literature, coarsening of TiAl two phase alloys occurs by thickening of the α_2 and γ plates [21], the driving force being the minimization of surface energy. Spheroidization is not likely to be observed, because the orientation relationship must be maintained. This may explain why the γ plates thickened instead of spheroidized. The amounts of phases present in the homogenized zoned processed alloy appear to be the same as those in the as-zone processed alloy. Whether or not this is true is difficult to determine. Consequently, the equilibrium structure may or may not have been achieved upon zone processing.

Figure 29 also shows how cracks propagate through this structure as a result of the bending force. The cracks appear mainly to follow the lamellar boundaries. However, transboundary crack propagation does occur. This may be associated with the orientation of the lamellae. Figure 29a shows that as the lamellae change orientation so does the crack direction. This is consistent with literature information which indicates lamellar orientation significantly affects mechanical properties[24].

Figure 30 shows the fracture surface of this alloy. From this figure, there does not appear to be significant changes in the fracture nature from the tension to the compression sides. Figure 30a shows that this alloy failed mainly by interlamellar separation with some signs of cleavage across lamellar colonies. Under higher magnification, the tension side of the fracture shows some signs of ductility. Figure 30b shows what may be slip traces and very narrow deformation twins. According to literature, the binary alloys do not usually deform by twinning below 600 C [14,15]. However, thin deformation twins have been reported to form in some ternary alloys, (e.g. Cr) [30]. In any case, no TEM diffraction patterns were derived for this alloy; consequently, a conclusion can not be drawn. Figure 30b shows a smooth fracture surface which lacks evidence of river patterns caused by cleavage. This surface may have been an interlamellar boundary, prior to fracture. At higher magnification the photomicrograph, figure 30c, shows sets of parallel lines which may be slip traces and/or deformation twins. Figure 30d shows what appears to be a lamellae separating from the interlamellar boundary. This is consistent with the crack propagation seen in the optical micrographs, figure 29. Figure 30e shows an interesting side note. In this figure, the growth facets can be seen in a casting pore.

(b) THE Ti-52/Al-48 ALLOY

Figure 31 shows a macrograph of the zone processed ingot. This alloy is similar to the 50 a/o Al alloy. The structure consists of large packets of the fine lamellar structure. Figure 31a shows the external structure of the zone processed ingot. Figure 31b shows the longitudinal cut and a transverse cut. Unfortunately, the transverse cut was taken in the last zone to freeze. This structure results from the impurity build up occurring ahead of the freezing solid/liquid interface as a result of zone refining. Therefore, this structure is not indicative of the rest of the processed ingot, since its composition is different and solidification was probably non-steady state.

Since the nominal composition of this alloy, 48 a/o Al, was slightly lower than that of the 50 a/o Al, it is expected that more α_2 should be present in the 48 a/o Al alloy. According to the SEM histogram technique, this is true. Figure 32a shows the microstructure of the directionally processed alloy. Like the 50 a/o Al alloy, large prior α_2 grains composed now of a lamellar structure of α_2 and γ are seen. Figure 32b shows blocky γ forming at the prior α grain boundaries (see arrows). Again, this phase appears to have an orientation relationship with both neighboring grains indicating that it formed prior to the lamellar structure.

Figure 33 shows the homogenized zone processed alloy. These micrographs were taken from the tension surface of a bend specimen near the fracture edge. The surface of this sample was polished and etched after testing; consequently, the structure is indicative of this preparation. This structure is not substantially different from that of the as-zoned alloy. The lamellar plates do not appear to have thickened substantially upon homogenization. Figure 33a shows a backscattered image of this alloy. Fine α_2, white phase, is seen, the fineness of which makes its detection in the optical micrographs, figures 33b and 33c, difficult. SEM EDX results indicate that the γ and α_2 phases have compositions of Ti-52.0/Al-48.0 (+/-0.2) and Ti-61.3/Al- 38.7 (+/- 0.6), respectively. Again, the composition of α_2 is too close to the composition of the eutectoid and the maximum Al content of α_2 at the eutectoid temperature to determine whether or not the eutectoid reaction occurred. The crack propagation shows that there appears to be a preference for following the interlamellar boundary. However, transboundary crack propagation does occur. This is seen in figure 33b and 33c.

Figure 34a show the overall fracture surface of this homogenized alloy. The fracture mechanism appears to be mainly lamellar separation with some cleavage across lamellar colonies. The compressive side appears to be all lamellar cleavage. The tension surface, figure 34b, shows several lamellae which have been bent (see arrows), but still remain attached to

the lamellar boundary. This seems consistent with the optical micrographs, figure 33. This lamellar tearing is evidence of ductility.

(c) THE Ti-49.5/Al-49.5/Cr-1 ALLOY

Figure 35 shows a macro of the zone processed alloy. Figure 35a shows the external surface of the zoned ingot. This surface shows what appears to be a finer packet size in comparison to the binary alloys. From the transverse and longitudinal cuts, shown in figure 35b, this small packet size is only a surface phenomena. The colony size is equivalent to that of the zone processed binary alloys. However, the grain boundary γ is coarser in this alloy. It is already visible in this macrograph (see arrow)

Figure 35c shows that the structure is mostly fine lamellae. A small portion of this structure consists of coarse and blocky grain boundary γ, figure 35d. This phase is continuous in neighboring grains indicating that it formed prior to the lamellar structure.

Figure 36 shows the homogenized zone processed microstructure. This structure is taken from a bend specimen near the fracture surface. The surface of this sample was polished and etched after testing. This sample's structure appears to be single phase with large equaxed grains, figure 36a. Large annealing twins are apparent. Needle shaped structures can also be seen. These structures are assumed to be deformation twins. Figure 36b shows these deformation twins within an annealing twin. When this alloy is observed in backscattering, figure 36c, a small amount of second phase is seen to be present at the grain boundaries. This phase is an α_2 based phase with a composition given by EDX of Ti-62.2 (+/-0.3)/Al-36.8 (+/- 0.3)/Cr-1.0 (+/-0.1). The matrix, γ, has a composition of Ti-50.5 (+/-0.2)/Al-48.5 (+/-0.2)/Cr-1.0 (+/-0.1). Figure 36a shows the fracture edge on the tension surface of a bend bar. This shows that cleavage is the predominate mode of fracture, because there are no signs of grain boundary separation. The crack propagation does change direction from one

grain to another. This is most likely associated with changes in favored cleavage planes from grain to grain.

Figure 37 shows the fracture surface of the zoned processed homogenized Cr ternary alloy. Figure 37a shows both the tension and compression edges. The cleavage fracture mode appears to be the same from one side to the next. Upon higher magnification, figure 37b, only signs of cleavage were observed. The fracture surface is consistent with the optical surface 36a. It was observed that from one grain to the next the orientation of fracture edge changed due to changes in favored cleavage planes from grain to grain. This is consistent with the cleavage facet size being equal to the grain size, as seen in 37a. No obvious signs of intergranular fracture were observed. This suggests that the grain boundary second phase did not weaken the boundary and may have even strengthen it. In addition, there were no obvious signs of ductility.

(d) THE Ti-48.5/Al-48.5/Cr-1/Mn-2 ALLOY

Figure 38 shows a macrograph of the zone processed Cr/Mn quaternary alloy. Figure 38a shows the surface of the zone processed ingot, which has a much smaller colony size in comparison to the binary alloys and the Cr ternary alloy. The small colony size is not only a surface structure, but is distributed throughout the ingot, as seen in 38b.

Figure 39 shows the as-zoned structure. This figure shows coarse proeutectoid γ, much coarser than that of the binary alloys or the Cr alloy and is much more prevalent. The lamellar structure also appears to be coarser in comparison. The volume fraction of the lamellar structure appears to have been reduced in comparison to the above alloys.

Figure 40 shows the microstructure for the homogenized zone processed alloy. These micrographs are taken in the proximity of the fracture edge from one of the bend specimens.

The surface of this sample was polished and etched after testing; consequently, the structure is indicative of this preparation. The microstructure in figures 40a and 40b show large equaxed grains with annealing twins. Figure 40b shows deformation twins inside an annealing twin. This alloy appears to be single phase, however, the backscatter mode reveals that a small amount of second phase exists at the grain boundaries, figure 40c. This micrograph is taken on a bend specimen after testing. The needle shaped structures inside the grains are assumed to be deformation twins. These are also apparent in 40b. What appears to be lamellar structure in figure 40a is actually an etching artifact as determined from backscatter examination on a polished unetched bend specimen. The second phase, α_2, was only observed at the grain boundaries. The as-zoned alloy was predominately lamellar. This indicates that, for this alloy, the equilibrium structures were not achieved upon zone processing. The composition derived from EDX was Ti-48.5 (+/-0.4)/Al-49.9 (+/-0.2)/Cr-.9 (+/-0.1)/Mn-1.7 (+/-0.2) for γ and Ti-58.9 (+/-0.1)/Al-38.2 (+/-0.2)/Cr-1.2 (+/-0.1)/Mn-1.7 (+/-0.1) for $\alpha 2$.

Figure 40b shows the fracture edge. The fracture mode appears to be mainly cleavage. There are no signs of intergranular fracture.

Figure 41 shows the fracture surface of a bend bar from this homogenized alloy. Figure 41a shows both the tension and compression sides of the fracture surface. The cleavage nature of fracture appears to be uniform from one side to the next. The cleavage facet size appears to be the same as the grain size. There are a few regions of the fracture surface which do show evidence of intergranular fracture, figure 41b. However, the predominate fracture mode is cleavage. There are no obvious signs of ductility on the fracture surface. The fracture surface of this alloy resembles that of the Cr alloy.

(e) THE Ti-48.5/Al-49.5/Cr-1/Zr-1 ALLOY

Figure 42 shows a macro of the zone processed ingot. These figures show an extremely fine

colony size. The structure appears to be uniform across the entire length of the ingot. The optical micrograph, figure 43, shows that more proeutectoid γ has formed in comparison to all of the above alloys. The lamellar structure has also become coarser in comparison.

Figure 44 shows the homogenized zone melted bend bar in the vicinity of the fracture edge. The surface of this sample was polished and etched after testing. This alloy shows large grains, as seen in figure 44a and 44b. Figure 44b shows a small amount of what is assumed to be deformation twins, the amount of which is small in comparison to the Cr/Mn quaternary alloy. This alloy is predominately single phase. However, a few grains boundaries have an α_2 based precipitate as seen in figure 44c, which is a backscattered image of the polished unetched bend specimen. From EDX, the γ composition was Ti-49.2 (+/-0.1)/Al-48.7 (+/-0.2)/Cr-1.0(+/-0.1)/Zr-1.2(+/-0.2). The second phase was too small to accurately determine the composition using EDX. There are no signs of a lamellar structure as seen in the as-zoned structure. Because of the difference in structure between the homogenized and as-zoned alloy, the equilibrium structure does not appear to have been achieved upon zone processing. By observing the fracture edge, figure 44a and 44b, it is seen that the predominate fracture mode is cleavage. There are no obvious signs of intergranular fracture. A small amount of deformation twins are seen.

Figure 45 shows the fracture surface of this bend bar. 45a shows both the tension and compression sides. There is no apparent difference between the two edges. The predominate fracture mode is cleavage in agreement with the optical observations. The cleavage facet size is consistent with the grain size. There are no signs of intergranular fracture indicating that the amount of second phase is probably too small to have a significant impact on the fracture. Figure 45b and 45c show the same region, except 45c is a higher magnification micrograph. This latter figure showed what may be deformation twins or slip traces. This was the only sign of ductility seen. This fracture surface is very similar to that of the Cr and the

Cr/Mn alloys. All of these alloys failed predominately by cleavage with the cleavage facet size corresponding to the grain size. The fracture surface of the Cr/Zr quaternary alloy did not show signs of intergranular failure as did the Cr/Mn alloy. The fracture surfaces of the Cr and the Cr/Mn alloys did not show signs of deformation twins or slip traces like the Cr/Zr alloy did. This suggests that this alloy has a higher ductility. However, as seen in table 9, the opposite is true. The Cr/Zr quaternary alloy showed the lowest percent strain of the Cr based alloys.

(f) THE Ti-48/Al-48/Ga-2/Mn-2 ALLOY

Figure 46 shows the longitudinal and transverse section of the as-zoned Ga/Mn alloy. From this figure, it is seen that the structure is uniform across the entire ingot. The lamellar colony size is hard to distinguish in these images. Figure 47 shows the optical micrograph of this ingot. Large irregular shaped γ grains are observed. This alloy has the least amount of the lamellar structure, however, there are still a few lamellar colonies remaining.

Figure 48a shows the homogenized microstructure present near the fracture edge of a bend specimen. The surface of this sample was polished and etched after testing. The microstructure shown in this figure consists of large elongated grains similar to those found in the as-zoned structure. This indicates that the equilibrium structure was probably achieved upon zone refining. This alloy is predominately single phase as determined by backscattering. However, a slight amount of second phase, based upon α_2, is seen to form at some grain boundaries, figure 48b. The EDX composition of this phase is Ti-58.3 (+/-0.3)/Al-36.0 (+/-0.3)/Ga-1.3 (+/-0.1)/Mn-4.4 (+/-0.2). The matrix, γ, is determined to be Ti-48.6 (+/-0.7)/Al-47.4 (+/-0.9)/Ga-2.3 (+/-0.1)/Mn-1.8 (+/-0.2). Figure 48a is distinctly different from either the Ga and Mn ternary alloys, figure 22a and 23a, respectively. The ternary alloys showed large equaxed grains with large annealing twins. These structures were

not seen in the Ga/Mn quaternary alloy, however, some narrow annealing twins are present, 48a. The difference between the ternary and the quaternary alloys is probably due to the synergistic effect between Ga and Mn, since the equilibrium structure appears to have been achieved upon zone processing. Ternary additions of both Ga and Mn decrease the C/A ratio of the binary alloy. Whether this trend continues for the quaternary must still be determined.

Figures 48a and 48c show the fracture edge of a bend specimen. From 48c it is seen that the predominate mode of failure is cleavage. There was no sign of intergranular fracture or deformation twinning. However, whether or not the latter is seen depends upon the orientation of the grains.

Figure 49 shows the fracture surface of this bend specimen. Figure 49a shows both the compression and tension sides of the fracture surface. The fracture nature from one side to the other does not appear to change much. The fracture surface can be characterized as having failed by cleavage with a few areas of intergranular failure, figure 49b. The cleavage facet size is difficult to discern. Figure 48c shows a crack propagating through two grains without much change in direction. This indicates that the cleavage planes of these two grains are the same or that Ga/Mn alloy has many cleavage planes with the same strength. This is the only alloy tested that did not show some correlation between grain size and cleavage facet size. Based upon this conclusion, this alloy would be considered to be the least ductile. From table 9 this is not obvious based upon the percent strain measurements. There were no obvious signs of ductility.

(g) THE Ti-48/Al-48/Mn-2/Zr-2 ALLOY

Figure 50 shows a macrograph of the as-zone Mn/Zr alloy. Figure 50a shows the external surface of this ingot. This surface has a modeled texture, which was not seen on any other alloys. The longitudinal and transverse sections illustrate that the structure is uniform

throughout the ingot, figure 50b. Figure 50c shows that the structure consists of a lamellar structure with a fine packet size and proeutectoid γ. The proeutectoid γ is much coarser than that of the binary alloys.

Figure 51 shows the homogenized microstructure present near the fracture edge of a bend specimen. The surface of this sample was polished and etched after testing. Figure 51a shows large equaxed grains with some annealing twins. There is no lamellar structure present as evidenced in the backscatter mode. However, the precussor ingot of this alloy was accidentally contaminated with copper and two additional phases are seen to precipitate in the γ matrix, figure 51b. According to EDX, the white phase is Ti-23/Al-43/Mn-16/Zr-14/Cu-4 . The light gray phase, α_2, has a composition of Ti-57/Al-38/Mn-3/Zr-1. The matrix, γ, has a composition of Ti-43.9 (+/-0.3)/Al-50.4 (+/-0.3)/Mn-1.9 (+/- 0.1)/Zr-3.6(+/-0.1). From these results, both γ and α_2 appear to exhibit a null solubility of Cu.

Both figure 51a and 51c show the fracture edge of this bend specimen. From these figures it is seen that fracture occurred by cleavage. There were no signs of either intergranular fracture or deformation twinning.

Figure 52 shows the fracture surface of this bend specimen. Figure 52a shows both the tension and compression sides of the fracture surface. The fracture surface appears to consist mainly of cleavage, which is consistent with the optical view of the fracture edge. The cleavage facet size is equivalent to the grain size, figure 52a. Figure 52b shows one area which may have a small amount of intergranular fracture. There were no obvious signs of ductility. The lack of a large amount of intergranular fracture appears to indicate that either the amount of second and third phase was too small to cause embrittlement or these phases did not effect the boundary.

9. EVIDENCE OF DUCTILITY

Based upon the appearance of the fracture surfaces, the only alloys which showed significant signs of ductility were the alloys with a lamellar structure, the homogenized binary alloys. Based upon the fracture surfaces only, it would be concluded that the other alloys had no ductility in comparison. This is not the case as represented by the percent strain at fracture and the plots of stress verses percent strain, figures 53-59. These data show that the curves deviate from linearity, that is plastic flow has occurred. The amount of plasticity was determined for each bend specimen by drawing a line on these plots through the fracture point (fracture stress, fracture strain) to the abscissa with a slope equal to the slope of the elastic region of the loading curves. The intersection of this line and the percent strain axis yields the amount of percent plastic strain at fracture. Table 10 gives the average and standard deviation values of plastic strain for each of these alloys as determined by this method.

The Mn/Zr quaternary alloy shows the least amount of plastic strain, figure 58 and table 10. The synergistic effect of Mn/Zr apparently decreases the cleavage strength of this alloy. Since no intergranular fracture was seen, the decrease is not associated with embrittlement of the grain boundaries due to Cu, but must be associated with the cleavage strength. Since the matrix, γ, contains no Cu the change in cleavage strength must be associated with Mn and Zr. The decrease in cleavage strength is consistent with the lack of correlation between cleavage facet size and grain size, described above. The other alloys show no substantial difference in plasticity.

10. COMPARISON OF CURRENT RESULTS TO THOSE GIVEN IN LITERATURE

A comparison of the data from this work to the four point bend data in the literature can only be performed on three alloys: the binary alloys, 48 a/o Al and 50 a/o Al, and the Cr ternary alloy. This is due to the lack of literature bend data for the compositions of the other alloys.

Table 11 gives the literature values for these alloys from the work by Kawabata et al. [4]. The fracture stresses are similar to those in table 11. The major discrepancy between the literature results and the results of this research is in the fracture strain measurements. This is most likely attributed to Kawabata's specimens having a testing dimension of 1 mm compared to 4 mm for this research. The smaller dimension offers less constraint, and hence, will behave in a less brittle fashion. No indication was given by Kawabata et al. of how the fracture strains were determined. In addition, the grain size of these alloys was not given. These latter effects may affect the comparison of the test results. The strain rate for the data given in table 11 was $8x10^{-5}$ 1/s. The strain rate for this research was $5x10^{-3}$ 1/s. Kawabata et al. are quoting a strain rate that is two orders of magnitude lower than used for the data in this research. This may contribute to the differences in the percent strain measurements. This should not have a major effect, since literature indicates that TiAl is not strain rate sensitive at room temperature [13,1].

The fracture toughness for the binary alloys are reported to be from 10 to 16 MPa$\sqrt{m}$ [5]. This is similar to the values given by this research.

IV. SUMMARY OF RESULTS AND CONCLUSIONS

The objective of this research was to investigate the effects of ternary and quaternary additions in extending the single phase γ field to lower Al contents. This was examined in order to investigate whether or not single phase γ alloys would improve in room temperature ductility if the Al content could be lowered. Within the experimental accuracy of EDX, it can be concluded that ternary Mn additions and possibly Ga additions slightly shift the γ single phase boundary to lower Al contents. Zr and Cr additions shift this boundary toward higher Al contents.

The zone processing used in this research produced alloys which are of higher purity than related work reported in the literature. Based upon a heating study for a two phase binary alloy, diffusion appears to be too sluggish for phase transformations to occur at temperatures below the eutectoid temperature. Hot working experiments showed that the grain size could be reduced. However, the hot working should be performed at temperatures above 900C in order to prevent cracking of the specimens. There appears to be no correlation between the homogenized hardness and the strength or ductility for TiAl alloys.

The ternary and quaternary compositions of these alloys show no obvious improvement in ductility. The Cr/Mn alloy has the highest strength and the highest ductility of the alloys tested. The other additions (Ag, Cr and Zr) show no significant improvement in ductility relative to the binary, 48 a/o Al, alloy which has the best reported ductility. The ductility measurements reported in this research are substantially lower than those reported in the literature. This is attributed to a larger test specimen thickness for the alloys in this research. The larger thickness offers more constraint resulting in more brittle behavior. All quaternary samples showed some signs of plasticity as indicated by the deviation from linearity of the stress versus strain curves. A few samples' fracture surfaces also showed signs of what may

be slip traces or deformation twins, which is also evidence of some plastic ductility.

As a result of this research, it was determined that Ag, Cu, and Cr are essentially insoluble in TiAl. Cu was also determined to be insoluble in Ti_3Al. Ag and Cu additions were found to embrittle TiAl based alloys.

The site substitution behavior of these elements was also determined. Zr was determined to substitute for Ti in TiAl, Cr for Al in TiAl, and Mn for both Ti and Al.

The fracture toughnesses were determined for a Cr/Zr and a Mn/Zr alloy. These values were compared to those determined for the 50 a/o Al binary alloy. Based upon the results of this research, the fracture toughnesses of the quaternary alloys were not substantially better than that of the binary alloy.

All of the quaternary alloys tested were slightly two phase. As a consequence, the question of whether any improvement in ductility is due a decrease in the Al content of single phase γ can not be conclusively answered even though the volume fraction of second phase was small. In addition, literature reports that grain size plays an important role in ductility. Since grain size was not controlled in this research, this may have some influence on the ductility of these alloys . Future work should investigate the effect of grain size. Also, alloys of slightly higher Al and/or lower alloying additions should be produced in order to more closely examine the lowest Al single phase γ alloys.

REFERENCES

REFERENCES

1. Kim Y.; JOM, July, 24-30, (1989).

2. Vujic D., Li Z., and Whang S.; Met Trans A, 19A, 2445-2455, (1988).

3. Huang S. and Hall E.; Met Trans. A, 22A, 427-438, (1991).

4. Kawabata T., Tamura T., and Izumi O.; Mat. Res. Soc. Symp. Proc., 133, 329-334, (1989).

5. Kim Y. and Dimiduk D.; JOM, August, 40-47, (1991).

6. Kawabata T., Tadano M., and Izumi O.; Scripta Met, 22, 1725-1730, (1988).

7. Elliot R. and Rostoker W.; Acta Met, 2, 884-885, (1954).

8. Lipsitt H., Shechtman D., and Schafrik R.; Met Trans., 6a, 1991-1996, (1975).

9. Dimiduk D., Miracle D., and Ward C.; Intermetallic Materials for Aerospace Systems, 367-375, (1992).

10. Suryanarayana C., Froes F., and Rowe R.; Int. Materials Reviews, 36, 3, 85-123, (1991)

11. Oliver B., Oliver W., and Huang B.; Scripta Met, 22,1405-1408, (1988).

12. Shechtman D., Blackburn M., and Lipsitt; Met Trans, 5, 1373-1381, (1974).

13. Lipsitt H., Shechtman D., and Schafrik R.; Met Trans A, 6A, 1991-1996, (1975).

14. Kawabata T., Kanai T., Izumi O.; Acta Metall, 33 (7), 1355-1366, (1985).

15. Kawabata T., Takezono Y., Kanai T., Izumi O.; Acta Metall, 36 (4), 963-975, (1988).

16. Hug G., Loiseau A., Veyssiere P.; Phil Mag A , 57 (3), 499-523, (1988).

17. Huang Y. and Whang S.; Scripta Met, 24, 139-144, (1990).

18. Huang S. and Siemers P.; Met Trans A, 20A, 1899-1906,(1989).

19. Oliver B. and Kad B.; J less Common Metals, 168, 81-90, (1991).

20. Mishurda J. and Perepezko J.; Mat. Res. Soc. Symp. Proc., (1990).

21. Jones S. and Kaufman M.; in press Acta. Met

22. Dogan B., Wagner R., and Schwalbe K.; private communication.

23. Umakoshi Y., Nakano T., and Yamne T.; J. Inst. Met Symp. Proc., (1991).

24.Yamaguchi M.; Matls. Sci. Tech., 8, 297-307, (1992).

25. Chan K.; JOM, May, 30-38, (1992).

26. Pettifor D.; N. Sci., 29, 48-53, (1986).

27. Tsujimoto T., Hasimoto K., Nobuki M., Suga H.; Trans Japan Inst Metals, 27 (5), 341-350, (1986).

28. Nandy T., Banerjee D. and Gogia A.; Scripta Met, 24, 2019-2022, (1990).

29. Hashimoto K., Doi H., and Tsujimoto T.; Trans Japan Inst Metals; 27 (2), 94-101, (1986).

30. Wunderlick W., Kremser T., Frommeyer G.; Z. Metallkde, 81 (11), 802-808, (1990).

31. Kasahara K., Hashimoto K., Doi H., and Tsujimoto T.; J. Japan Inst Metals, 54 (8), 948-954, (1990).

32. Ren Y., Chen G., and Oliver B.; Scripta Met, 25, 249-254, (1991).

33. Kad B. and Oliver B.; Mat. Res. Soc. Symp. Proc., 133, 237-242, (1989).

34. Huang S., Michael E., Gigloitti F.; U. S. Patent # 4902474.

35. Hashimoto K., Doi H., Kasahara K., Tsujimoto T., and Suzuli T.; J Japan Inst Metals, 52 (8), 816-825, (1988).

36. Babu v. and Seehra M.; J Mater Res, 6 (2), 339-342, (1991).

37. Tsujimoto T. and Hashimoto K.; Mat Res Soc Symp Proc, 133, 391-396, (1989).

38. Hanamura T., Uemori R., and Tanino M; J Mater Res, 3 (4), 656-664.

39. Hashimoto K., Doi H., Kasahara K., Nakano O., Tsujimoto T., and Suzuki T.; J. Japan Inst. Metals, 52 (11), 1159-1166, (1988).

40. Xiang'yan K., Xuanhui Q., and Baiyun H.; Rare Metals, 10 (1), 38-42, (1991).

41. Liu C.; Science of Advanced Mater., 423-459.

42. Hashimoto K., Doi H., Kasahara K., Tsujimoto T., and Suzuki T.; Japan Inter SAMPE Symp, 157-162,(1989).

43. Hanamura T. and Tanino M.; J Mater Sci Letters, 8, 24-28, (1989).

44. Reviere R. , Oliver B., and Bruns D.; Mat. and Mauf. Proc., 4 (10), 103-131, (1989).

45. Measurements Group Inc.; Student Manual For Strain Gage Technology, Bulletin 309c

(1991).

46. Kad B.; P.h. D. Dissertation, University of Tennessee, (1990).

47. Hashimoto K., Doi H., and Tsujimoto T.; J. Inst. Metals, 27 (2), 94-101, (1986).

48. Ren Y., Chen G., Oliver B.; Scripta Met, 25, 249-254, (1991).

49. Doi H., Hashimoto K., Kasahara K., and Tsujimoto T.; J. Japan Inst. Metals, 53 (11), 1089-1097, (1989).

50. Babu V. and Seehra M.; J. Mater. Res., 6 (2), 339-342, (1991).

51. Mohandas E. and Beaven P.; Scripta Met, 25, 2023-2027, (1991).

52. Rossouw C., Turner P., White T., and O'Connor A.; Phil. Mag. Let, 60 (5), 225-232, (1989).

53. Turner P., White T., O'Connor J., and Rossouw C.; J. Microscopy, 162 (2), 369-378, (1991).

54. Cliff G. and Lorimer G.; J. Microscopy,103 (2), 203-207, (1975).

55. Spence J. and Tafto J.; J. Microscropy, 130 (2), 147-154, (1982).

56. Mehrer H., Sprengel W., and Denkinger M.; ASM/TMS Proc., Chicago, IL., (1992).

57. Hashimoto K., Doi H., Kasahara K., Tsujimoto T., and Suzuki T.; J. Japan Inst. Metals, 52 (8), 816-825, (1988).

APPENDIX

Table 1. Properties of Titanium Aluminides, Titanium-Base Conventional Alloys, Super alloys, and 4340 Steel

Property	Ti Base	Ti_3Al Base	TiAl Base	Super alloy Inconel 601 Solution Treated	4340 Quenched Tempered
Density (Kg/m^3) (x 1000)	4.5	4.1-4.7	3.7-3.9	8.1	7.8
RT Modulus (GPa)	96-115	120-145	160-176	207	207
Yield Strength (MPA)	380-1150	700-990	400-630	380	900-1400
Tensile Strength (MPa)	480-1200	800-1140	450-700	760	960-1500
Creep Limit (C)	600	750	1000	1095	
Oxidation (C)	600	650	900-1000	1095	
Ductility (%) RT tensile	10-20	0	1-3	40	12-25
Ductility (%) HT tensile	High	10-20	10-90	90	20-50 (650 C)
Structure	HCP/BCC	DO_{19}	$L1_0$	FCC	BCC
K1c (MPa$\sqrt{m}$)	57	20-30	10-12		55-105
Specific Yield Strength (MPa)	84-256	159-225	105-166	47	115-179
Specific Tensile Strength (MPa)	107-267	182-259	118-184	94	123-192

Source: Kim Y.; JOM, July, 24-30, (1989)., ASM; Metals Handbook, 1, ASM, Metals Park Ohio, (1961)., Callister W.; Materials Science and Engineering, John Wiley and Sons, New York, New York, (1985)., ASM: Source Book on Industrial Alloy and Engineering Data, ASM, Metals Park, Ohio, (1978)., Courtney T., Mechanical Behavior of Metals, McGraw-Hill, New York, New York, (1990)., Huntington Alloy Products Division, Huntington Alloys, The International Nickel Company, Huntington, West Virginia, (1983).

Table 2. Ternary Alloy Compositions Studied
Assuming Different Substitution Behaviors
x = Ag, Cr, Ga, Mn, and Zr

	Random Substitution	Ti Substitution	Al Substitution
x in a/o	1-5	1-5	1-5
Ti in a/o	49.5-47.5	49-45	50
Al in a/o	49.5-47.5	50	49-45

Table 3. Estimate of Accuracy of EDX Analysis
on Single Phase TiAl Alloys, Where SDEV is 1 Standard Deviation

Alloy in a/o	EDX, Average Measured Composition a/o Al (SDEV)	Actual Composition a/o Al (SDEV)	Maximum Difference Between Measured and Actual Composition
Ti-50/Al-50 (arc melt/homogenized)	49.5 (0.32)	50.0 (0.11)#	0.9
Ti-52/Al-48 (splat quenched)	51.8	52.3(0.00)	0.5

Based on weight loss calculations

Table 4. Estimate of Resolution of EDX Analysis on TiAl Alloys
Where SDEV is 1 σ Standard Deviation

Alloy in a/o	Date Run EDX	EDX, Measured Composition of γ in a/o Al (SDEV)	Average for all γ Measurements Made in a/o Al (SDEV)
Ti-55/Al-45	8/12/92	46.96 (0.10)	-----
"	9/10/92	47.22 (0.33)	-----
"	9/15/92	46.98 (0.20)	-----
"	-----	-----	47.05 (0.23)

Table 5. Dissolved Impurity Analysis of Homogenized Alloys

Alloy in a/o	Casting Procedure	C in ppm by weight	N in ppm by weight	O in ppm by weight
Ti-50/Al-49/Zr-1	Drop Cast	39	15	201
Ti-55/Al-45	Arc Melt	86	13	603
Ti-49.5/Al-49.5/ Cr-1	Arc Melt	96	8	423
Ti-48/Al-48/Mn-2/Ga-2	Zone Process	68	20	285
Relative Accuracy	------	10%	15%	10%

Table 6. K Factor Relative to Silicon for Elements Analyzed using ALCHEMI

Element	K factor
Al	0.963
Ti	1.181
Cr	1.237
Mn	1.28
Zr	0.71

Table 7. Site Occupancy Behavior in TiAl for Cr, Mn, and Zr. Determined from ALCHEMI Results Using Multivariant Analysis. SDEV is 1 σ Standard Deviation.

Alloy	% occupancy of impurity on Al sites (SDEV)	% occupancy of impurity on Ti sites (SDEV)	Calculated composition of impurity in a/o (SDEV)	Composition of impurity determined from EDX on SEM in a/o (SDEV = 1 a/o)
Ti-48/Al-49/Cr-3	75.4 (2.0)	24.6 (0.9)	4.4 (0.1)	3
Ti-48/Al-50/Mn-2	49.6 (3.4)	50.4 (2.3)	2.3 (0.1)	2
Ti-49/Al-49/Zr-2	1.9 (6.2)	98.1 (6.2)	1.0 (0.1)	2

Table 8. Phase Boundary Compositions for a Ti-45Al Alloy Homogenized at 1100 C for 100 hr. Followed by Cooling to 600 C and Holding for Various Times Before Quenching to Room Temperature.

Time @ 600 C (hr) after 1100 C homogenization for 100 hr	a/o Al of $\alpha 2+\gamma/\gamma$ boundary (SDEV)	a/o Al of $\alpha_2/\alpha 2+\gamma$ boundary (SDEV)	% α_2 determined from lever rule	% α_2 determined from histogram
3	47.2 (0.3)	38.7 (0.7)	23	28
10	47.4 (0.3)	39.4 (0.3)	30	23
100	47.1 (0.5)	39.1 (0.1)	26	23
1000	47.1 (0.1)	39.0 (0.1)	26	23

Table 9. Four Point Bend Test Results for Zone Processed and Homogenized Alloys

Alloy	Fracture Stress in MPa (SDEV)	% Strain at Fracture (SDEV)	Fracture Stress for K1 Test in MPa (SDEV)	Stress Intensity Factor K1 in MPa $\sqrt{m}$ (SDEV)	Average Colony/Grain Size on Tensile Surface in mm	% α_2 Present
Ti-50/Al-50	348.38 (31.0)	0.49 (0.08)	143.8 (23.5)	10.7 (1.2)	0.8	9
Ti-52/Al-48	400.51 (47.5)	0.42 (0.13)			2.3	15
Ti-49.5/ Al-49.5/ Cr-1	370.63 (4.81)	0.51 (0.07)			0.6	5
Ti-48.5/ Al-48.5/ Cr-1/ Mn-2	468.26 (21.6)	0.57 (0.11)			0.3	9
Ti-48.5/ Al-49/ Cr-1 /Zr-1	404.69 (16.2)	0.40 (0.03)	224.2 (25.6)	14.3 (2.9)	0.4	4
*Ti-48/ Al-48 / Mn-2/ Zr-2	398.29 (49.3)	0.31 (0.07)	173.0 (73.5)	11.0 (3.9)	0.3	4
Ti-48/Al-48/Ga-2/ Mn-2	392.29 (40.1)	0.45 (0.16)			0.5	3

* This alloy was contaminated with copper.

Table 10. Average Percent Plastic Strain Determined by a Linear Offset Method for Zone Processed and Homogenized Alloys Subjected to Four Point Bending. Percent Strain Determined via Strain Gages

Alloy	Average Percent Plastic Strain	Standard Deviation
Ti-50/Al-50	0.32	0.10
Ti-52/Al-48	0.17	0.11
Ti-49.5/Al-49.5/ Cr-1	0.30	0.07
Ti-48.5/Al-48.5/ Cr-1/Mn-2	0.29	0.11
Ti-48.5/Al-49 Cr-1/Zr-1	0.17	0.03
*Ti-48/Al-48/ Mn-2/Zr-2	0.08	0.04
Ti-48/Al-48/ Ga-2/Mn-2	0.22	0.16

* This alloy was contaminated with copper.

Table 11. Literature Four Point Bend Data for Arc Melted and Homogenized Alloys. Testing Dimension Thickness was 1mm.

Alloy	Fracture Stress (MPa)	Percent Fracture Strain
Ti-50/Al-50	230	1.8
Ti-52/Al-48	470	1.6
Ti-50/Al-49/Cr-1	340	1.8

Source: Kawabata T., Tamura T., Izumi O.; Mat. Res. Soc. Symp., 133, 329-334. (1989).

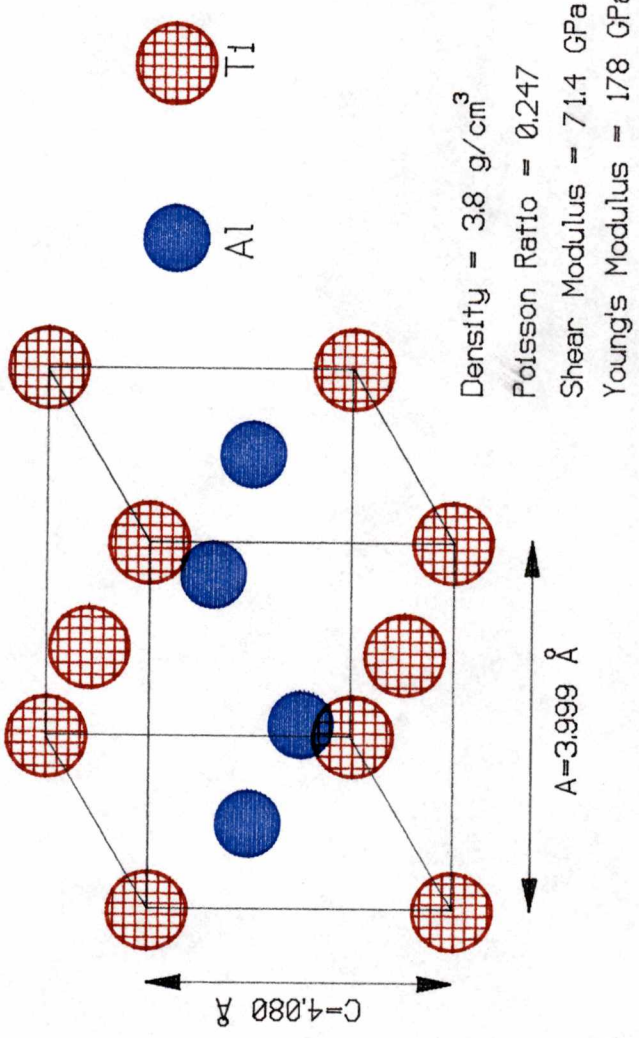


Figure 1. Unit Cell of Stoichiometric TiAl Showing a Typical Slip Plane and Some Physical Properties

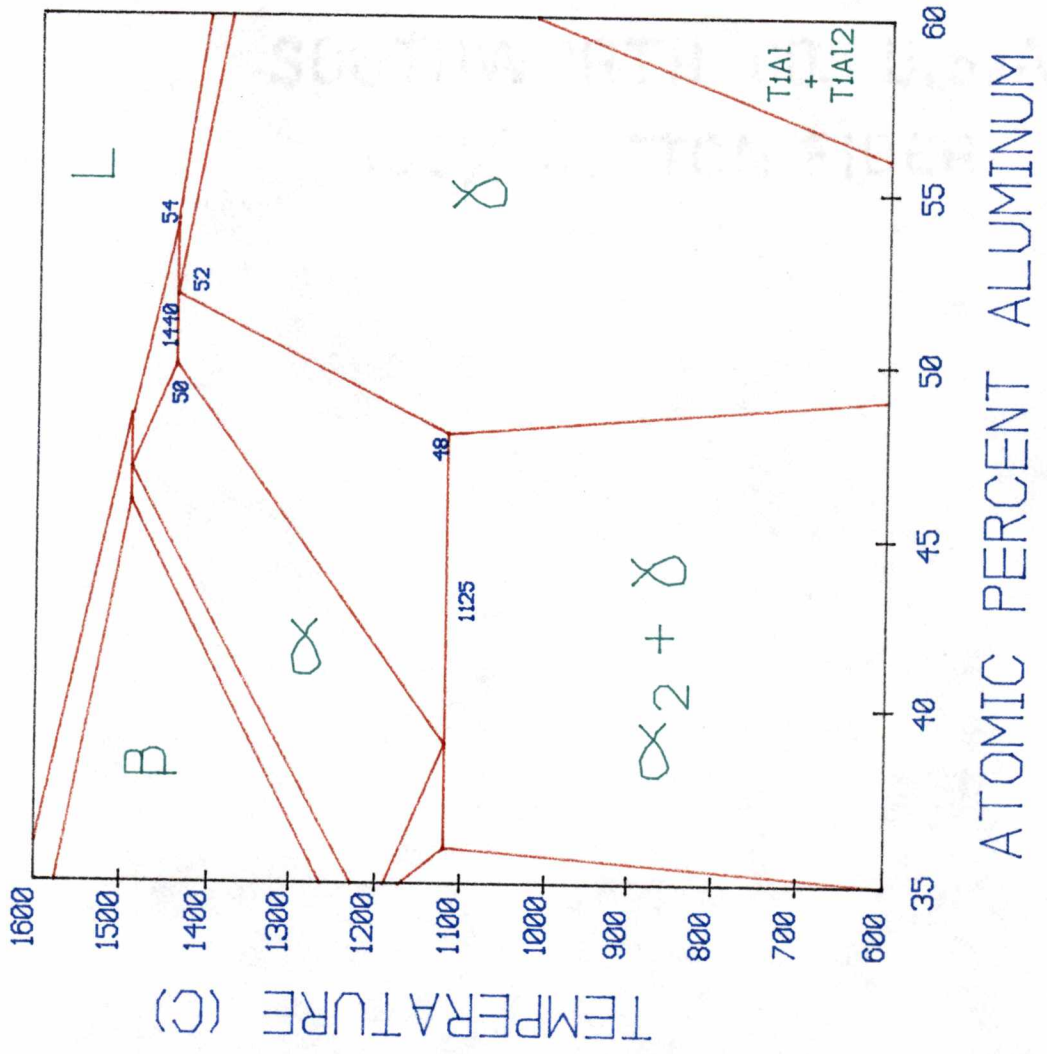


Figure 2. Binary Ti-Al Phase Diagram

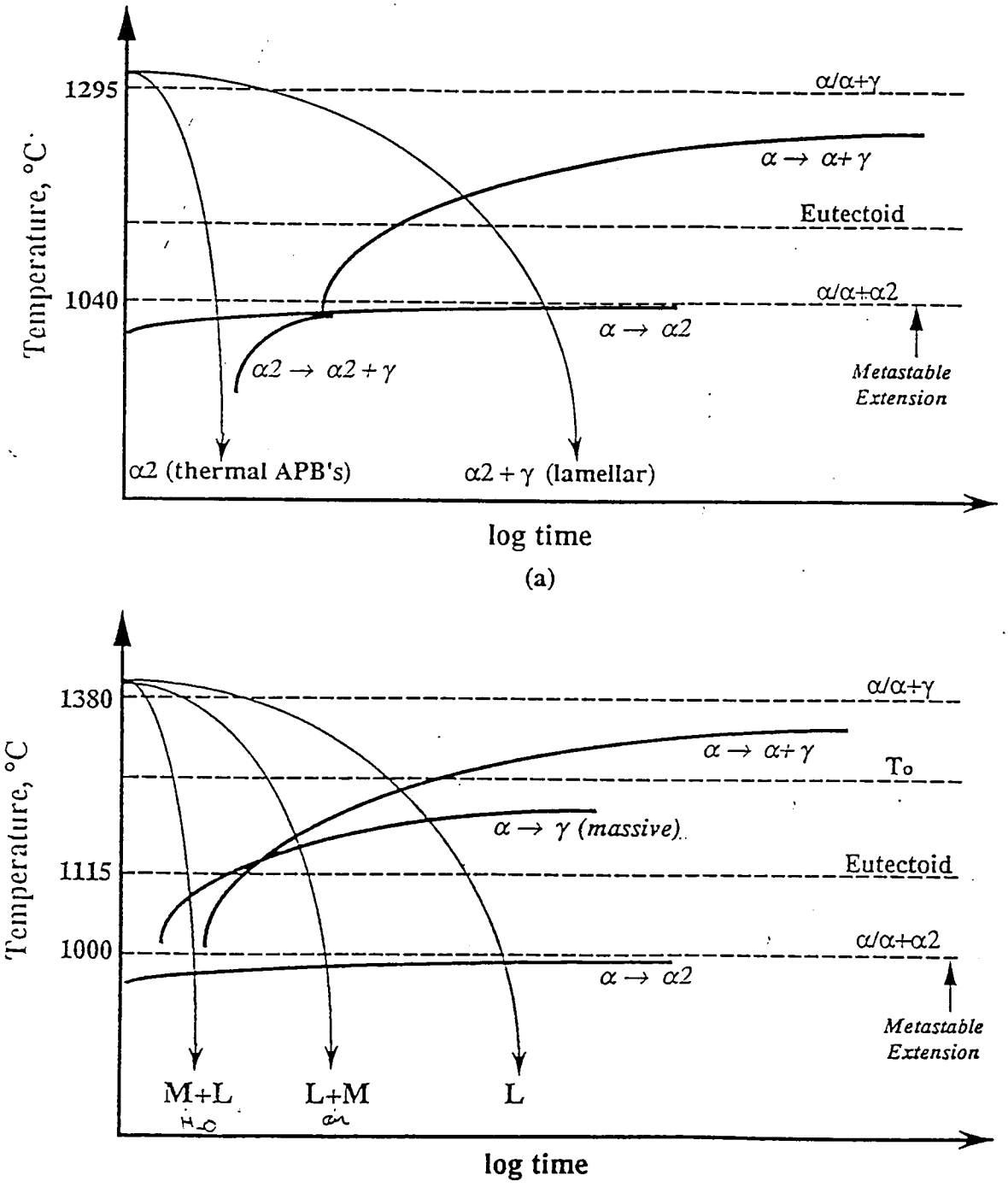


Figure 3. Schematic CCT Diagrams for Both 45 Al (a) and 48 Al (b) Representing the Decomposition of the High Temperature **α** Phase.
M = Massive, L = Lamellar [21].

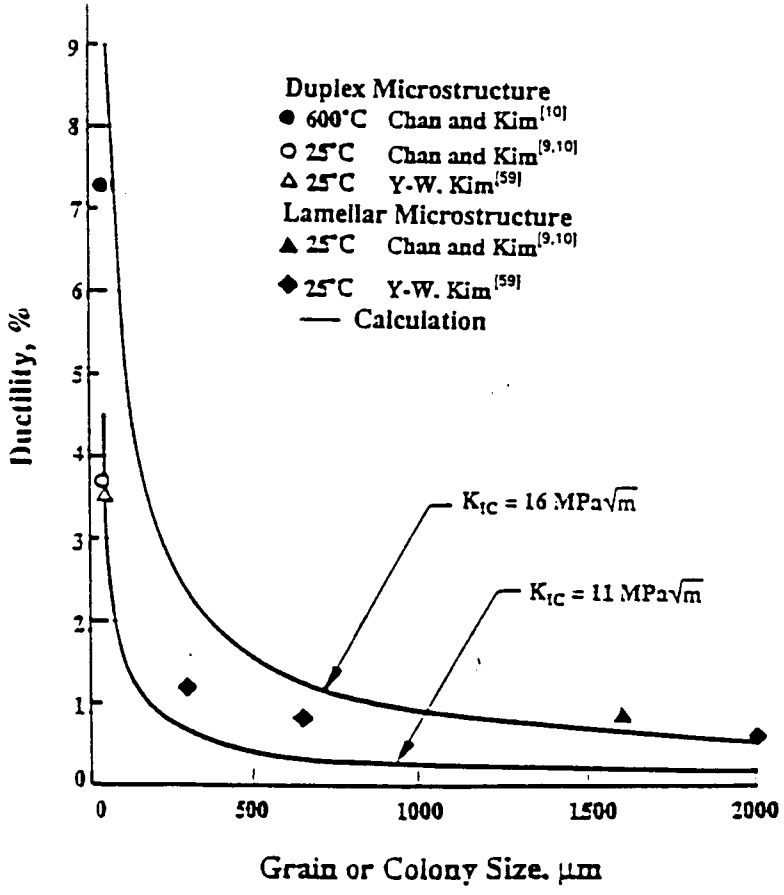


Figure 4. A Comparison of Observed and Calculated Tensile Ductility as a Function of Grain Size or Colony Size for Ti-48.4/Al-47/Nb-2.6/(Cr+V)-2. Calculated Curves Obtained Using a Micromechanical Model [25].

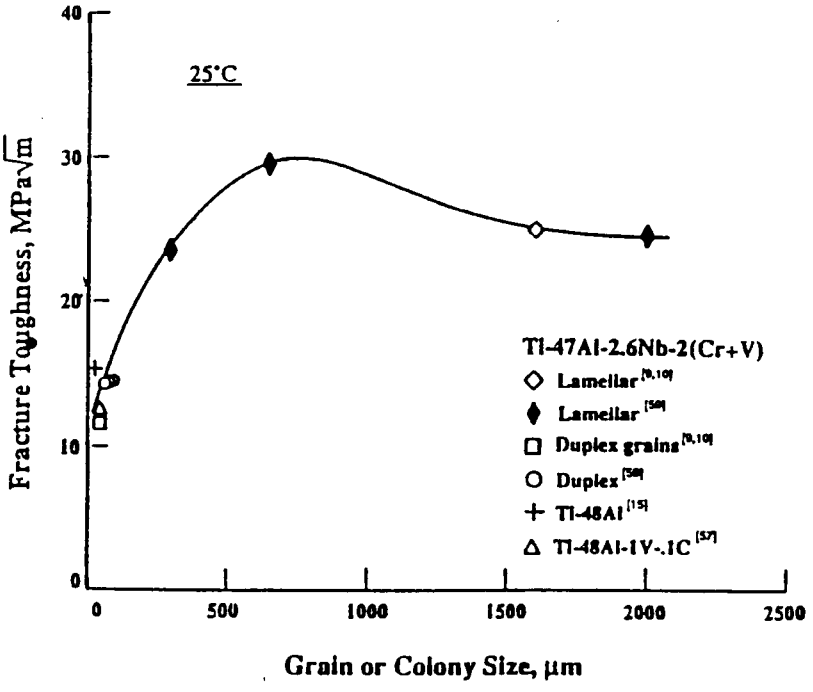


Figure 5. The Dependence of Fracture Toughness on Grain Size or Colony Size for Various TiAl Alloys [25].

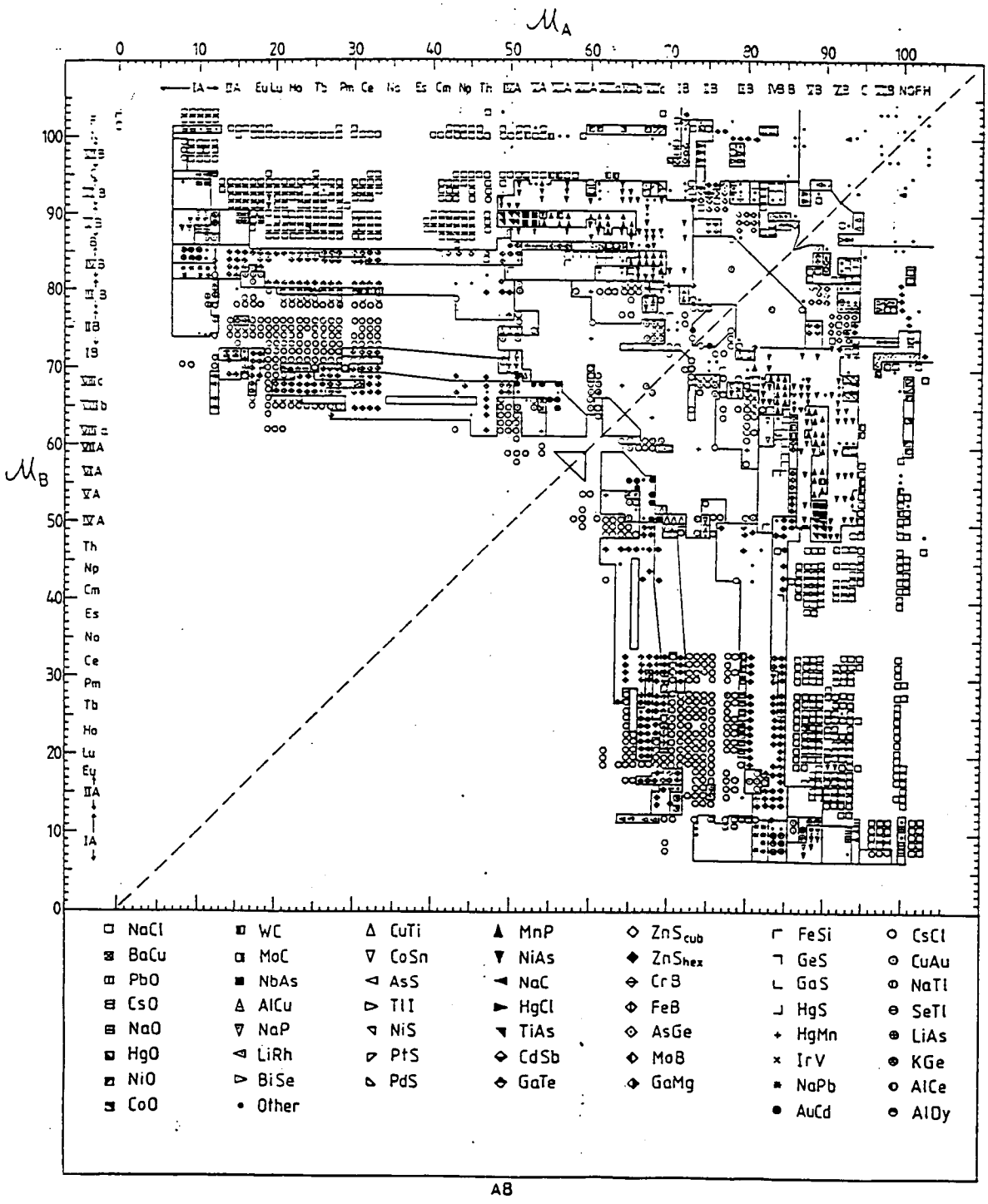


Figure 6. AB Structure Map [26].



Figure 7. Typical Bend Contour Showing Locations of EDX Analysis. Sites A–D are off Exact Channelling Conditions. Site E is the Exact Channelling Condition.

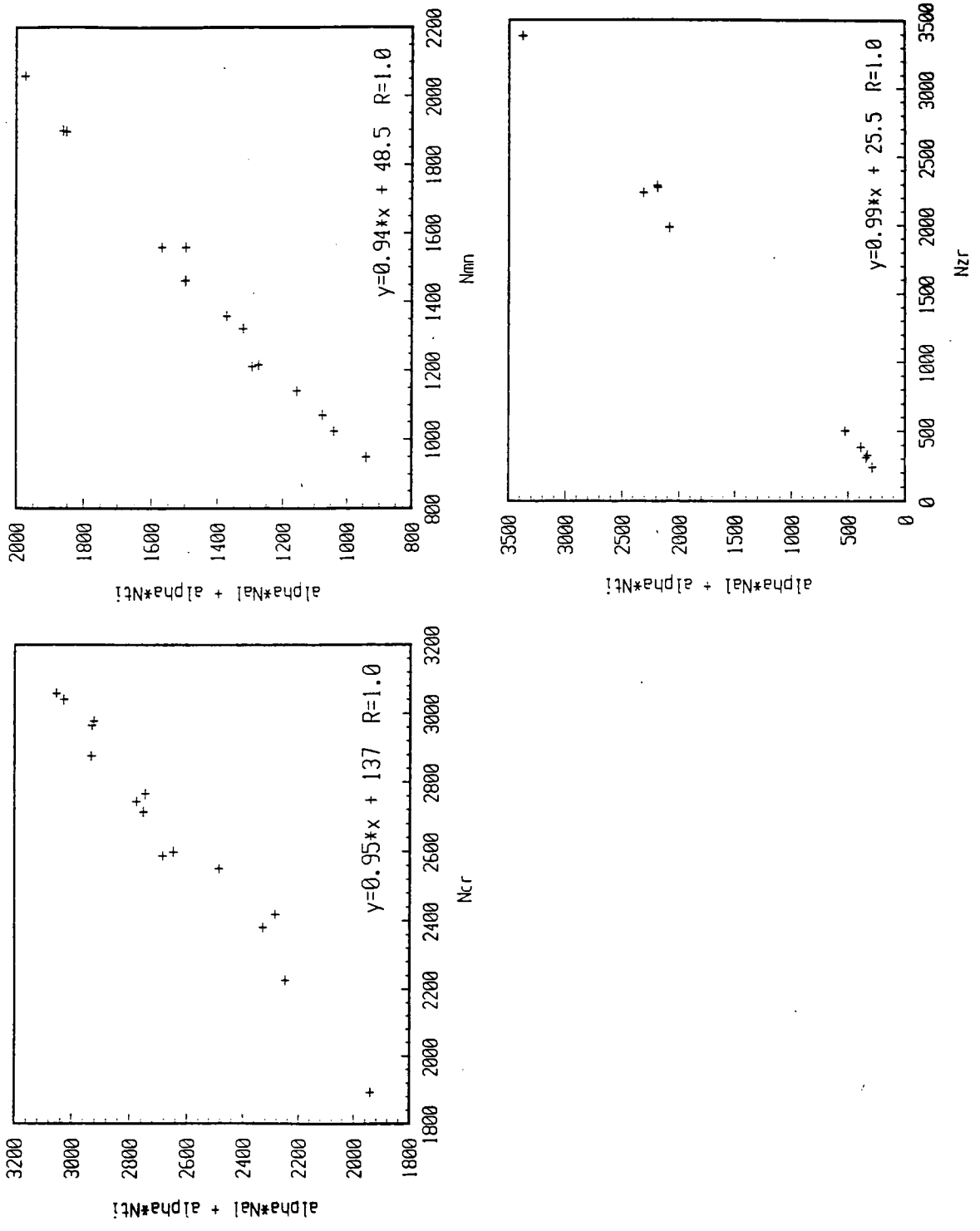


Figure 8. Plots of Impurity Counts (Cr, Mn, and Zr) Versus $\Sigma\alpha_i N_i$ Showing Linear Fit to Model Assumed by the Mutivariant Analysis Technique Used to Calculate ALCHEMI Data.

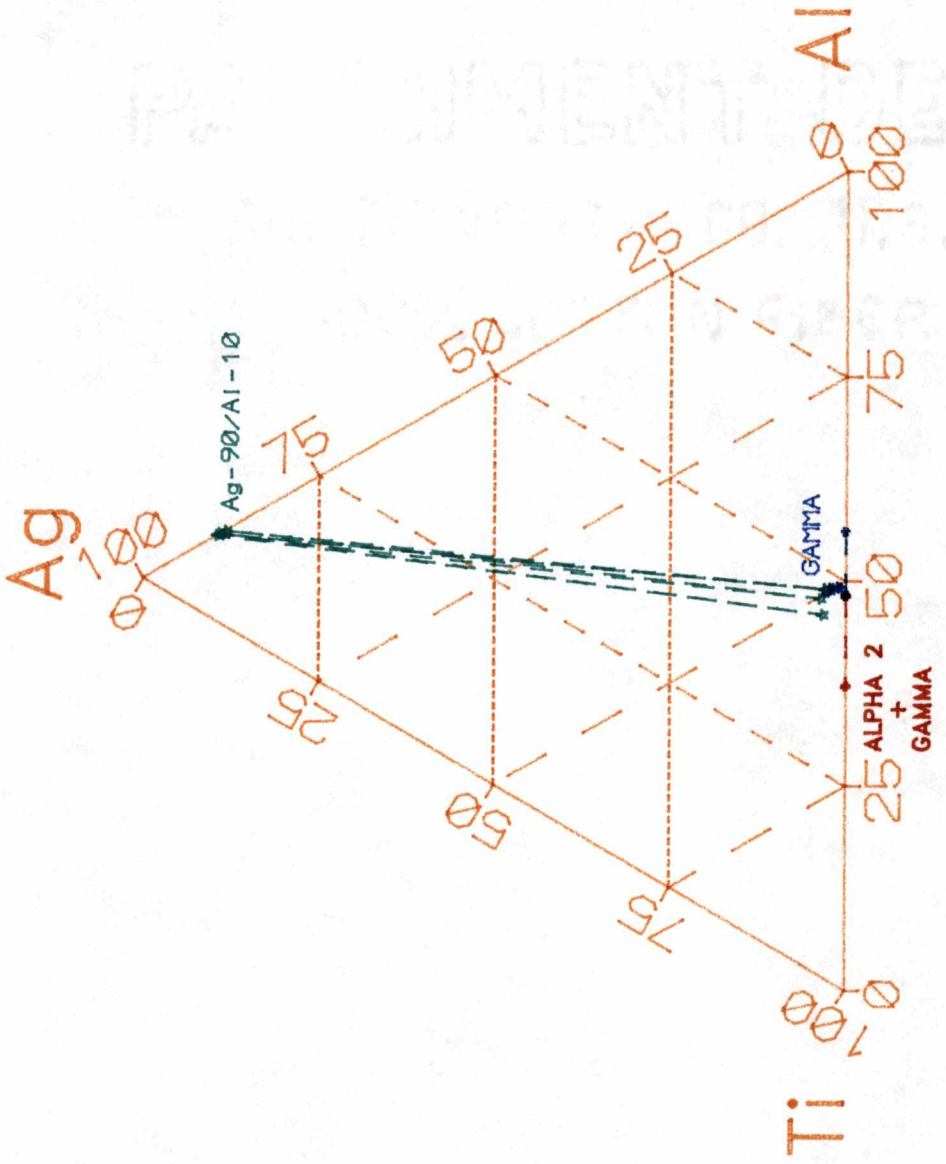


Figure 9. Experimental 1100 C TiAl+Ag Ternary Phase Diagram.

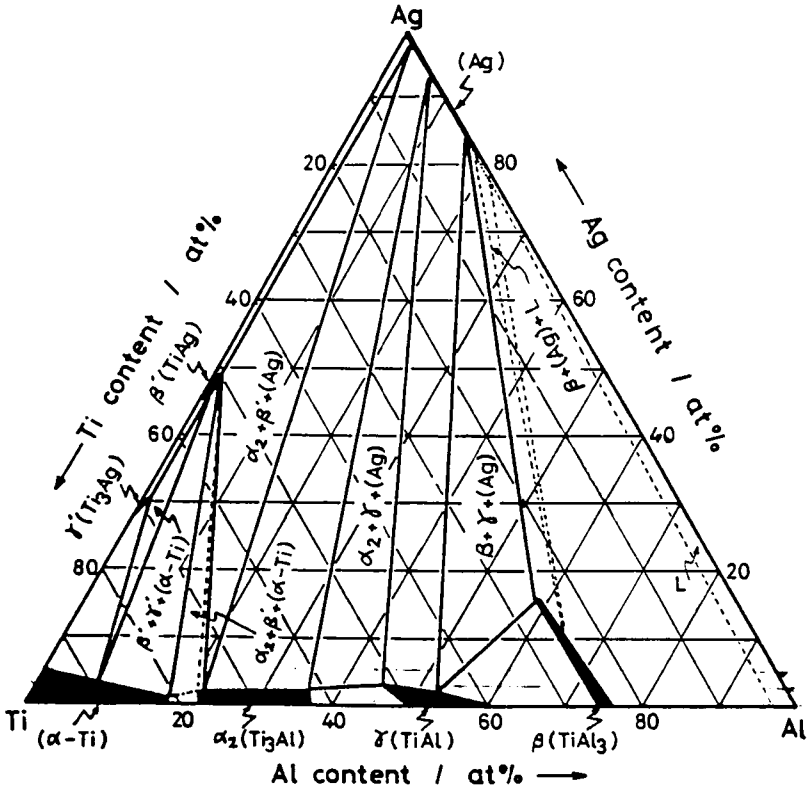


Figure 10. 800 C TiAl+Ag Ternary Phase Diagram Proposed by Hashimoto et al. [47].

a)

150 nm



b)

12 nm

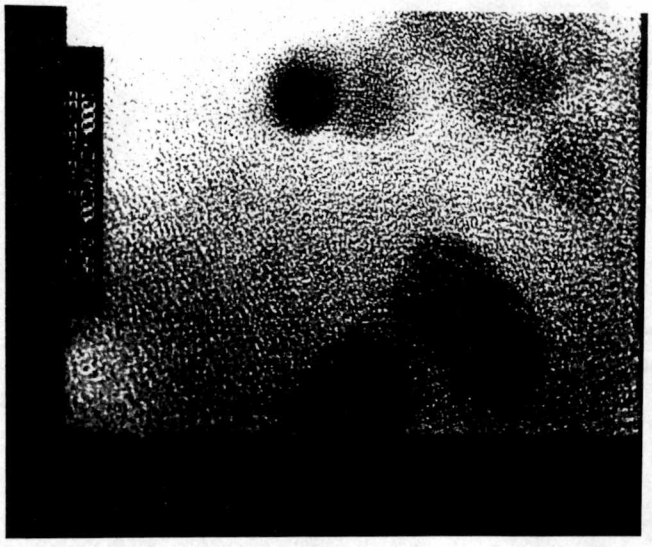


Figure 11. CBED Image Showing Small Second Phase in Ti-50/Al-48/Ag-2 Homogenized Alloy. a) 80 kx Magnification Showing Distribution of Second Phase. b) 1000 kx Magnification Showing Second Phase Particles.

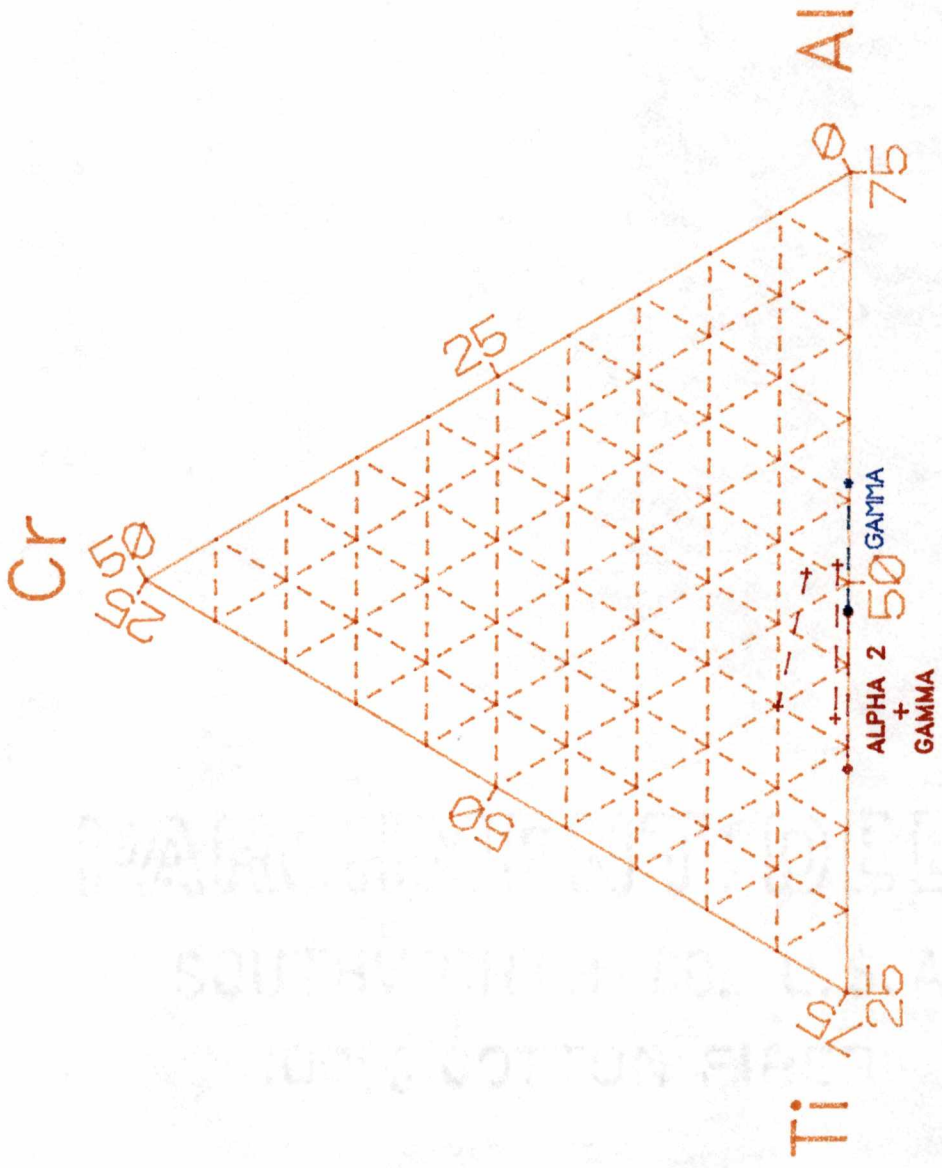


Figure 12. Experimental 1100 C TiAl+Cr Ternary Phase Diagram.

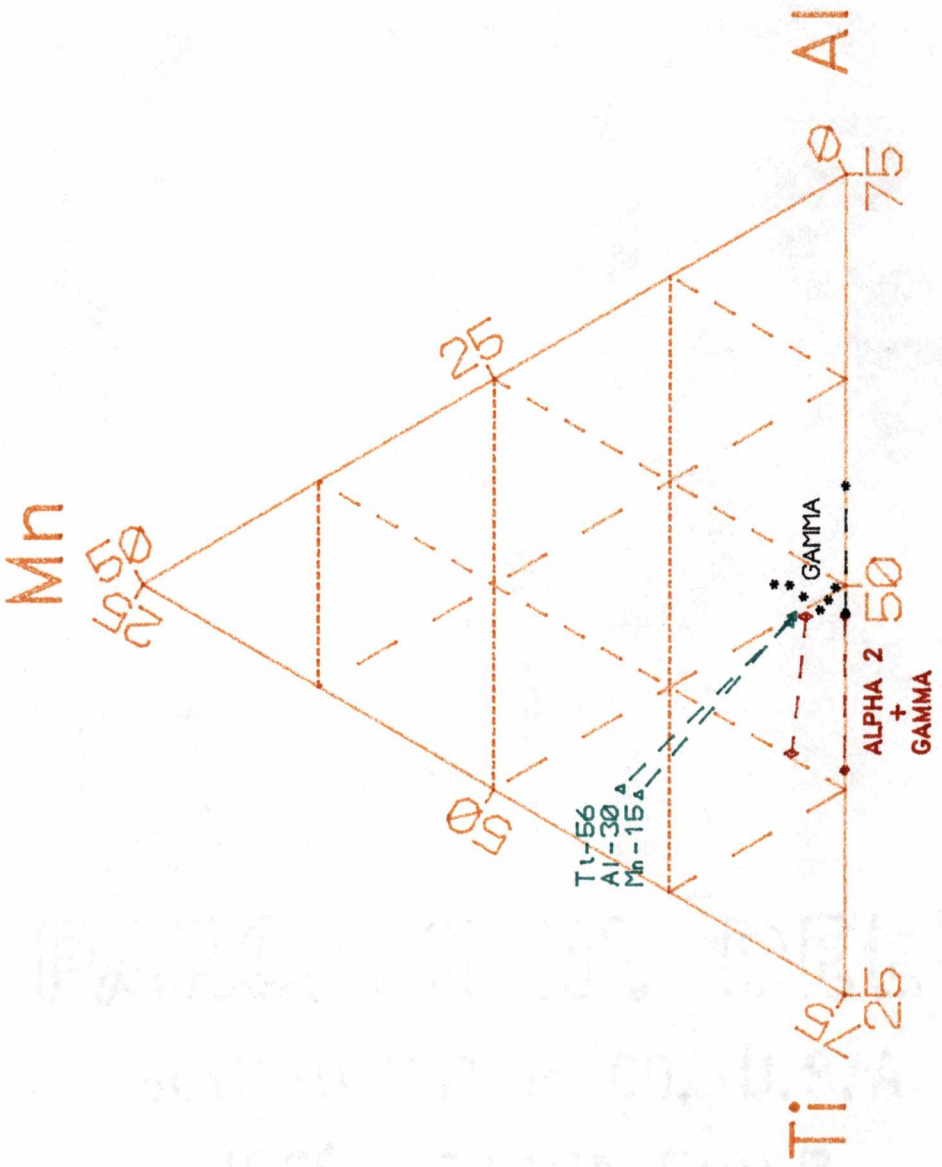


Figure 13. Experimental 1100 C TiAl+Mn Ternary Phase Diagram.

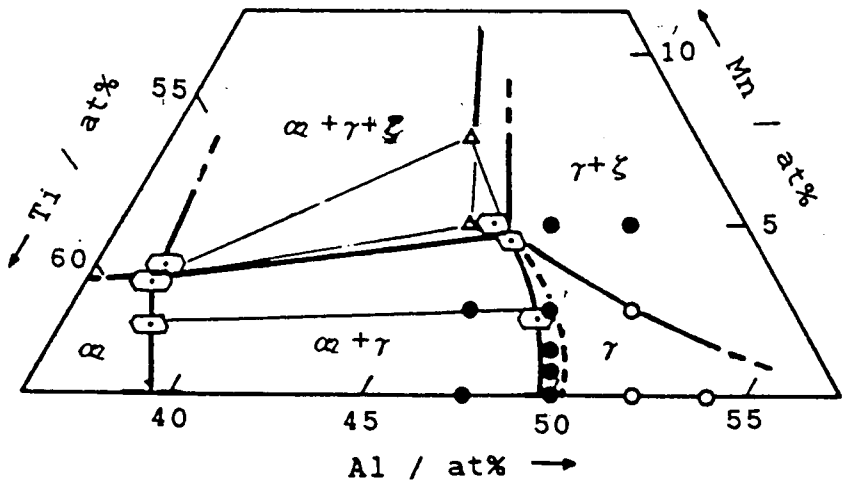


Figure 14. 1000 C TiAl+Mn Ternary Phase Diagram Proposed by Hashimoto et al. [57].

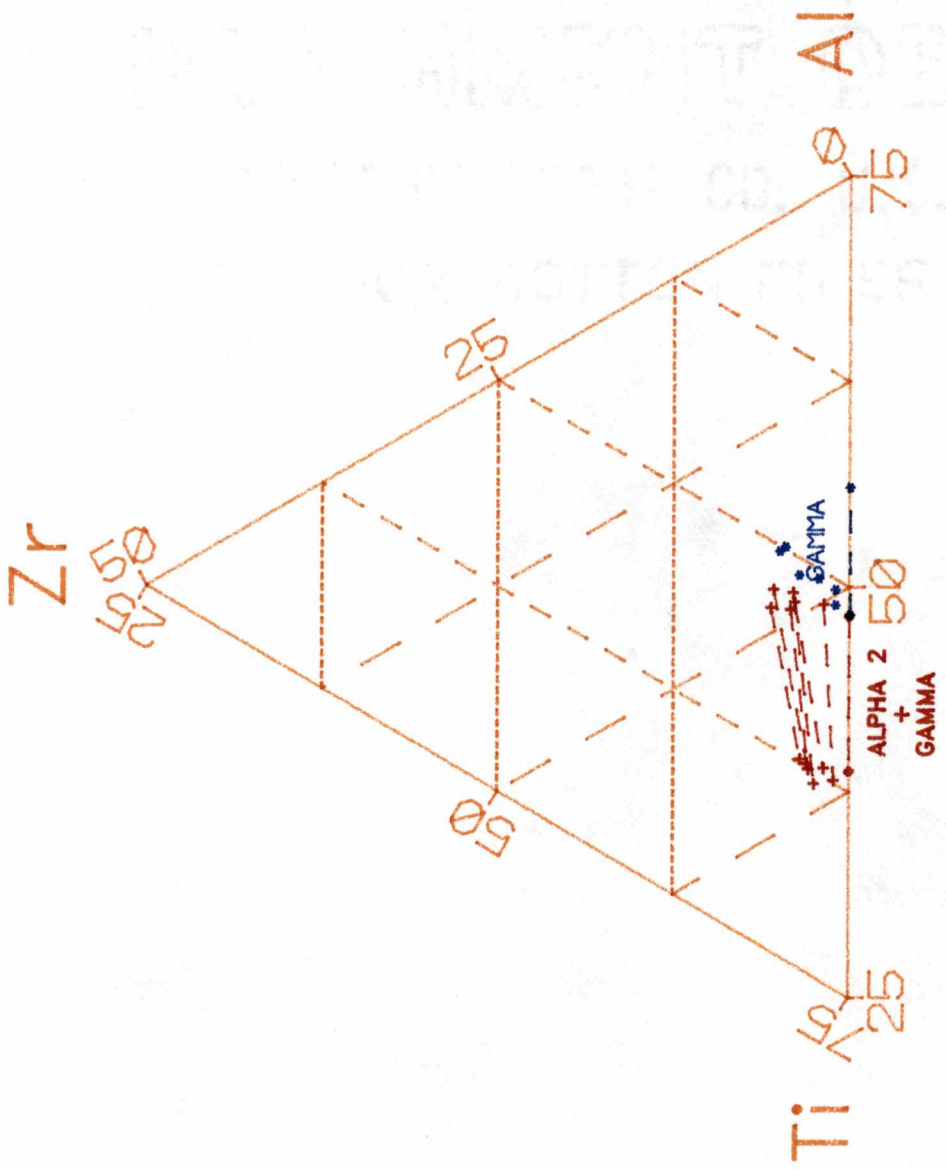


Figure 15. Experimental 1100 C TiAl+Zr Ternary Phase Diagram.

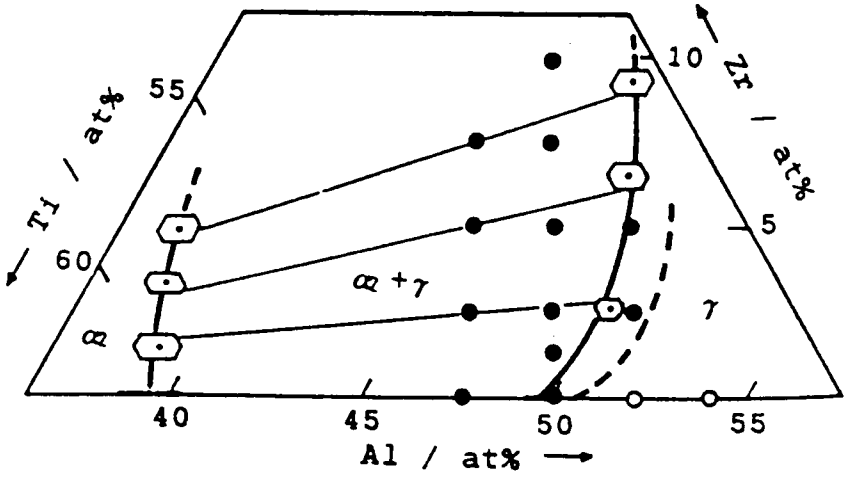


Figure 16. 1000 C TiAl+Zr Ternary Phase Diagram Proposed by Hashimoto et al. [57].

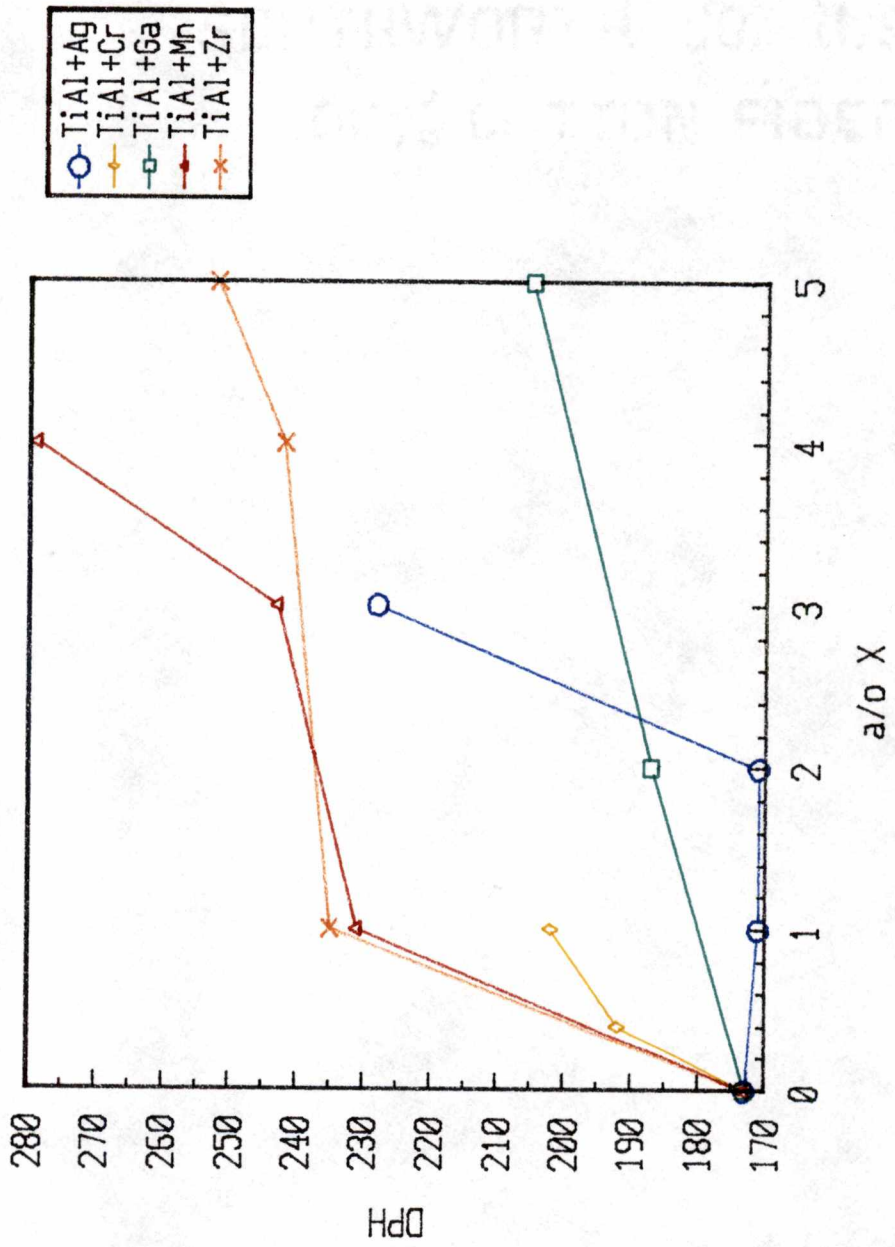


Figure 17. Homogenized Hardness versus Alloying Addition, x, for Single Phase TiAl Ternary Alloys, Where x = Ag, Cr, Ga, Mn, and Zr. Based on the Substitution Behavior of x, all Alloys Assume an Effective "Ti"/"Al" ratio Equal to Unity.Typical SDEV=+/-20 DPH.

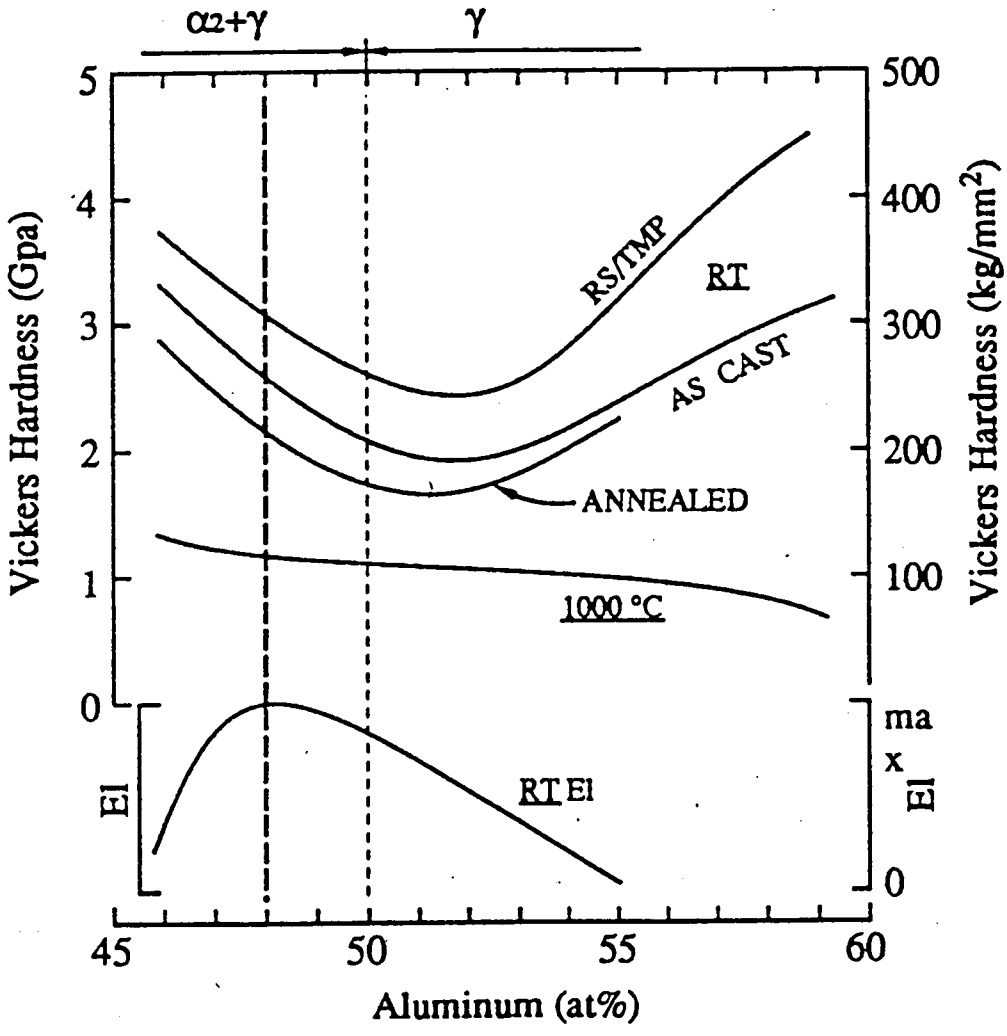
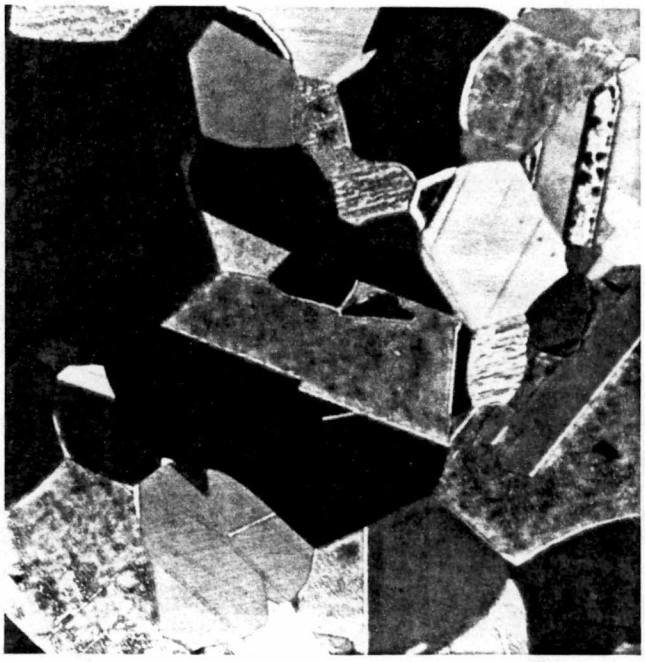


Figure 18. Hardness and Tensile Elongation versus Aluminum Content for Binary TiAl Alloys [1].



a)

250 μm



b)

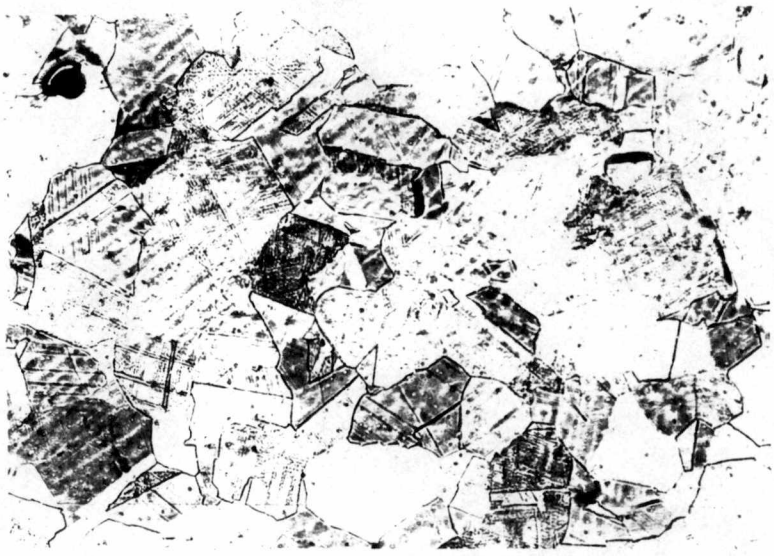
250 μm

Tension Side

Figure 19. Typical Optical Microstructure and Fractograph for Arc Melted and Homogenized Ti-50/Al-50. a) Optical Micrograph, Etched b) SEM Fractographs Showing Tension side of Fracture Surface, Produced by Vice Bend Test.

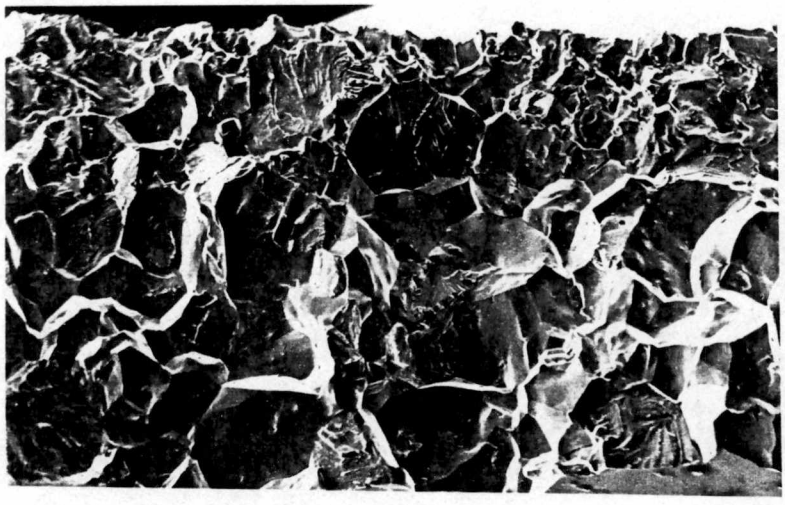
a)

250 μm



b)

250 μm

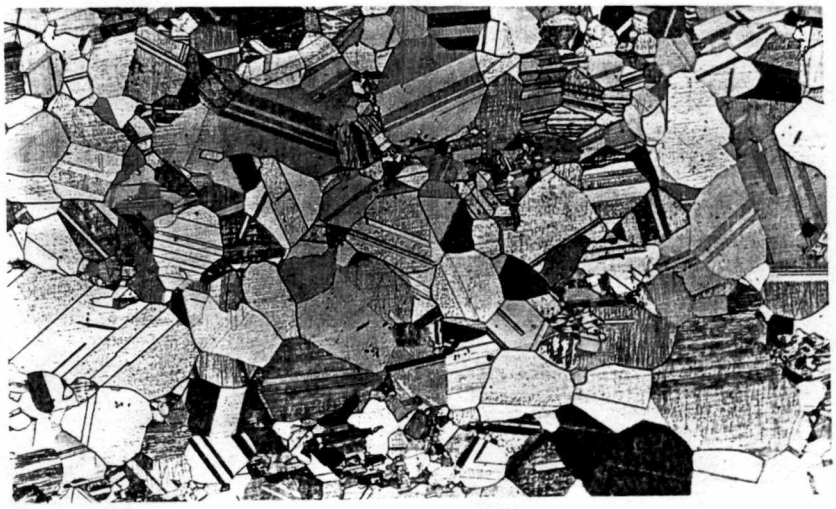


Tension Side

Figure 20. Typical Optical Electro Polished Microstructures and Fractographs for Drop Cast and Homogenized Ti-50/Al-48/Ag-2. a) Optical Micrograph, Etched b) SEM Fractographs Showing Tension Side of Fracture, Produced by Vice Bend Test.

a)

250 μm



b)

250 μm

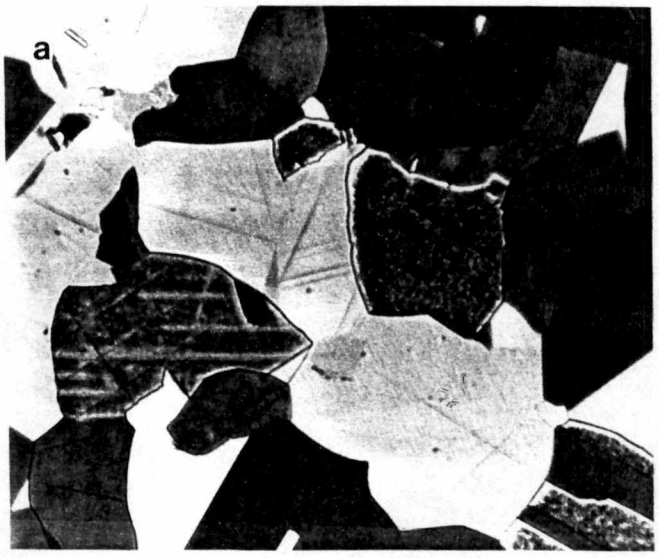


Tension Side

Figure 21. Typical Optical Microstructures and Fractographs for Arc Melted and Homogenized Ti-48.5/Al-48.5/Cr-3. a) Optical Micrgraph, Etched b) SEM Fractographs Showing Tension Side of Fracture Surface, Produced by Vice Bend Test.

a)

250 μm



b)

250 μm



Tension Side

Figure 22. Typical Optical Microstructures and Fractographs for Arc Melted and Homogenized Ti-50/Al-48/Ga-2. a) Optical Micrograph, Etched b) SEM Fractographs Showing Tension Side of Fracture Surface, Produced by Vice Bend Test.

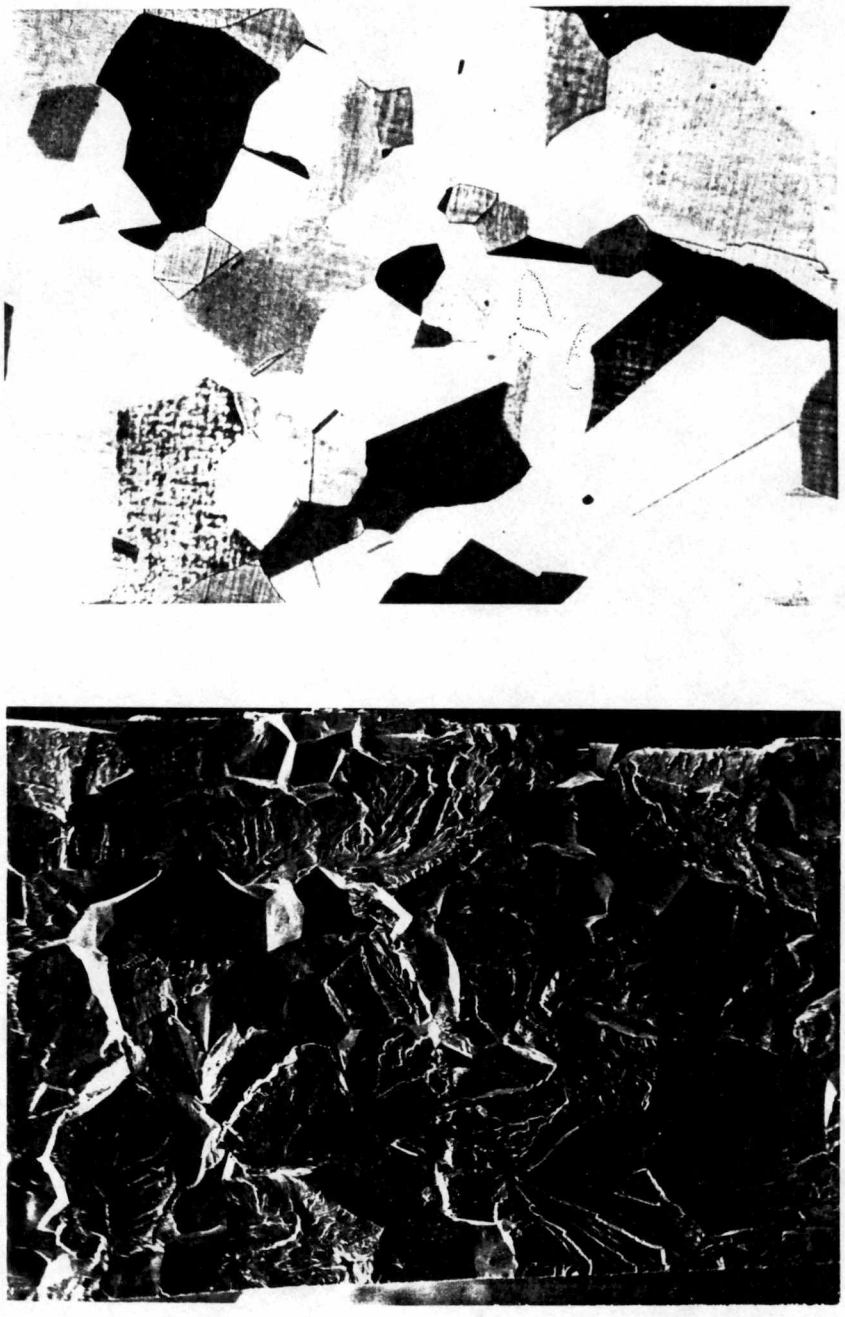


Figure 23. Typical Optical Electro Polished Microstructures and Fractographs for Arc Melted and Homogenized Ti-48/Al-50/Mn-2. a) Optical Micrograph, Etched b) SEM Fractographs Showing Tension Side of Fracture Surface, Produced by Vice Bend Test.

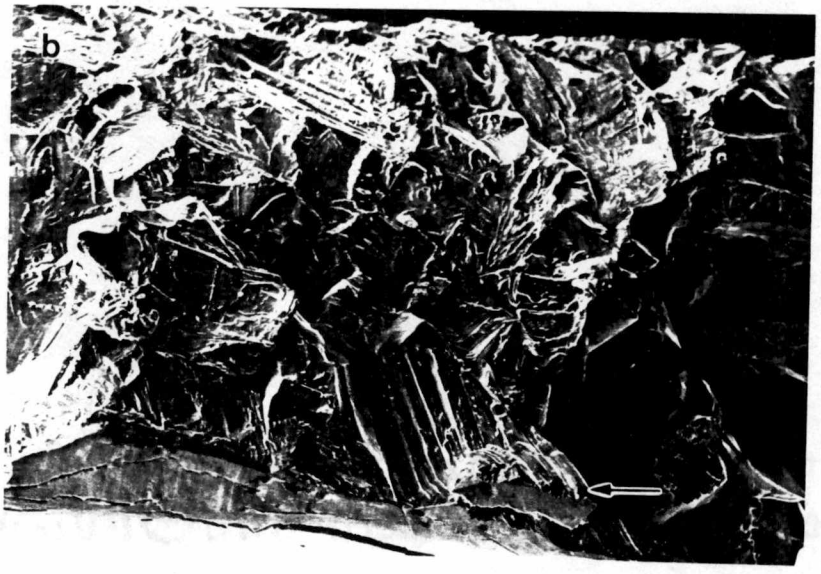
a)

250 μm



b)

250 μm

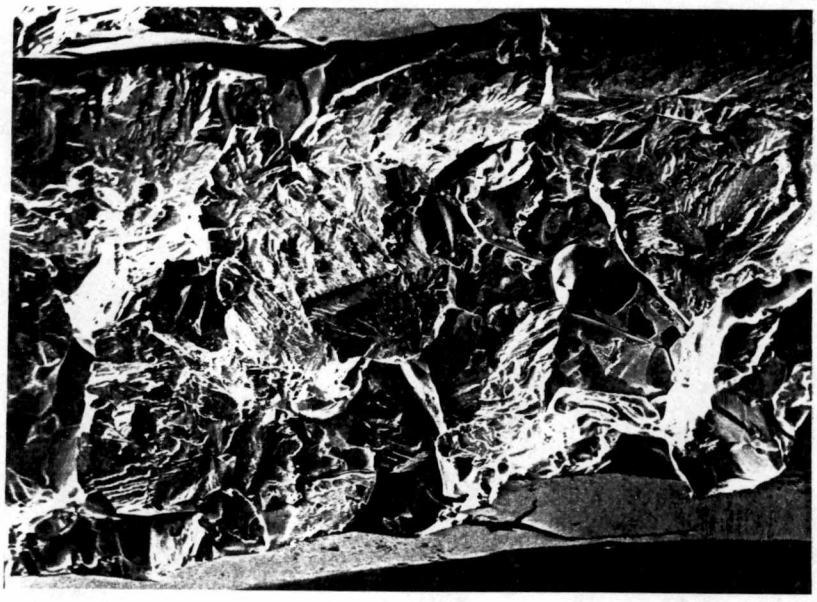


Tension Side

Figure 24. Typical Optical Electro Polished Microstructures and Fractographs for Drop Cast And Homogenized Ti-49.5/Al-49.5/Zr-1. a) Optical Micrograph, Etched b) SEM Fractographs Showing Tension Side of Fracture Surface, Produced by Vice Bend Test. Arrow Points to Bent Grain.

a)

250 μm



Tension Side

b)

50 μm



Tension Side

Figure 25. Fractograph of Drop Cast and Homogenized Ti-50/Al-46/Ag-4 Showing a Ag-Al Solid Solution Along a Grain Boundary. a) low magnification, 50x b) Same Area as a) but Higher Magnification.



Figure 26. Typical Optical Electro-polished Microstructures for Arc Melted and Homogenized Ti-50/Al-50, Etched.

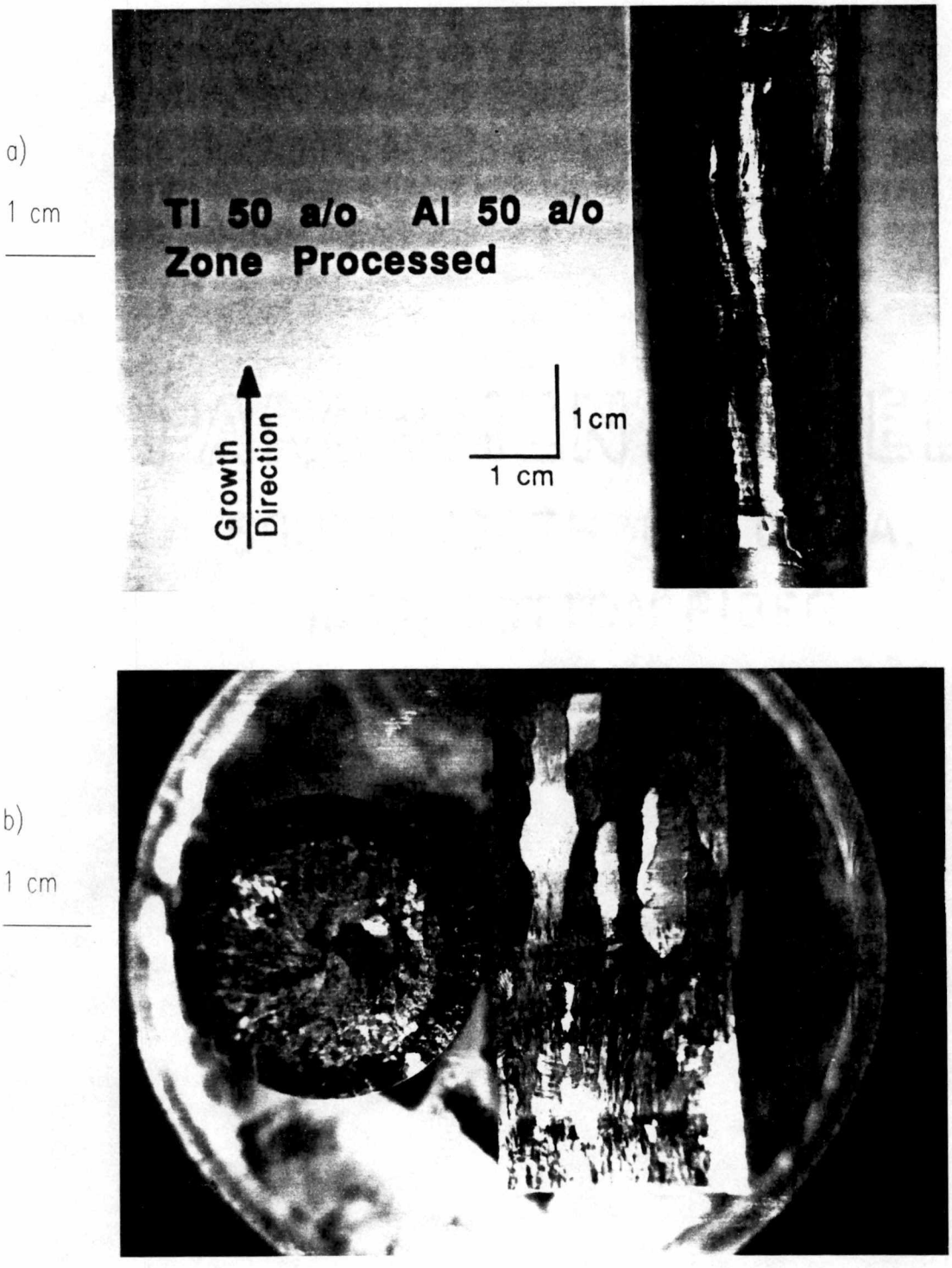


Figure 27. Macro of Zone Melted Ti-50/Al-50. a) Exterior of ingot b) Transverse and Longitudinal Section, Etched. Growth Direction from Bottom to Top of Photograph.

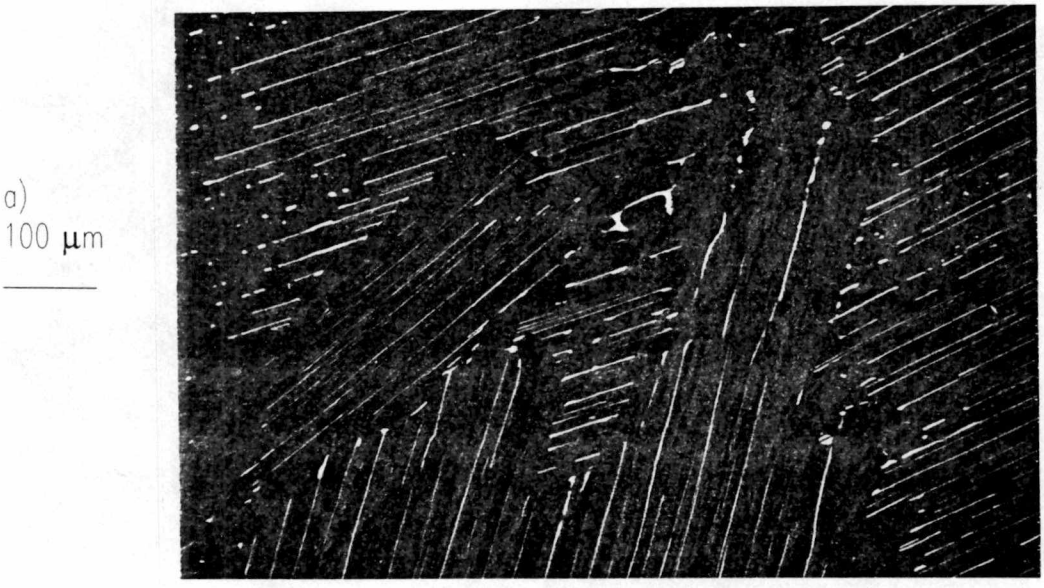
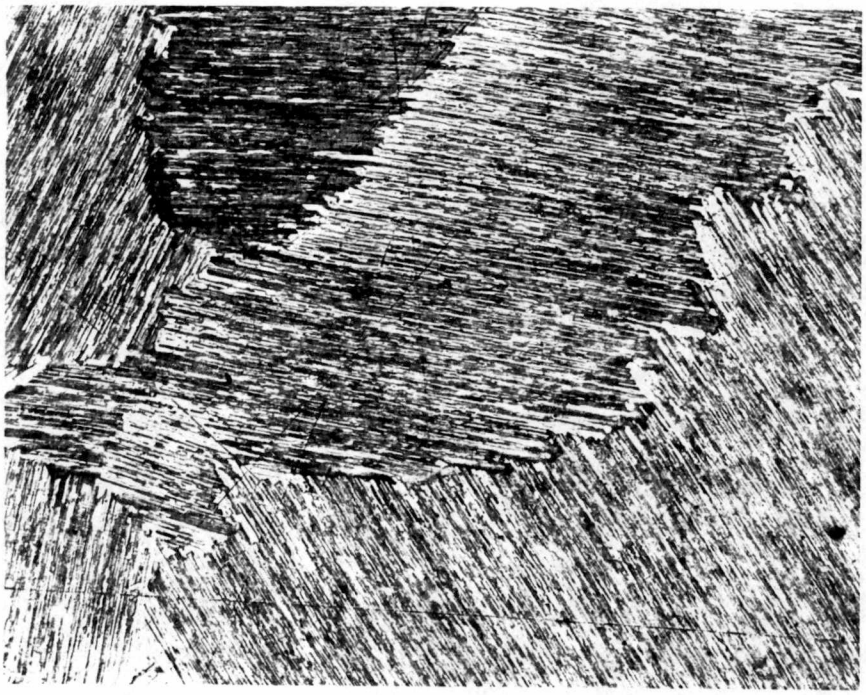


Figure 28. Microstructure of Zone Processed Ti-50/Al-50. a) SEM Backscattered Image for Homogenized Sample Showing Fine $\alpha 2$ b) Optical Microstructure Showing Lamellar Colonies, Etched c) Optical Microstructure Showing Proeutectoid γ at Prior α Boundaries, Etched. Growth Direction from Bottom to Top of Photographs for b) and c). Arrows in c) Point to Blocky γ.

b)

250 μm



c)

50 μm

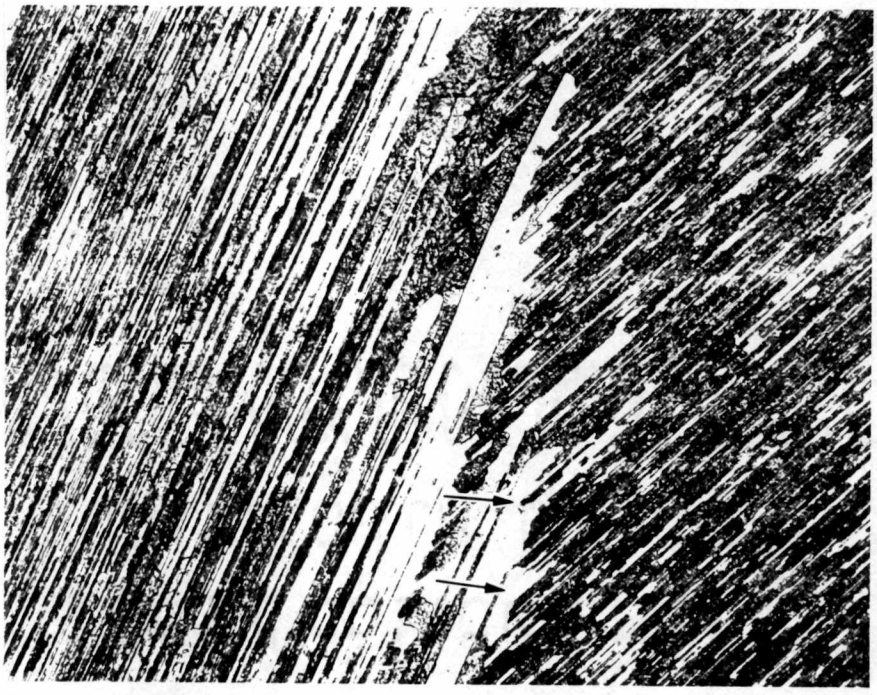
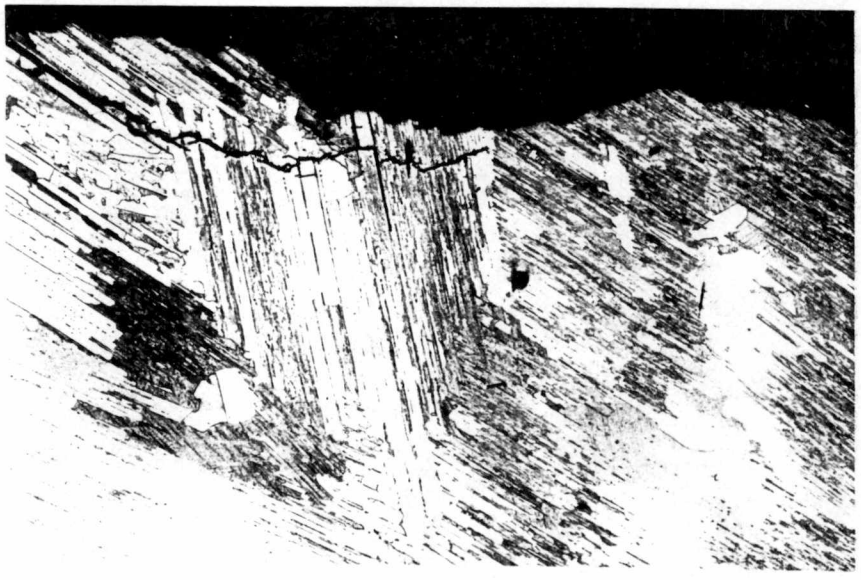


Figure 28 Continued.

a)

250 μm



b)

50 μm

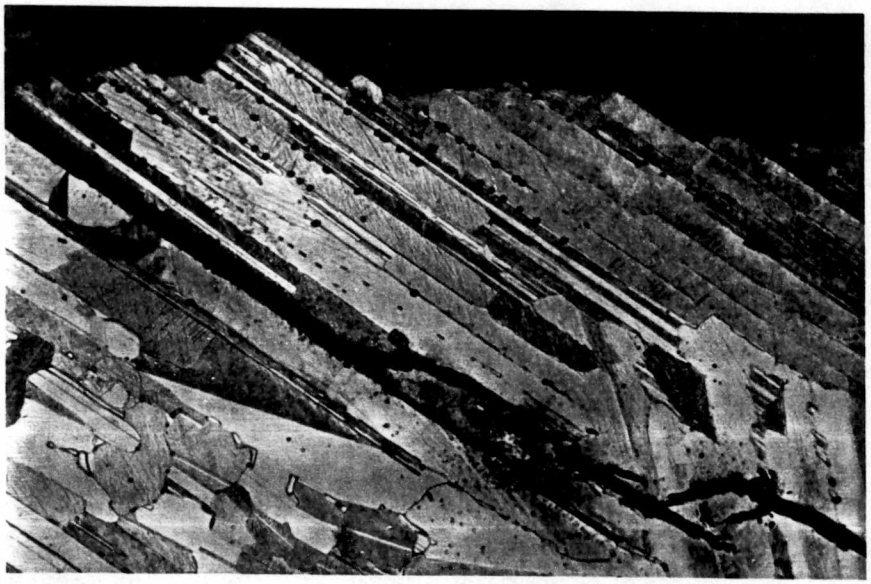
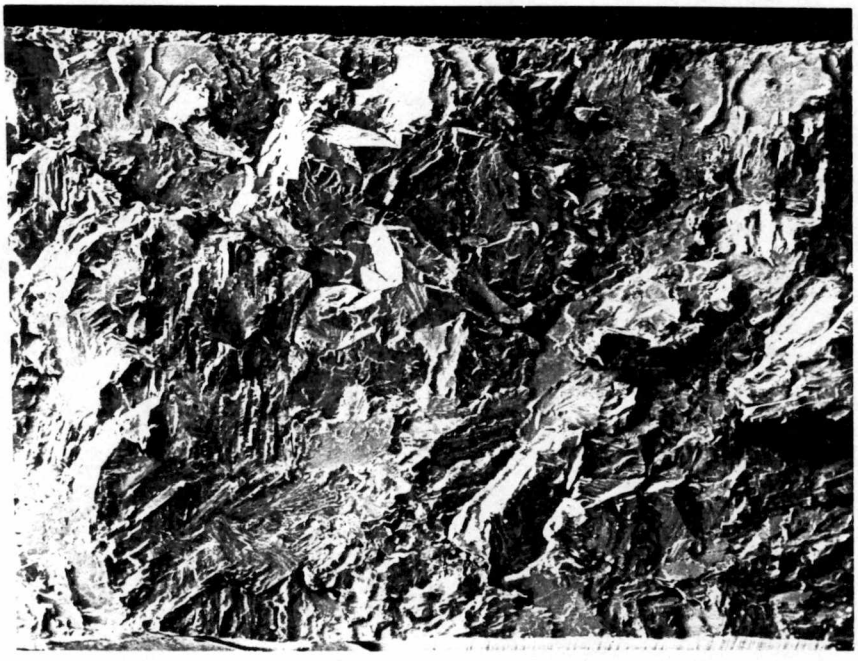


Figure 29. Optical Microstructure of Zone Processed and Homogenized Ti-50/Al-50. a) Showing Fracture Edge and Crack Propagation Behavior b) Showing Fracture Edge and Interlamellar Separation, Etched.



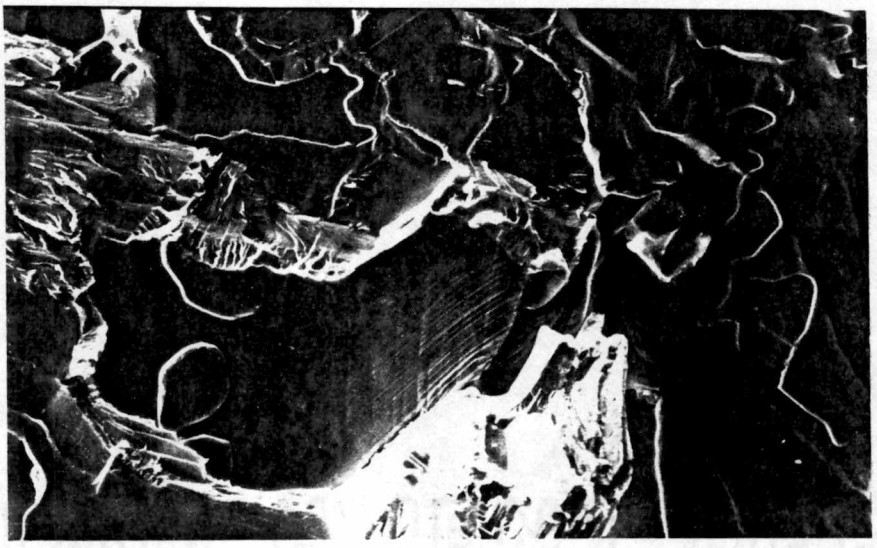
a)
1 mm

Tension Side

Figure 30. SEM Fractographs of Zone Processed and Homogenized Ti-50/Al-50. a) Low Magnification Showing Both Tension and Compression Sides b) Shows Possible Slip Traces and Deformation Twins c) Higher Magnification of Region in b d) Shows Lamellar Separation Near Casting Pore e) Shows Casting Pore with Growth Facets Inside.

b)

25 μm



c)

10 μm

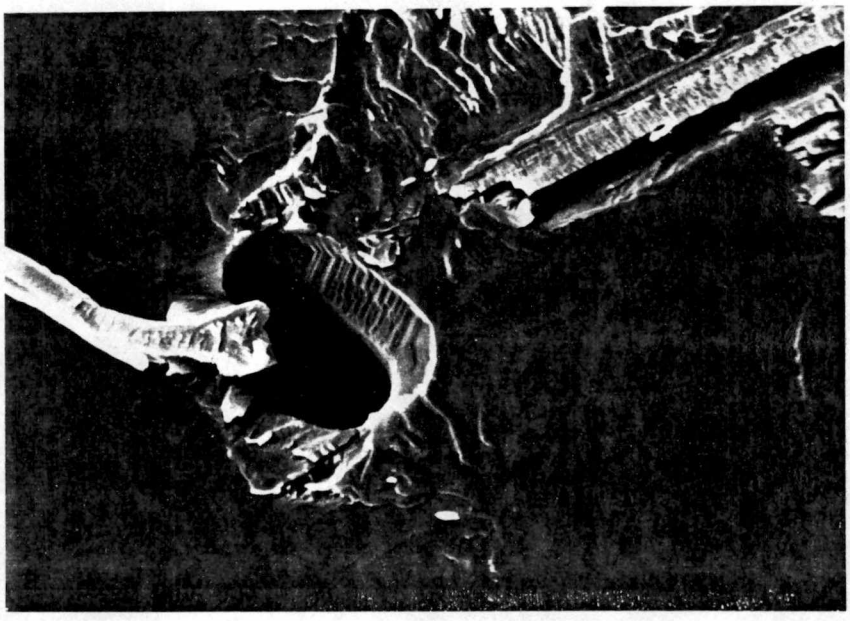


Tension Side

Figure 30. Continued.

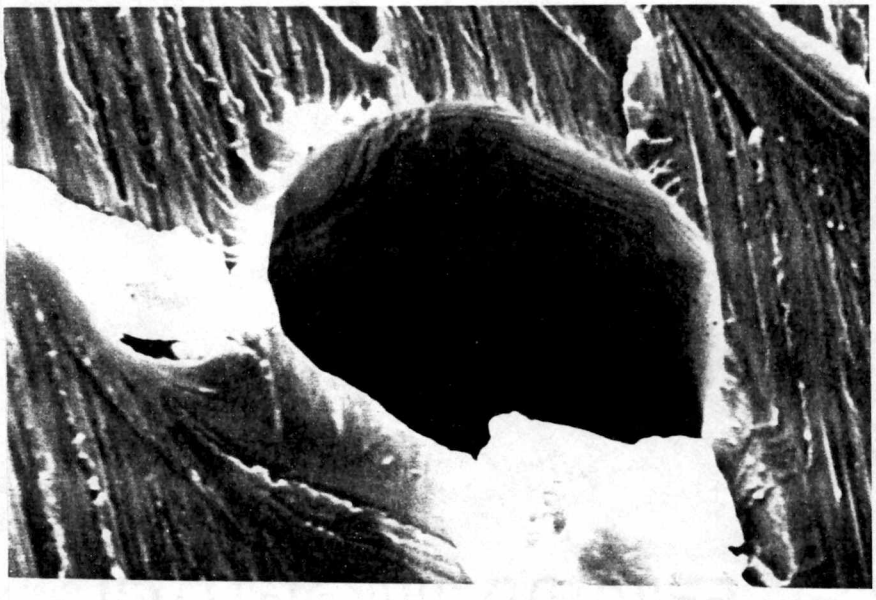
d)

10 μm



e)

5 μm



Tension Side

Figure 30. Continued.

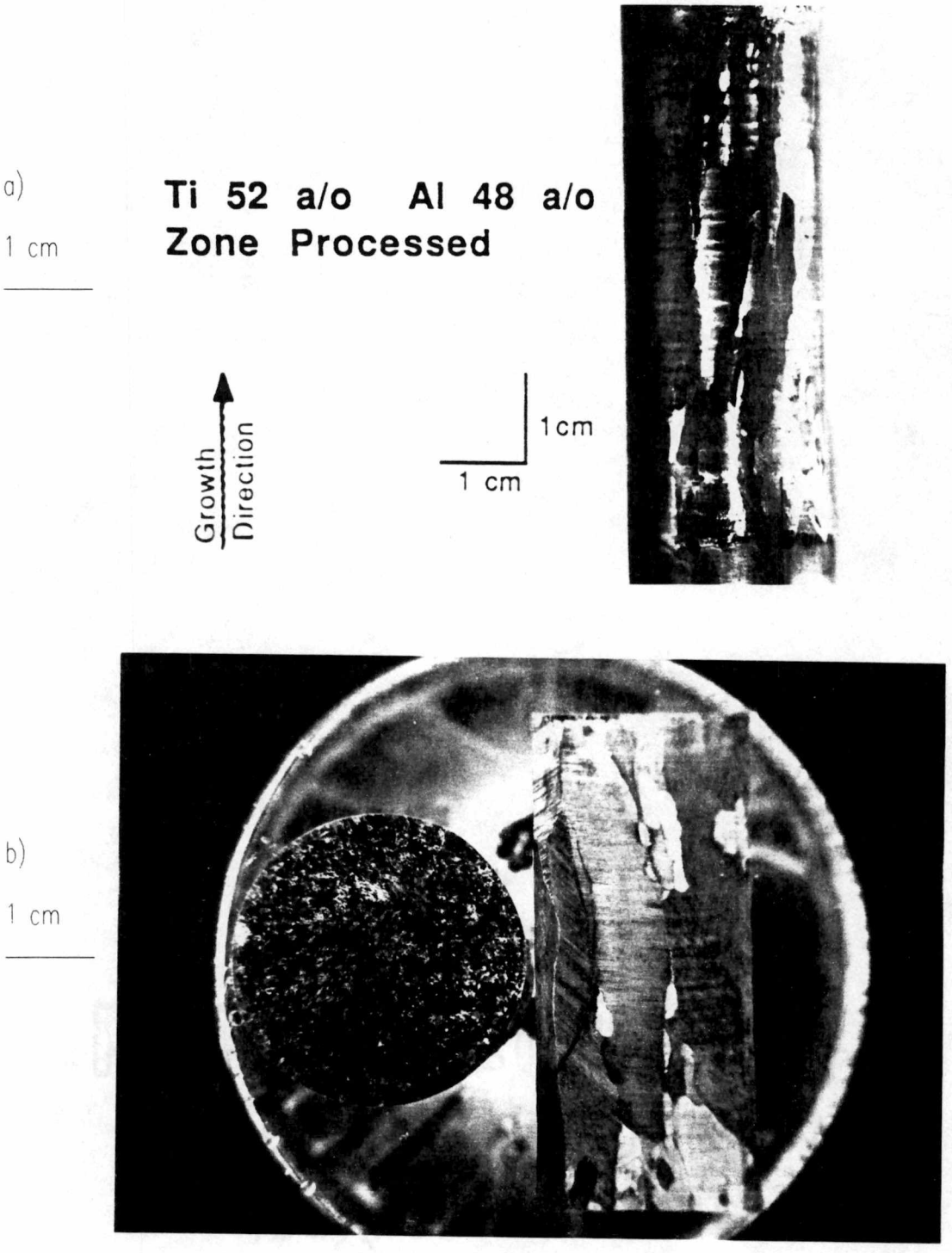


Figure 31. Macro of Zone Melted Ti-52/Al-48. a) Exterior of ingot b) Transverse and Longitudinal Section, Etched. Growth Direction from Bottom to Top of Photograph.

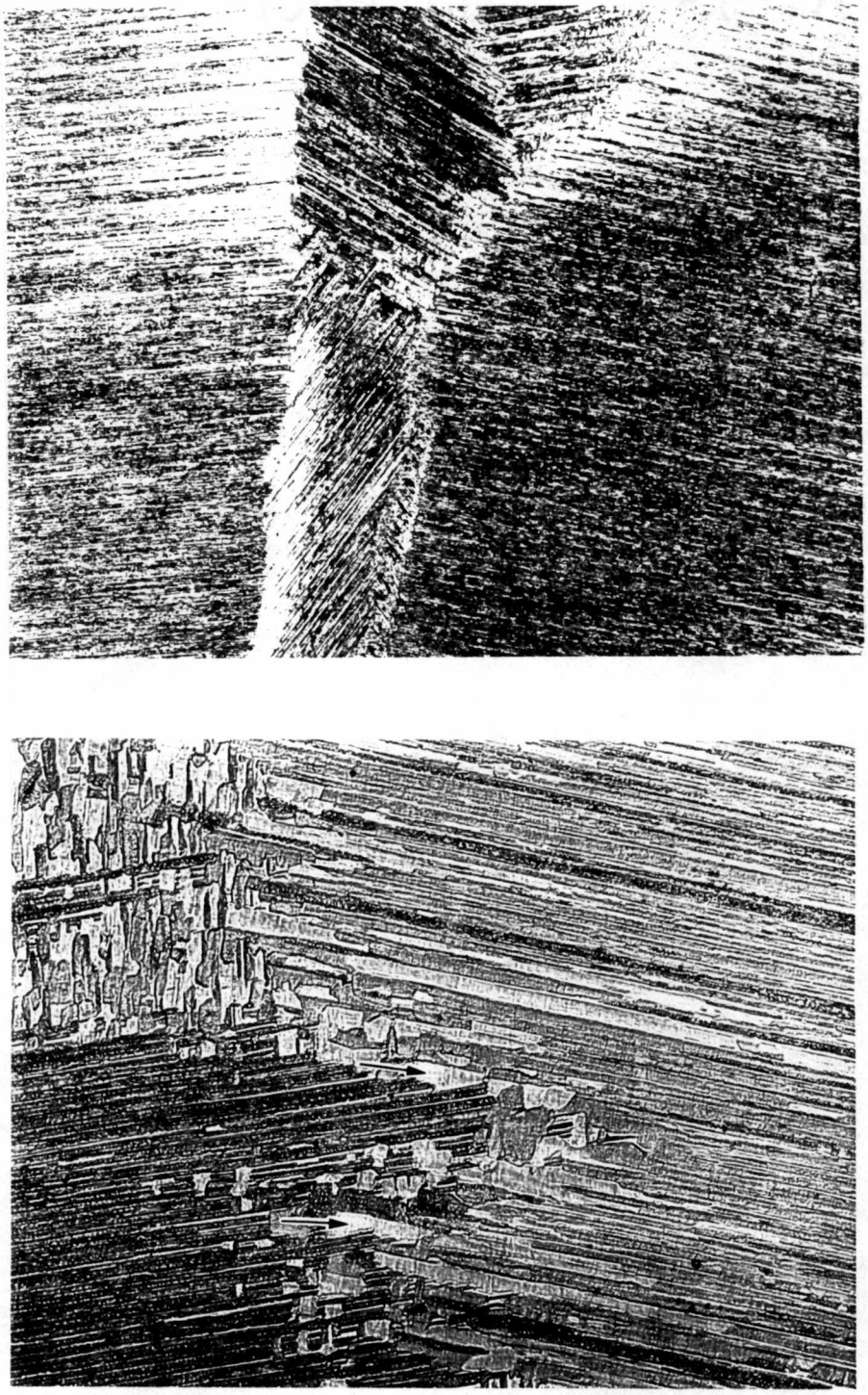


Figure 32. Microstructure of Zone Processed Ti-52/Al-48. a) Shows Lamellar Colonies, Etched b) Shows Proeutectoid γ at Prior α Boundaries, Etched. Growth Direction from Bottom to Top of Photographs. Arrows in b) Point to Blocky γ.

a)

50 μm

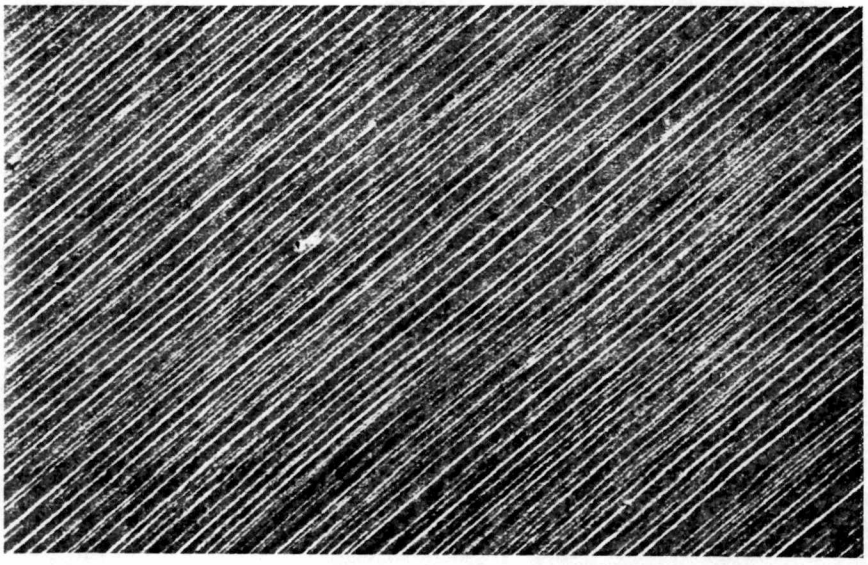
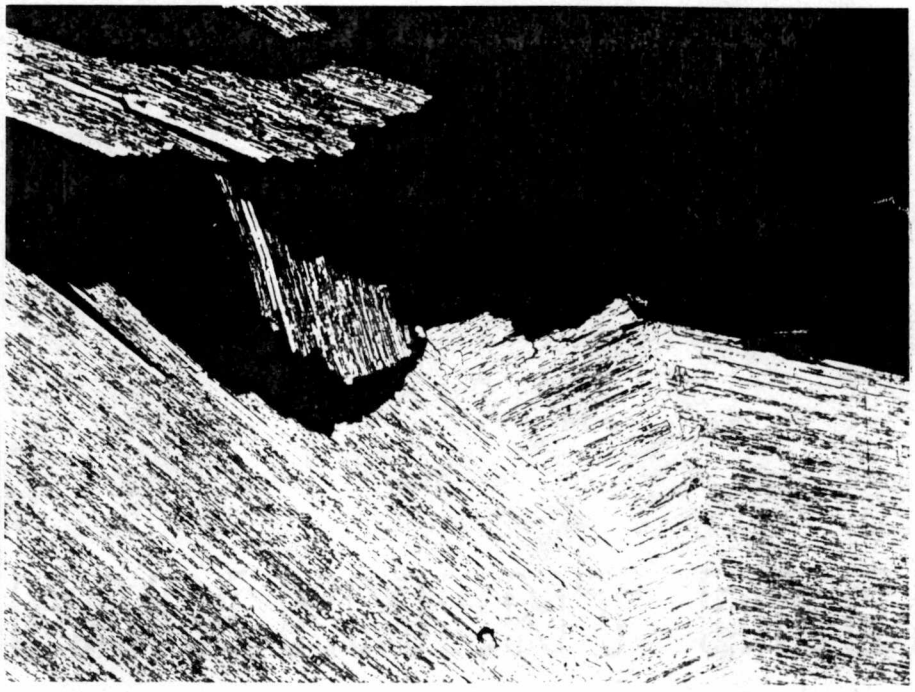


Figure 33. Homogenized Microstructure of Zone Processed Ti-52/Al-48. a) SEM Backscattered Image Showing Fine $\alpha 2$ b) Optical Microstructure Showing Fracture Edge and Crack Propagation Behavior, Etched c) Optical Microstructure Showing Fracture Edge and Interlamellar Separation, Etched.

b)

250 μm



c)

50 μm

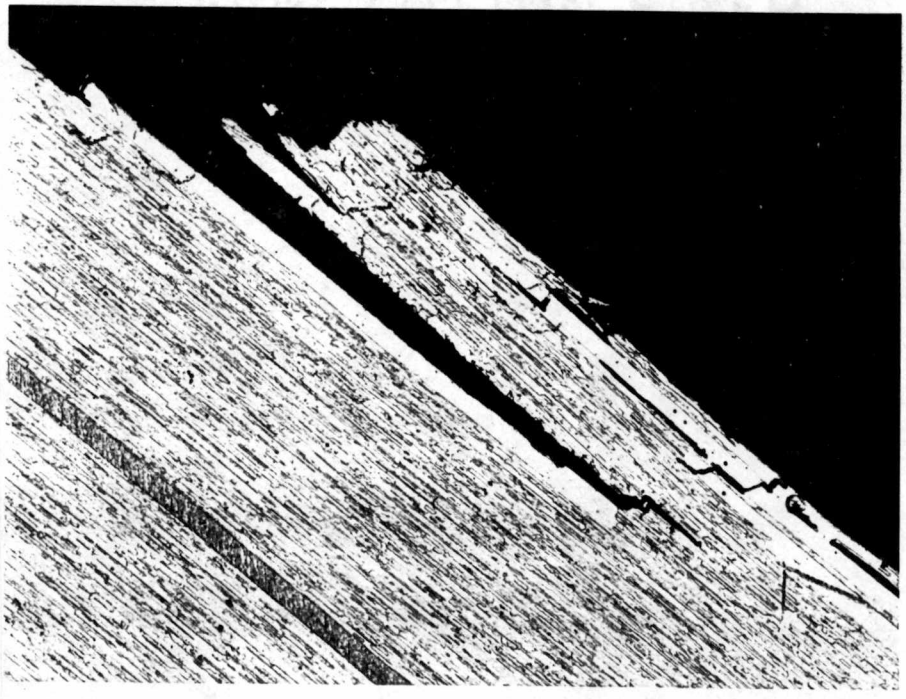


Figure 33. Continued.

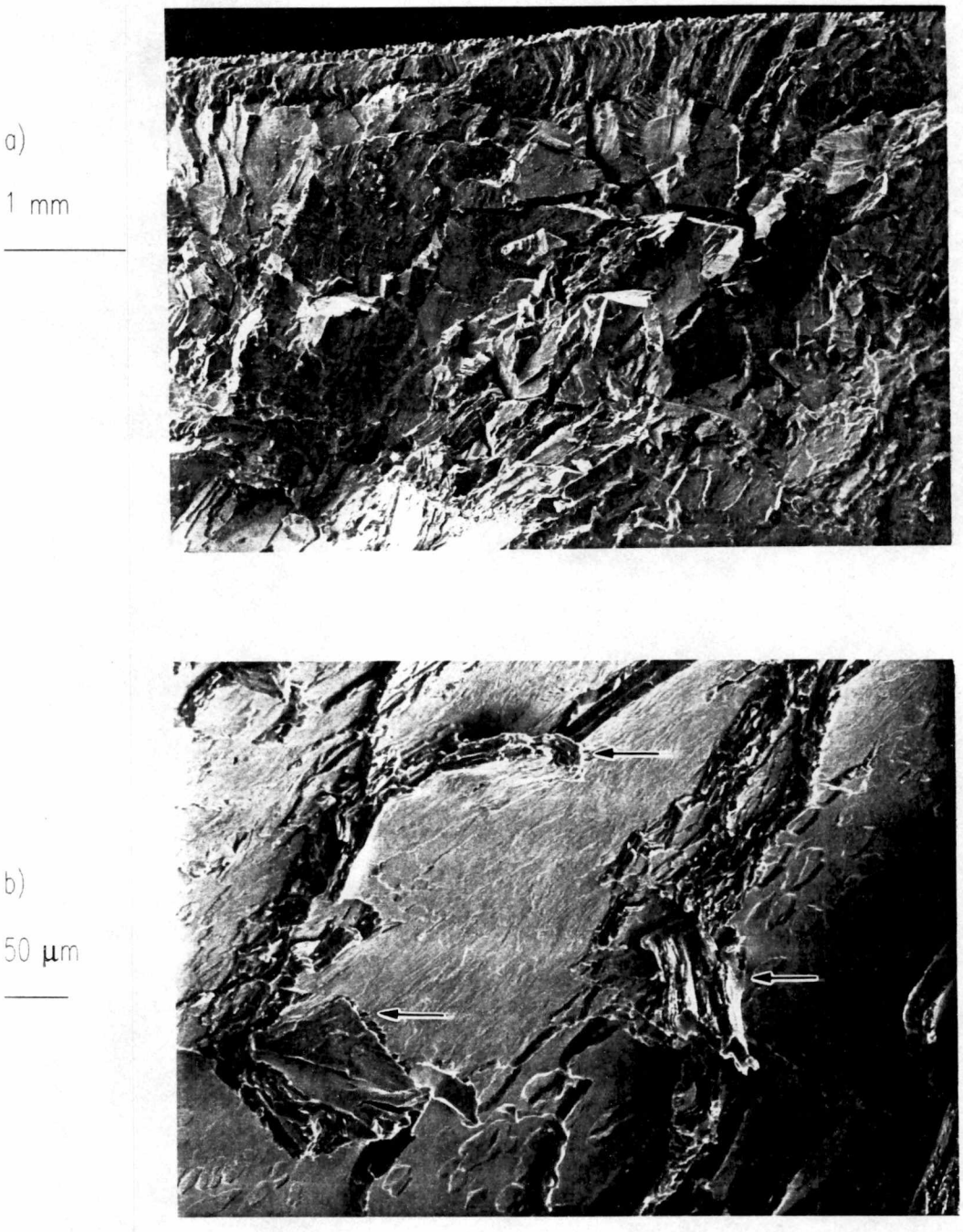


Figure 34. SEM Fractographs of Zoned Processed and Homogenized Ti-52/Al-48. a) Low Magnification Showing Both Tension and Compression Sides b) Shows interlamellar Separation. Arrows Point to Bent Lamellae.

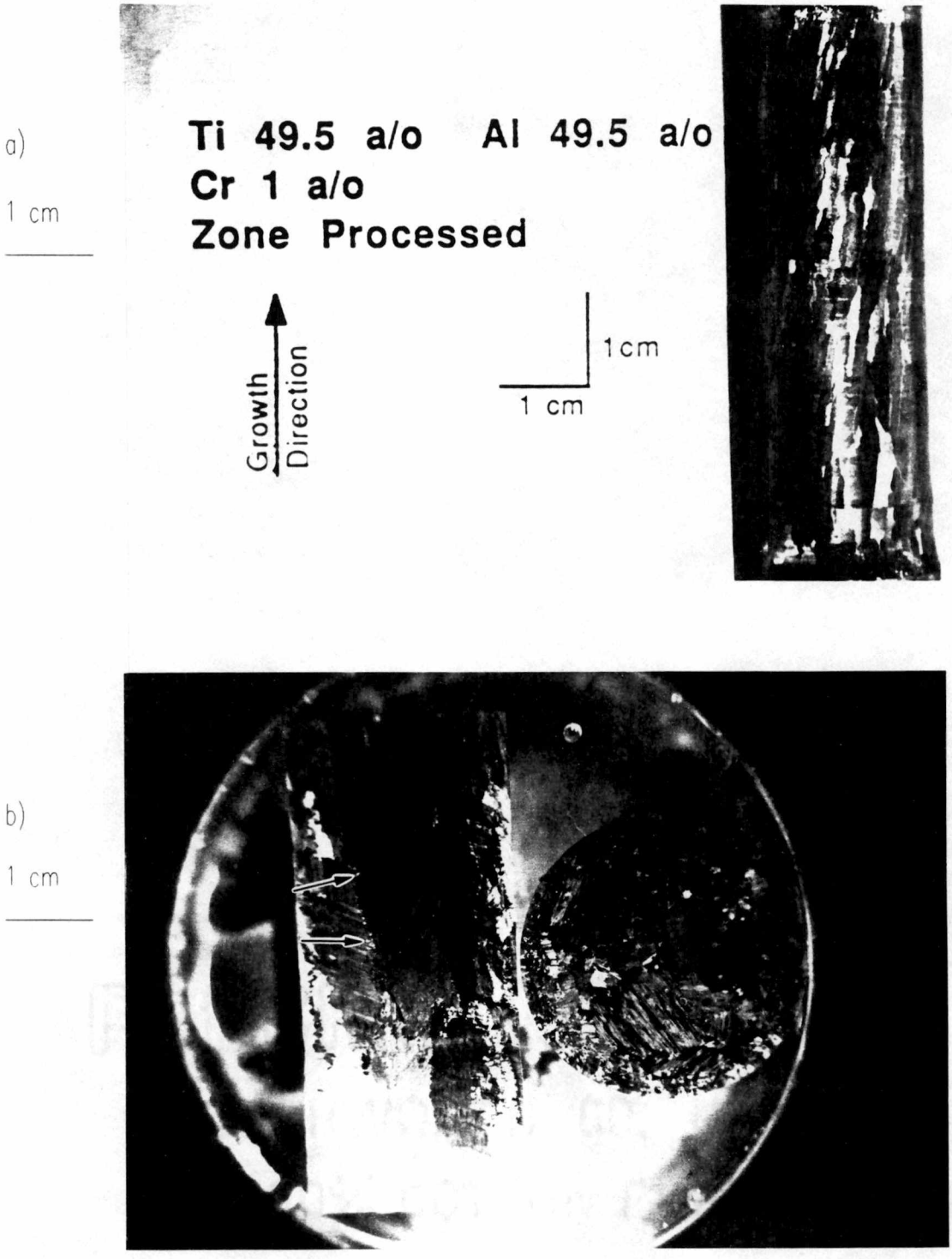
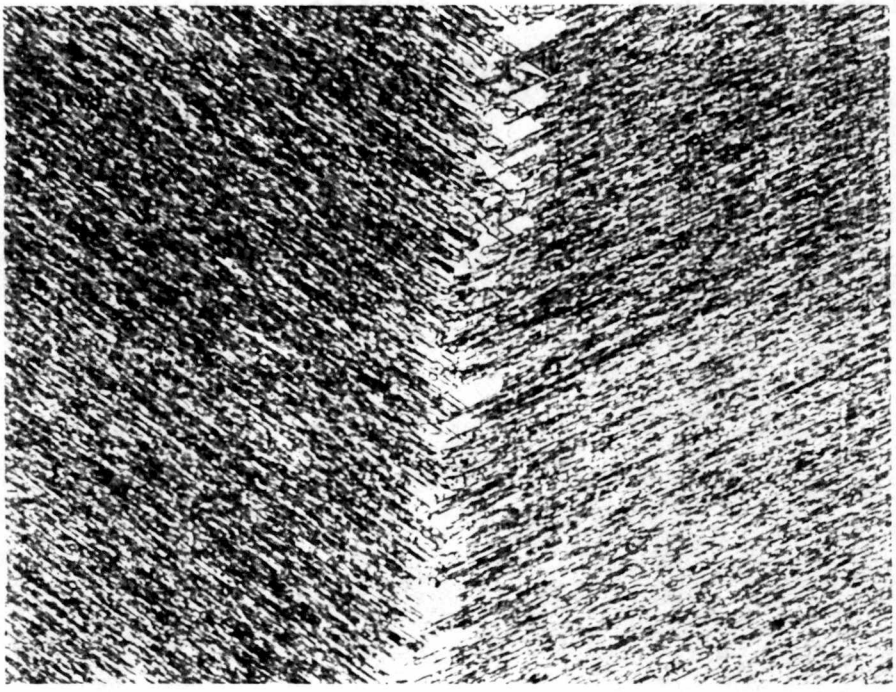


Figure 35. Zone Melted Ti-49.5/Al-49.5/Cr-1. a) Macro of Exterior of ingot b) Macro of Transverse and Longitudinal Section, Etched. c) Optical Microstructure Showing Lamellar Colonies, Etched d) Optical Microstructure Showing Proeutectoid γ at Prior α Boundaries, Etched. Growth Direction from Bottom to Top of Photographs. Arrows in b) Point to Blocky γ.

c)

250 μm



d)

50 μm

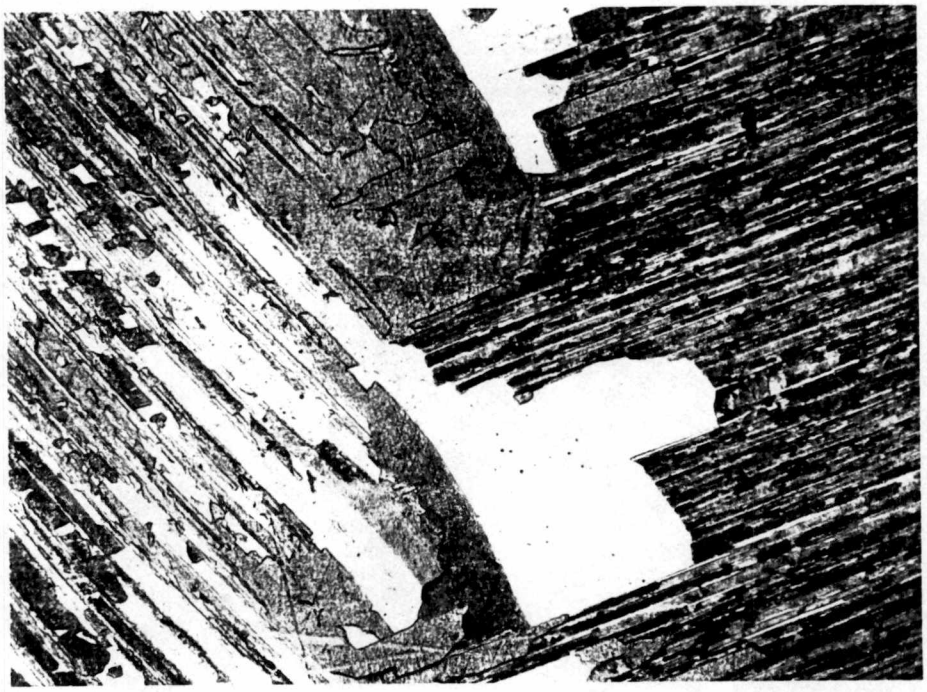
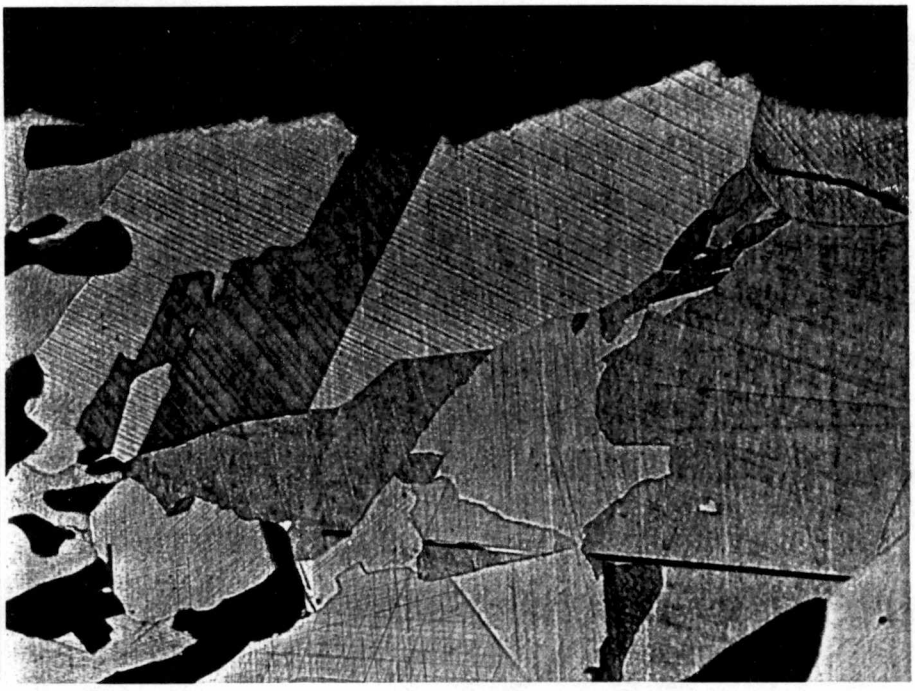


Figure 35. Continued.

a)

250 μm



b)

50 μm

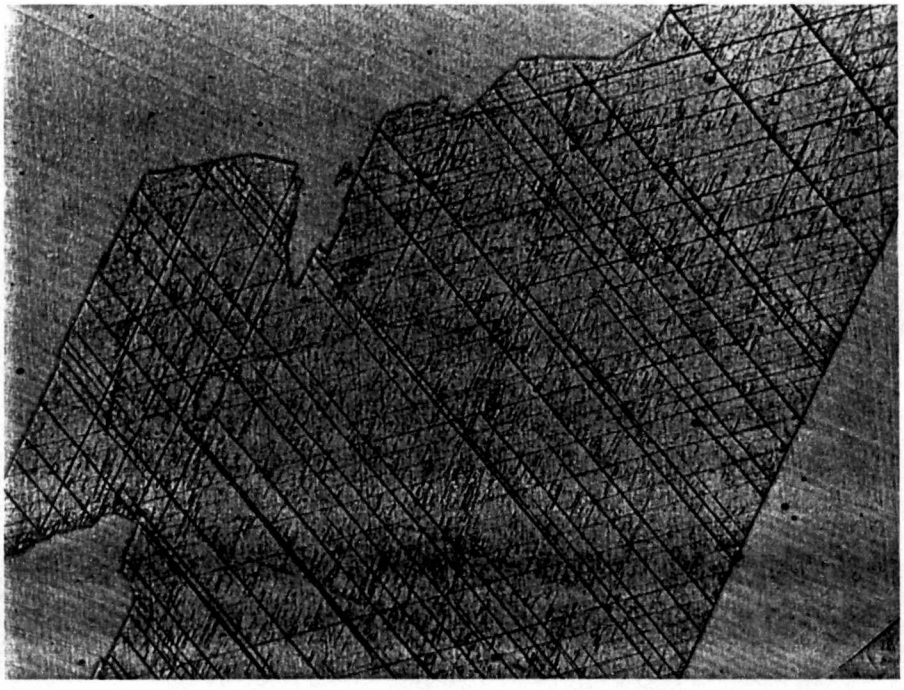


Figure 36. Homogenized Microstructure of Zone Processed Ti-49.5/Al-49.5/Cr-1 a) Optical Microstructure Showing Fracture Edge, Etched b) Optical Microstructure Showing Fracture Edge and Deformation Twins, Higher magnification of a), Etched. c) SEM Backscattered Image Showing $\alpha 2$ Based Second Phase at Grain Boundaries.

c)

100 μm

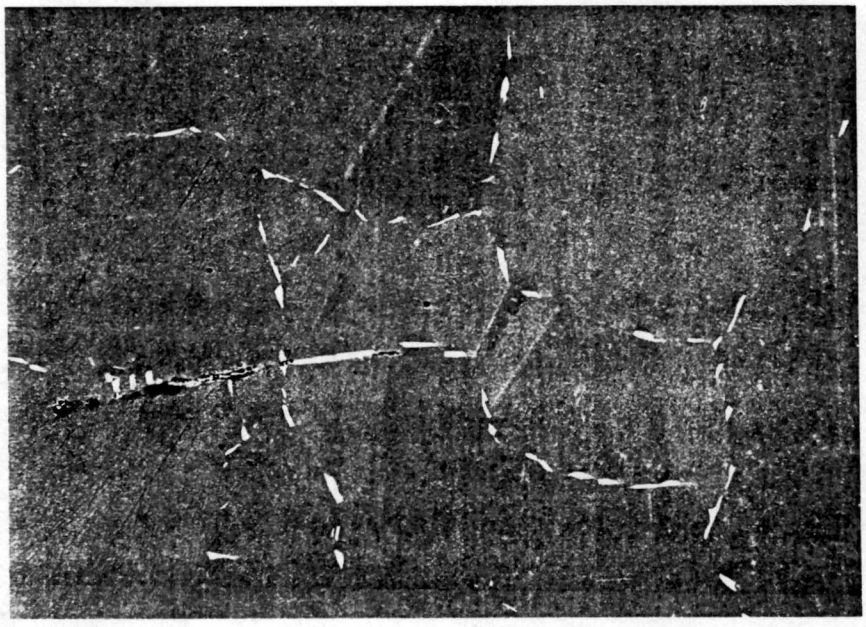
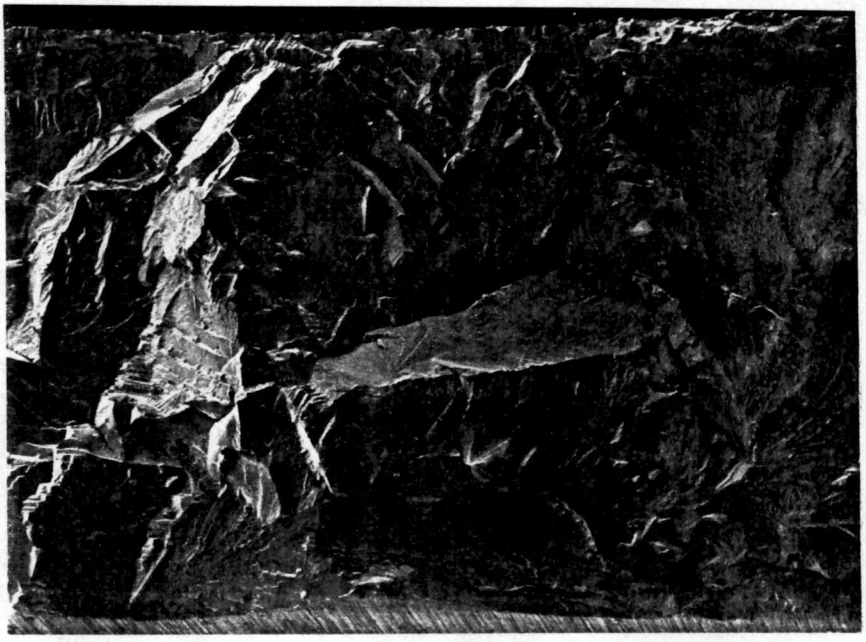


Figure 36. Continued.

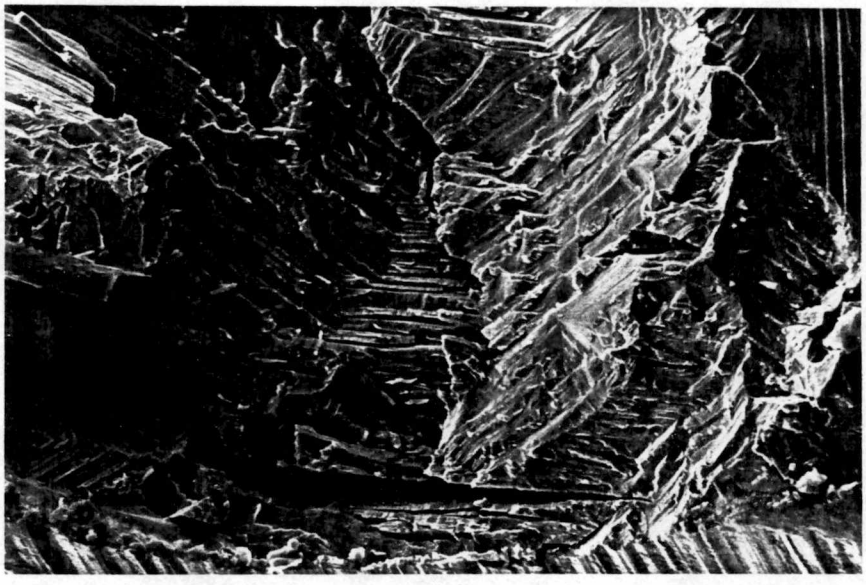
a)

1 mm



b)

50 μm



Tension Side

Figure 37. SEM Fractographs of Zoned Processed and Homogenized Ti-49.5/Al-49.5/Cr-1. a) Low Magnification Showing Both Tension and Compression Sides b) Shows Higher Magnification of Cleavage Facet.

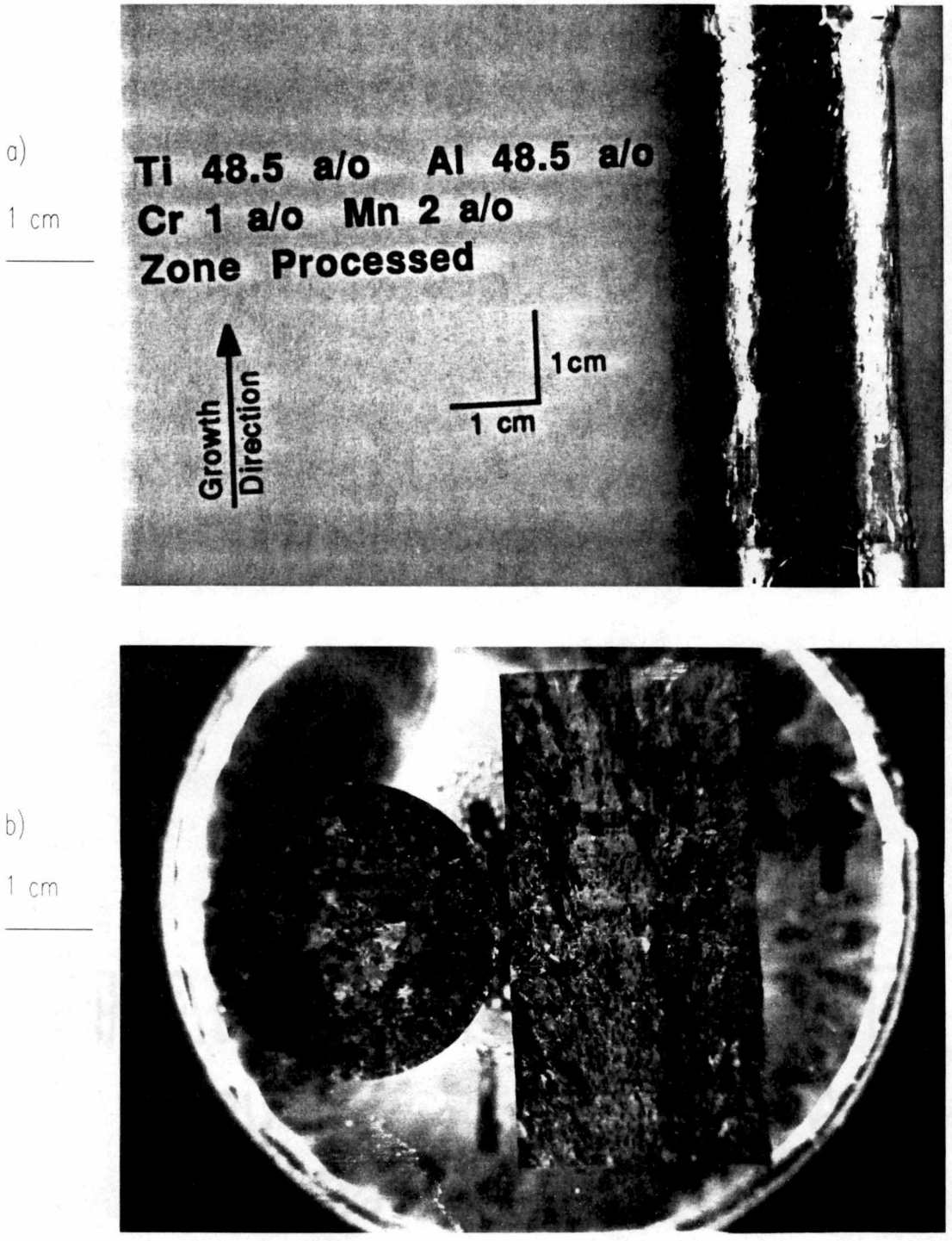


Figure 38. Macro of Zone Melted Ti-48.5/Al-48.5/Cr-1/Mn-2. a) Exterior of ingot b) Transverse and Longitudinal Section, Etched. Growth Direction from Bottom to Top of Photographs.



Figure 39. Microstructure of Zone Processed Ti-48.5/Al-48.5/Cr-1/Mn-2. Showing Lamellar Colonies and Proeutectoid γ at Prior α Boundaries, Etched. Growth Direction from Bottom to Top of Photographs

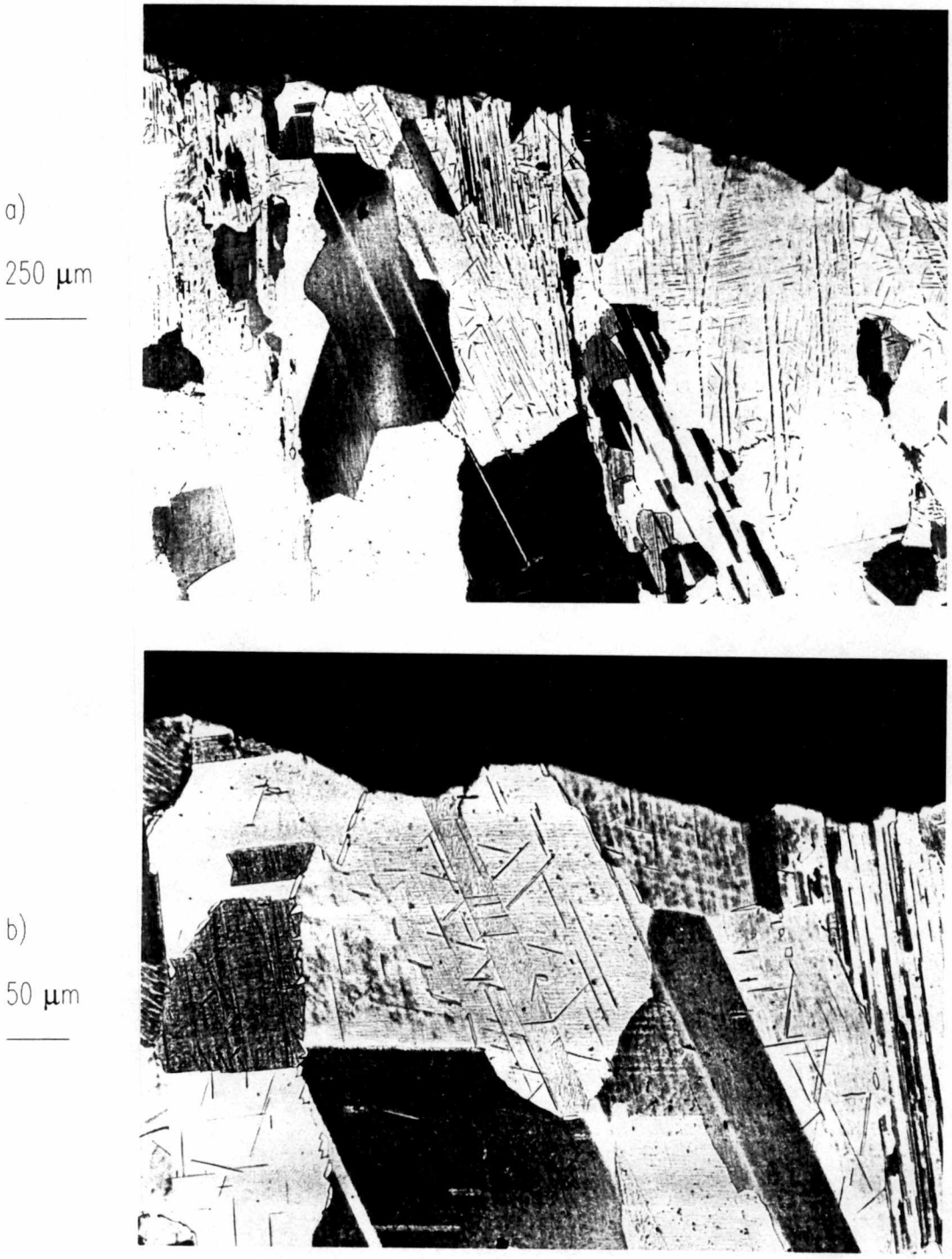


Figure 40. Homogenized Microstructure of Zone Processed Ti-48.5/Al-48.5/Cr-1/Mn-2 a) Optical Microstructure Showing Fracture Edge, Etched b) Optical Microstructure Showing Fracture Edge and Deformation Twins, Etched. c) SEM Backscattered Image Showing $\alpha 2$ at Grain Boundaries and Twins Inside Grains.

c)

50 μm

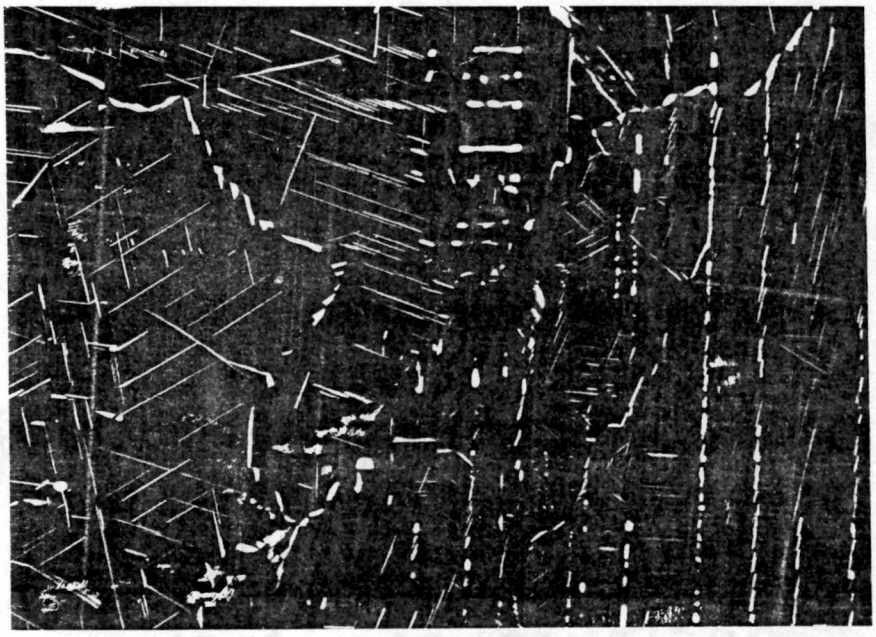
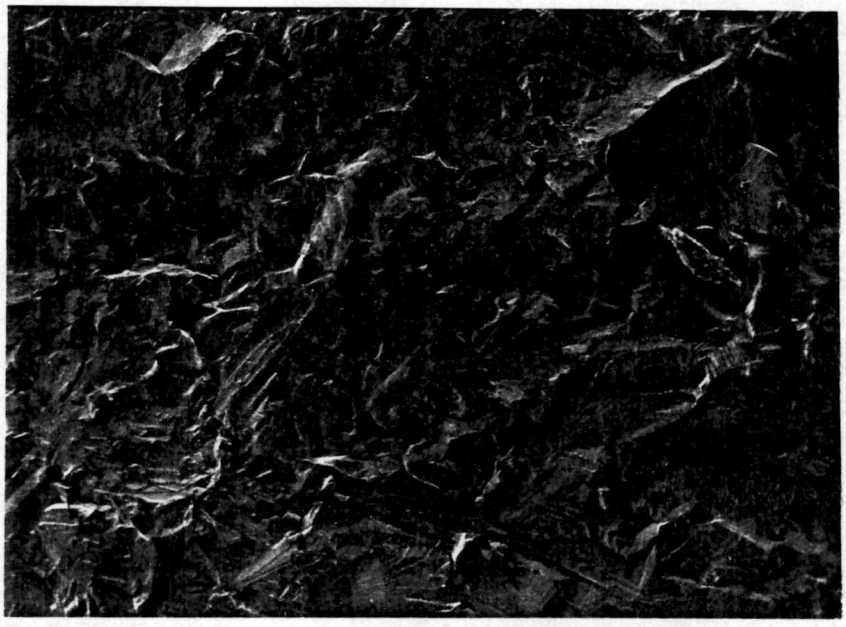


Figure 40. Continued.

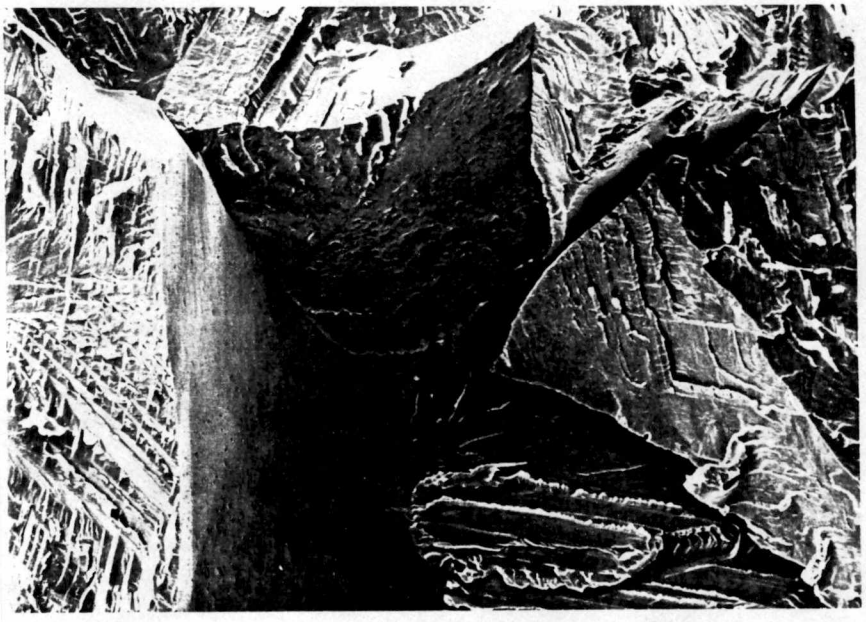
a)

1 mm



b)

50 μm



Tension Side

Figure 41. SEM Fractographs of Zoned Processed and Homogenized Ti-48.5/Al-48.5/Cr-1/Mn-2. a) Low Magnification Showing Both Tension and Compression Sides b) Shows Higher Magnification of Intergranular Fracture region.

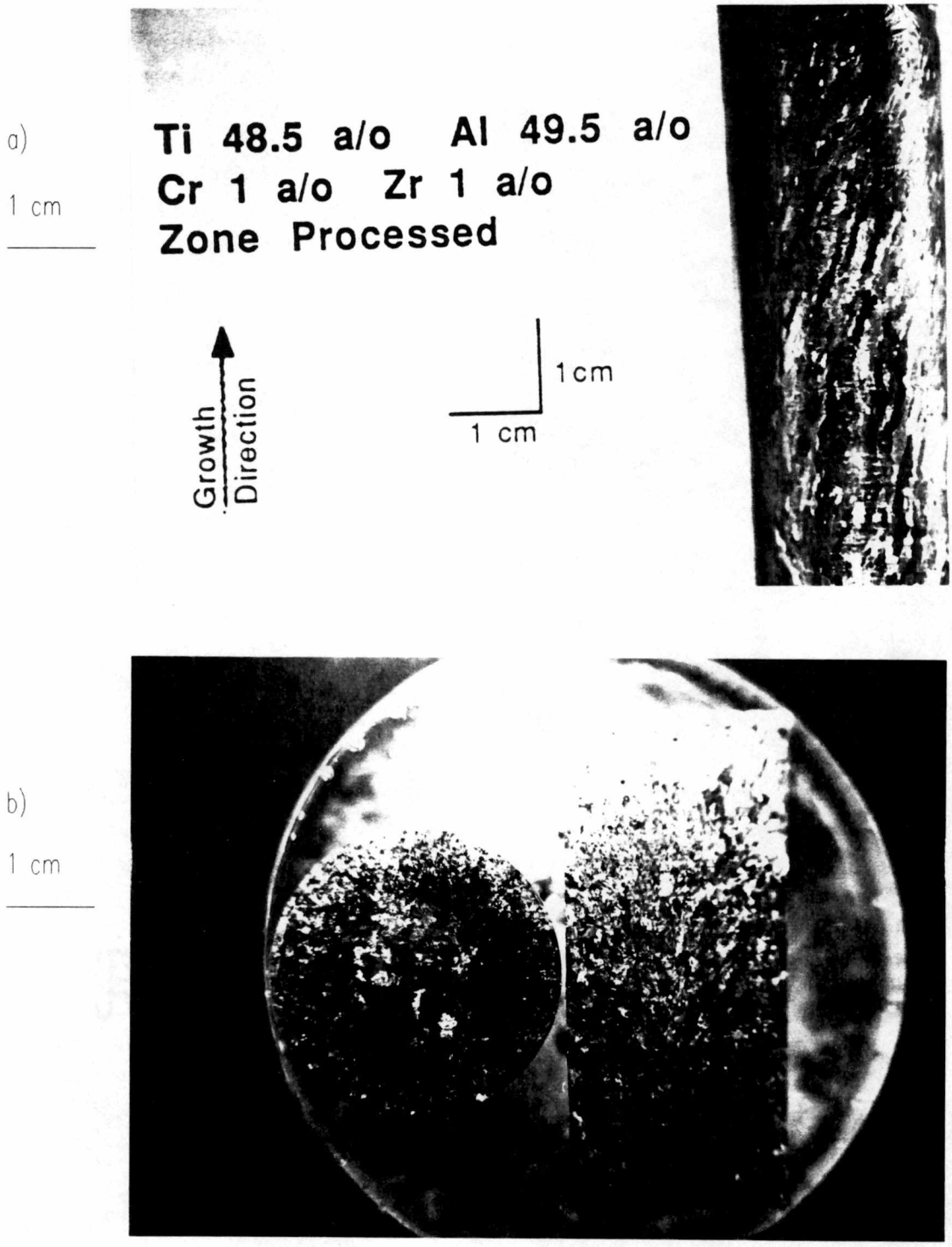


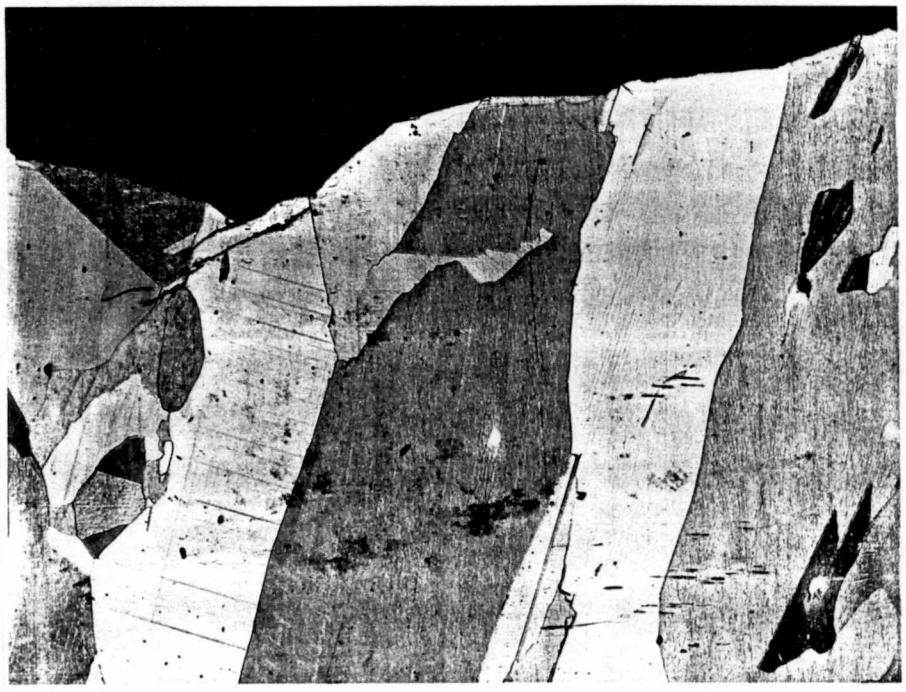
Figure 42. Macro of Zone Melted Ti-48.5/Al-49.5/Cr-1/Zr-1. a) Exterior of Ingot b) Transverse and Longitudinal Section, Etched. Growth Direction from Bottom to Top of Photographs.



Figure 43. Microstructure of Zone Processed Ti-48.5/Al-49.5/Cr-1/Zr-1. Showing Lamellar Colonies and Proeutectoid γ at Prior α Boundaries, Etched. Growth Direction from Bottom to Top of Photographs

a)

250 μm



b)

50 μm

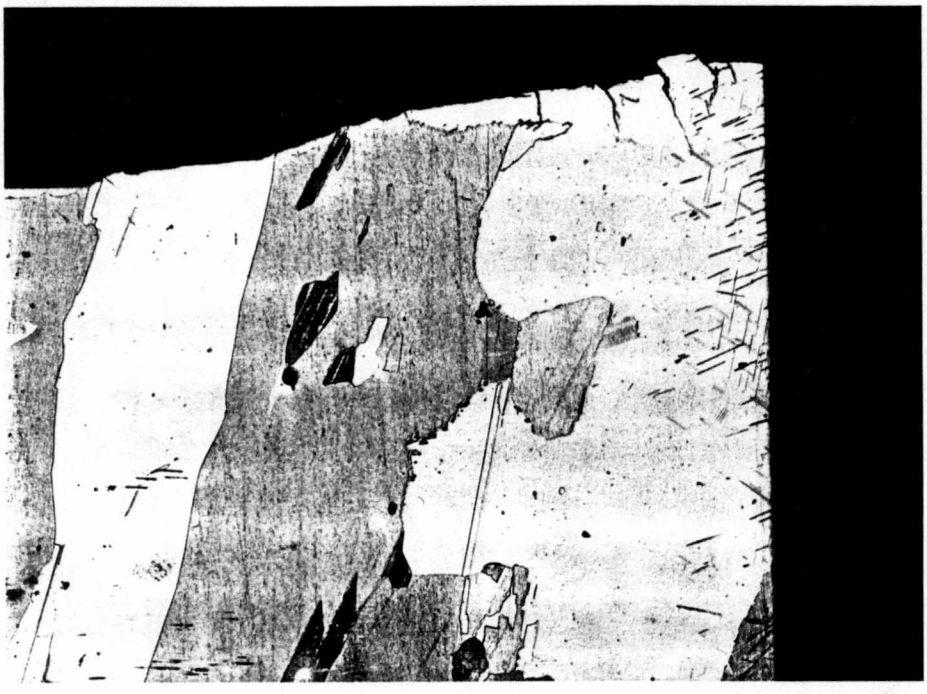


Figure 44. Homogenized Microstructure of Zone Processed Ti-48.5/Al-49.5/Cr-1/ Zr-1 a) Optical Microstructure Showing Fracture Edge, Etched b) Optical Microstructure Showing Fracture Edge and Deformation Twins, Etched. c) SEM Backscattered Image Showing $\alpha 2$ at Grain Boundaries.

c)

50 μm

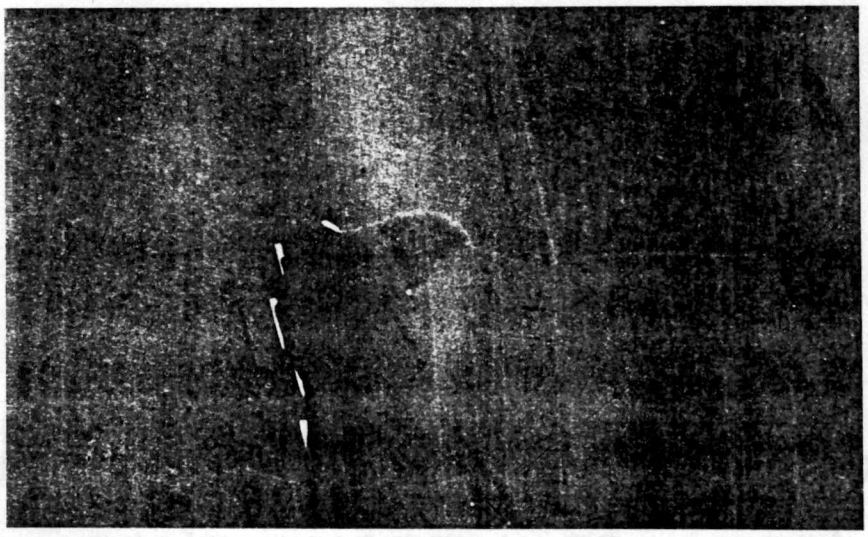
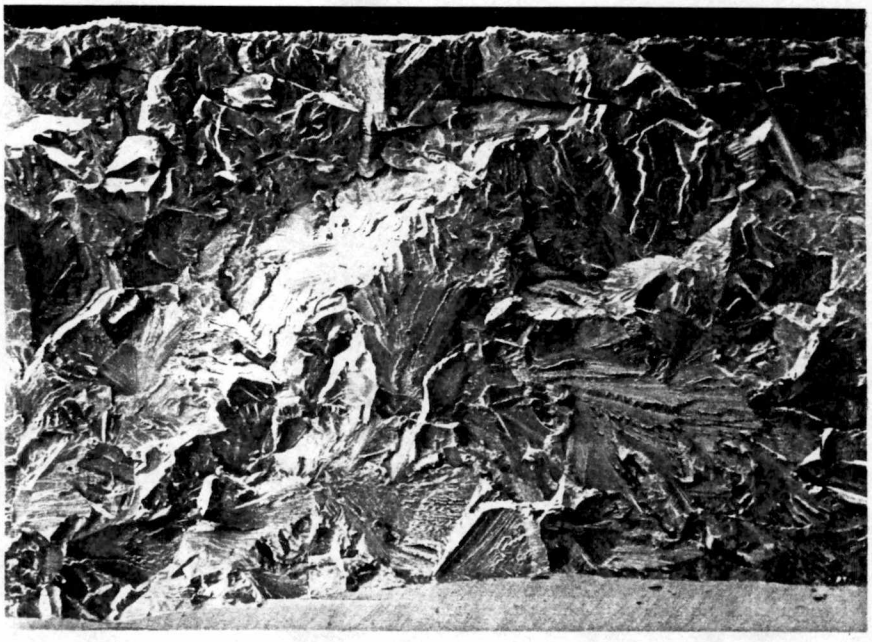


Figure 44. Continued.

a)

1 mm

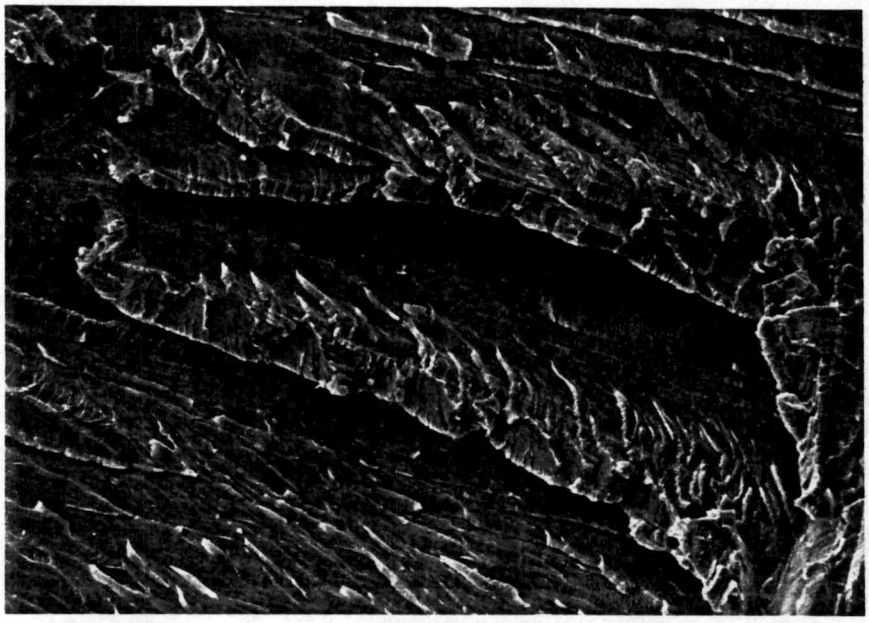


Tension Side

Figure 45. SEM Fractographs of Zoned Processed and Homogenized Ti-48.5/Al-49.5/Cr-1/Zr-1. a) Low Magnification Showing Both Tension and Compression Sides b) Shows Higher Magnification of Cleavage Facet c) Higher Magnification of b Showing Possible Slip Traces or Deformation Twins.

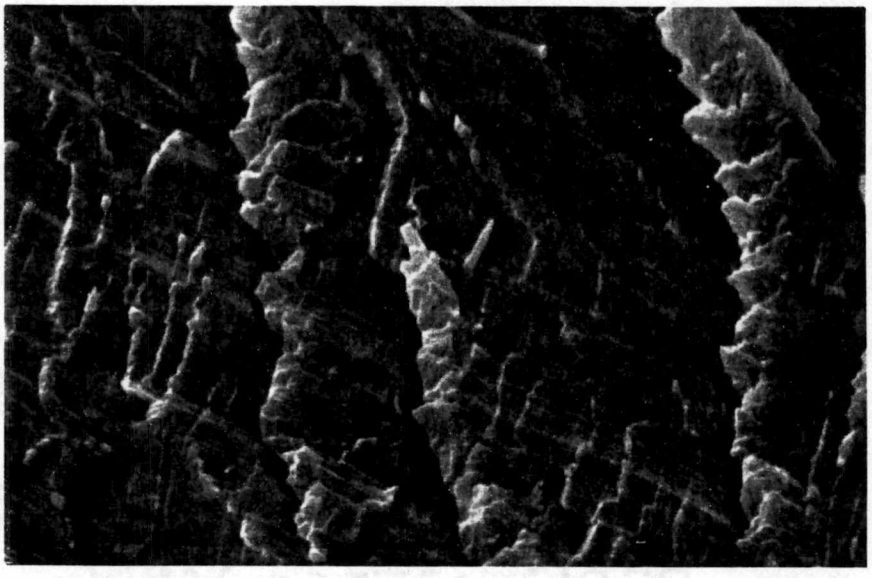
b)

50 μm



c)

5 μm



Tension Side

Figure 45. Continued.

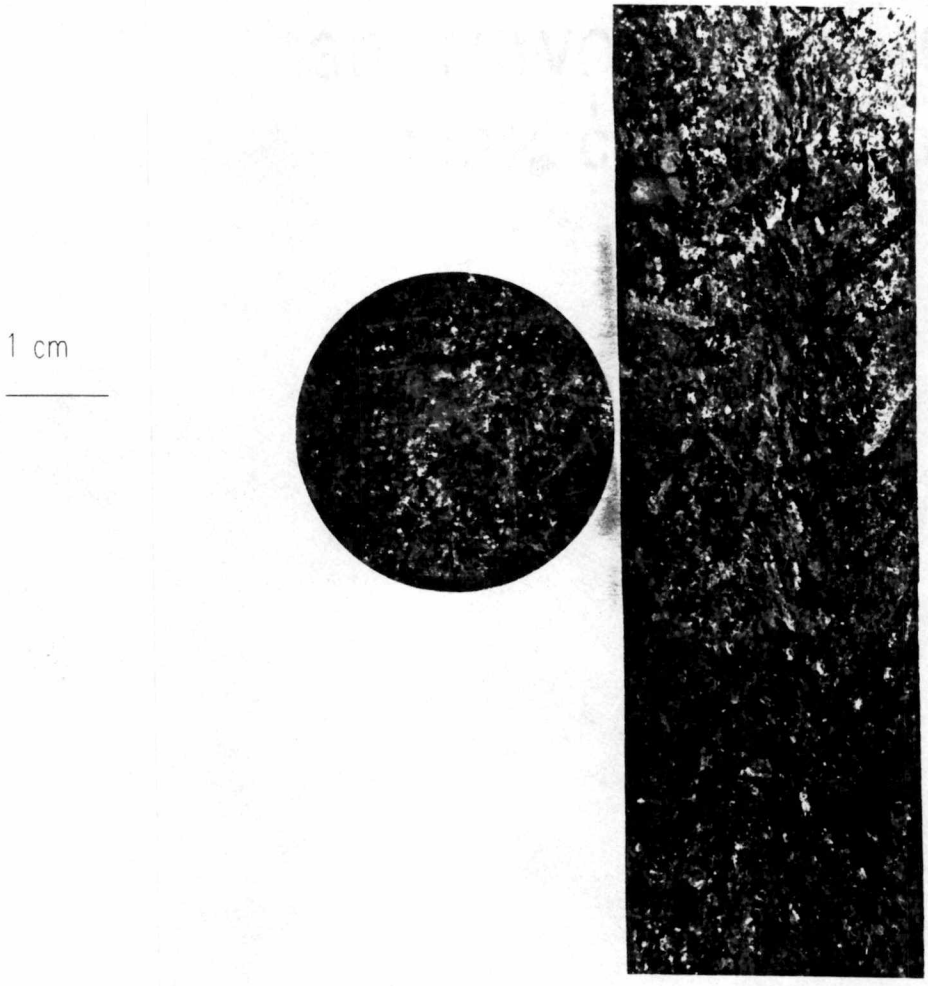


Figure 46. Macro of Zone Melted Ti-48/Al-48/Ga-2/Mn-2 Transverse and Longitudinal Section, Etched. Growth Direction from Bottom to Top of Photographs.



Figure 47. Microstructure of Zone Processed Ti-48/Al-48/Ga-2/Mn-2. Showing Lamellar Colonies and γ (TiAl) grains, Etched. Growth Direction from Bottom to Top of Photographs.

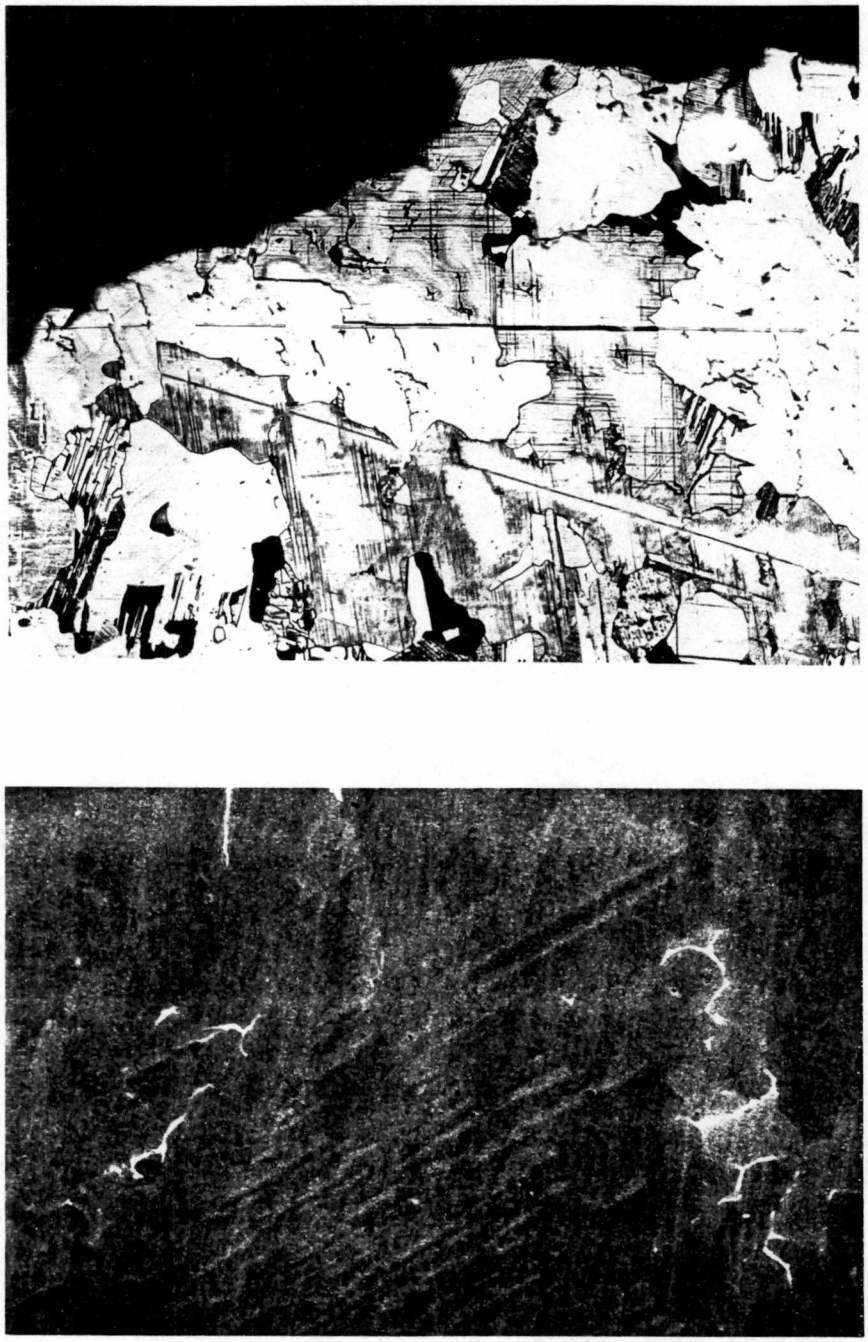


Figure 48. Homogenized Microstructure of Zone Processed Ti-48/Al-48/Ga-2/Mn-2 a) Optical Microstructure Showing Fracture Edge, Etched b) SEM Backscattered Image Showing $\alpha 2$ at Grain Boundaries c) Optical Microstructure Showing Fracture Edge and Crack Propagation Direction, Etched.

c)

50 μm



Figure 48. Continued.

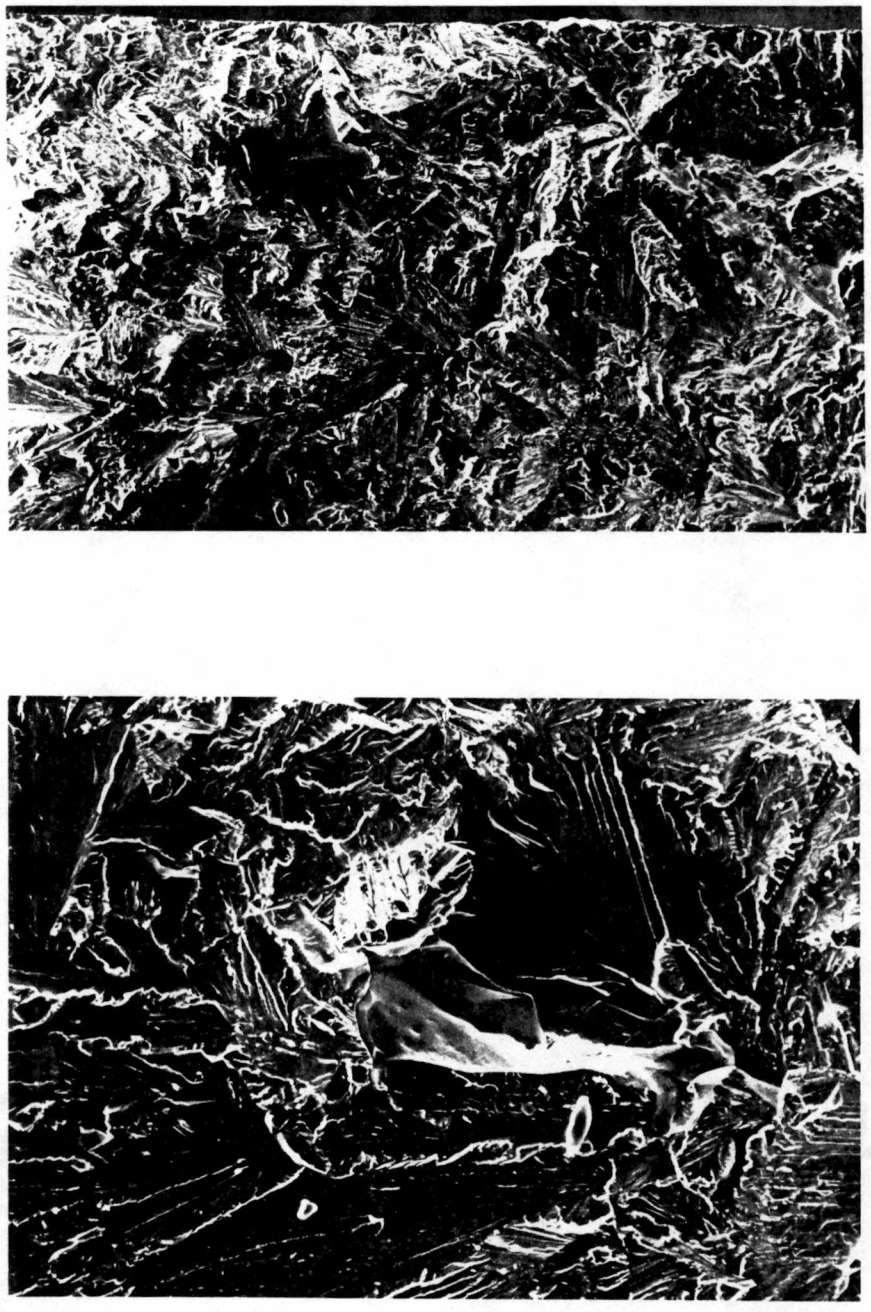


Figure 49. SEM Fractographs of Zoned Processed and Homogenized Ti-48/Al-48/Ga-2/ Mn-2. a) Low Magnification Showing Both Tension and Compression Sides b) Shows Higher Magnification of Intergranular Fracture Region.

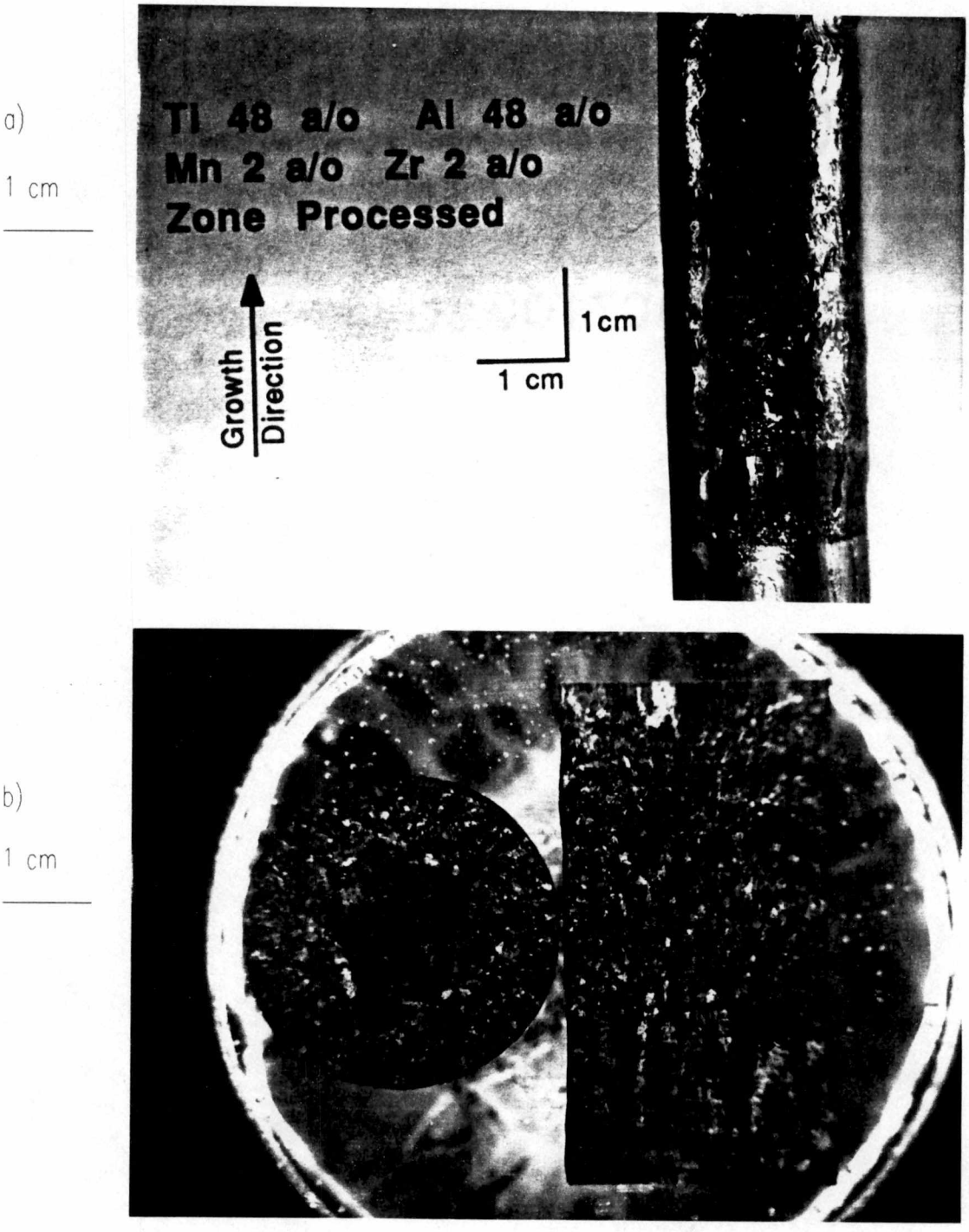


Figure 50. Zone Melted Ti-48/Al-48/Mn-2/Zr-2. a) Macro of Exterior of Ingot b) Macro of Transverse and Longitudinal Section, Etched. c) Optical Micrograph Showing Lamellar Structure and Proeutectoid γ at Prior α Boundaries, Etched. Growth Direction from Bottom to Top of Photographs

c)

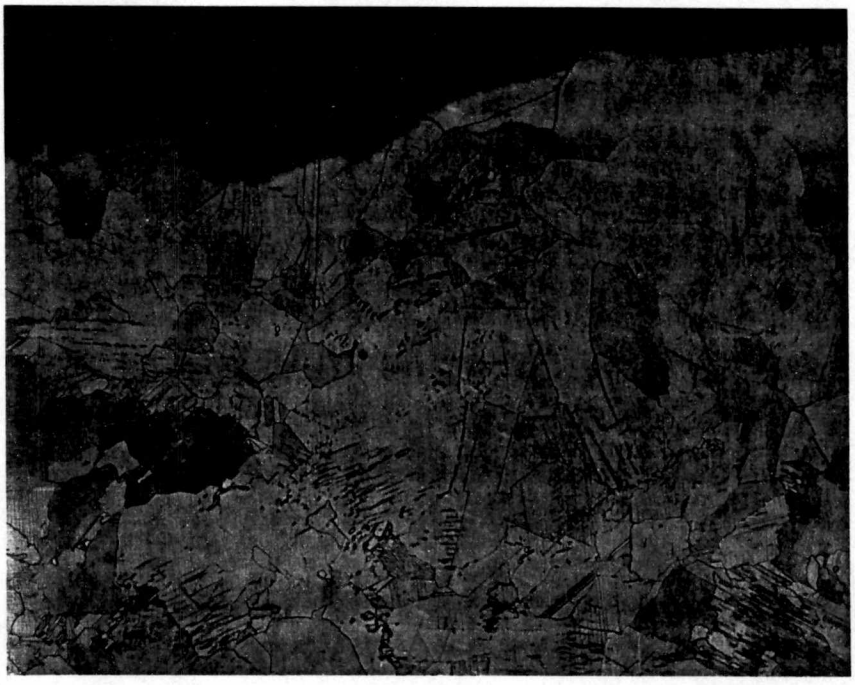
250 μm



Figure 50. Continued

a)

250 μm



b)

250 μm

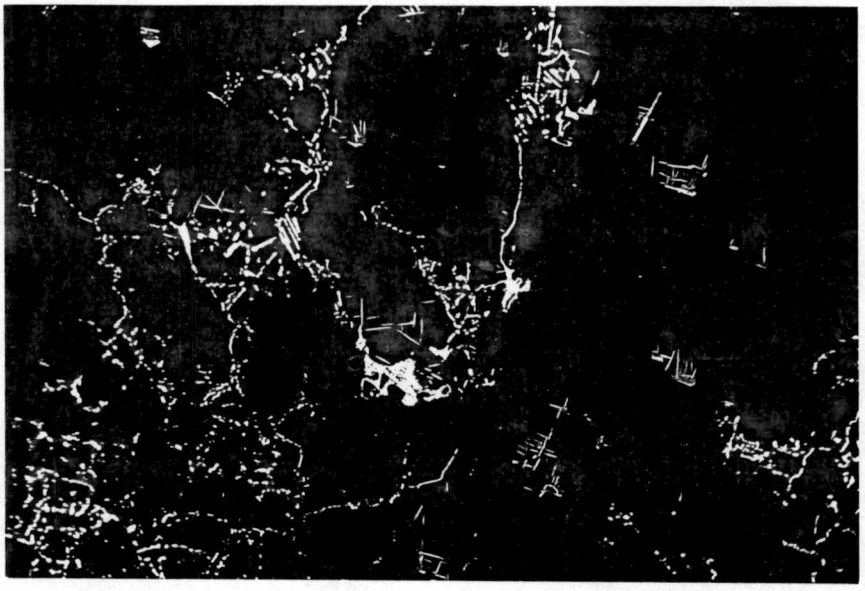


Figure 51. Homogenized Microstructure of Zone Processed Ti-48/Al-48/Mn-2/Zr-2 a) Optical Microstructure Showing Fracture Edge, Etched b) SEM Backscattered Image Showing $\alpha 2$ (Gray Phase) and a Cu Rich Phase (White Phase) at the Grain Boundaries c) Optical Microstructure Showing Fracture Edge and Crack Propagation Direction, Etched.

c)

50 μm

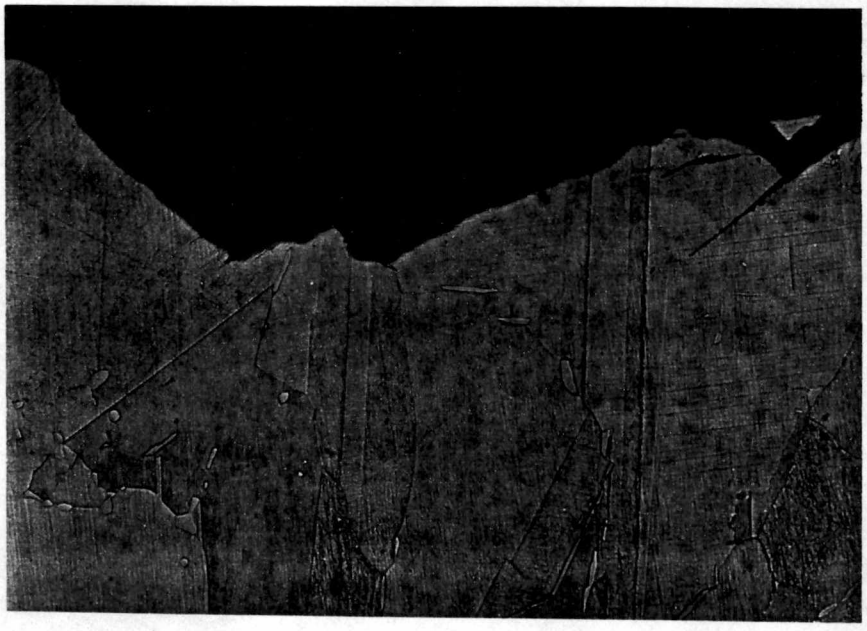


Figure 51. Continued.

a)

1 mm



b)

50 µm



Tension Side

Figure 52. SEM Fractographs of Zoned Processed and Homogenized Ti-48/Al-48/Mn-2/ Zr-2. a) Low Magnification Showing Both Tension and Compression Sides b) Shows Intergranular Fracture Region and a Large Cleavage Facet.

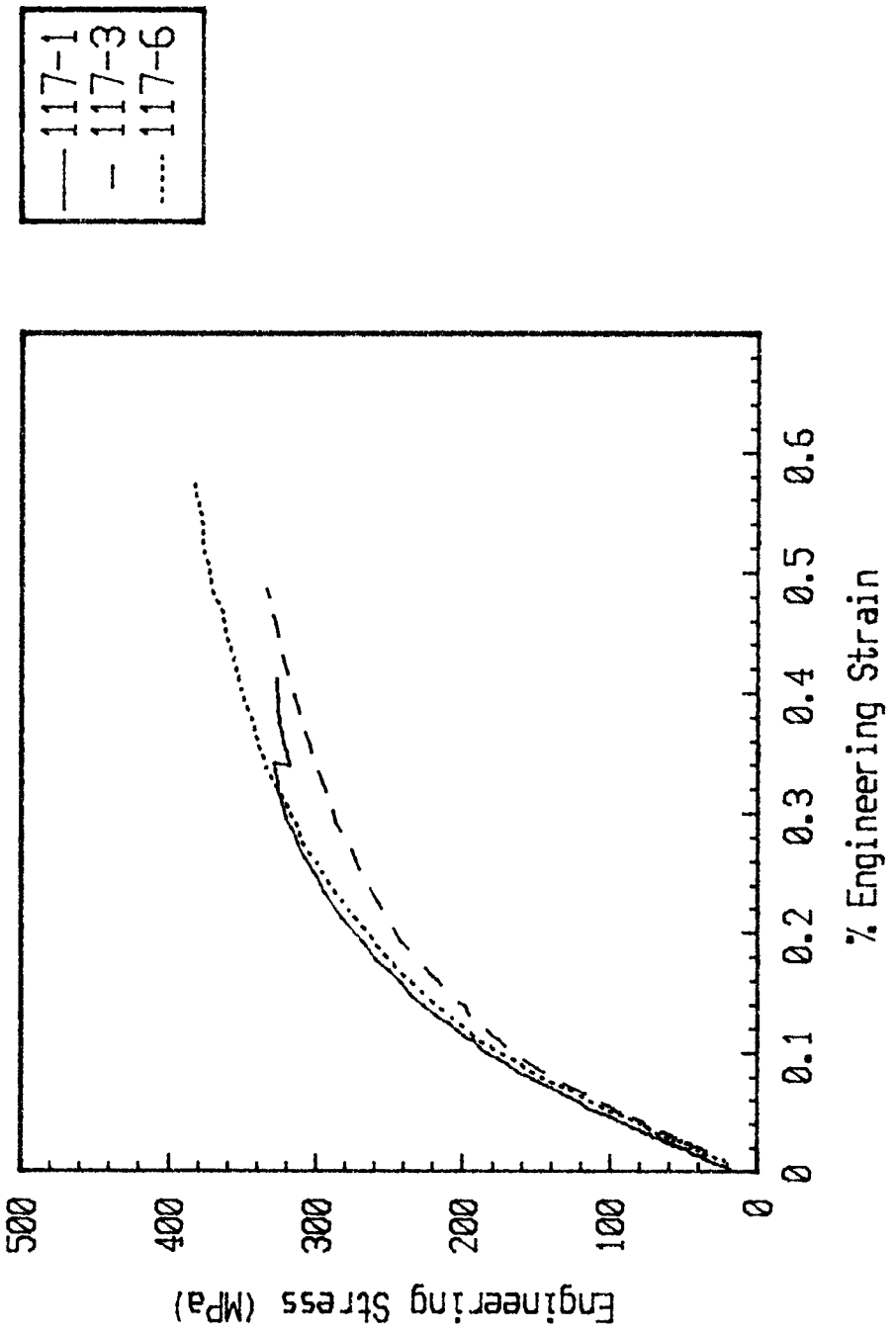


Figure 53. Engineering Stress (MPa) versus Percent Engineering Strain for Four Point Bending of Ti-50/Al-50. Strain Measured via Strain Gages.

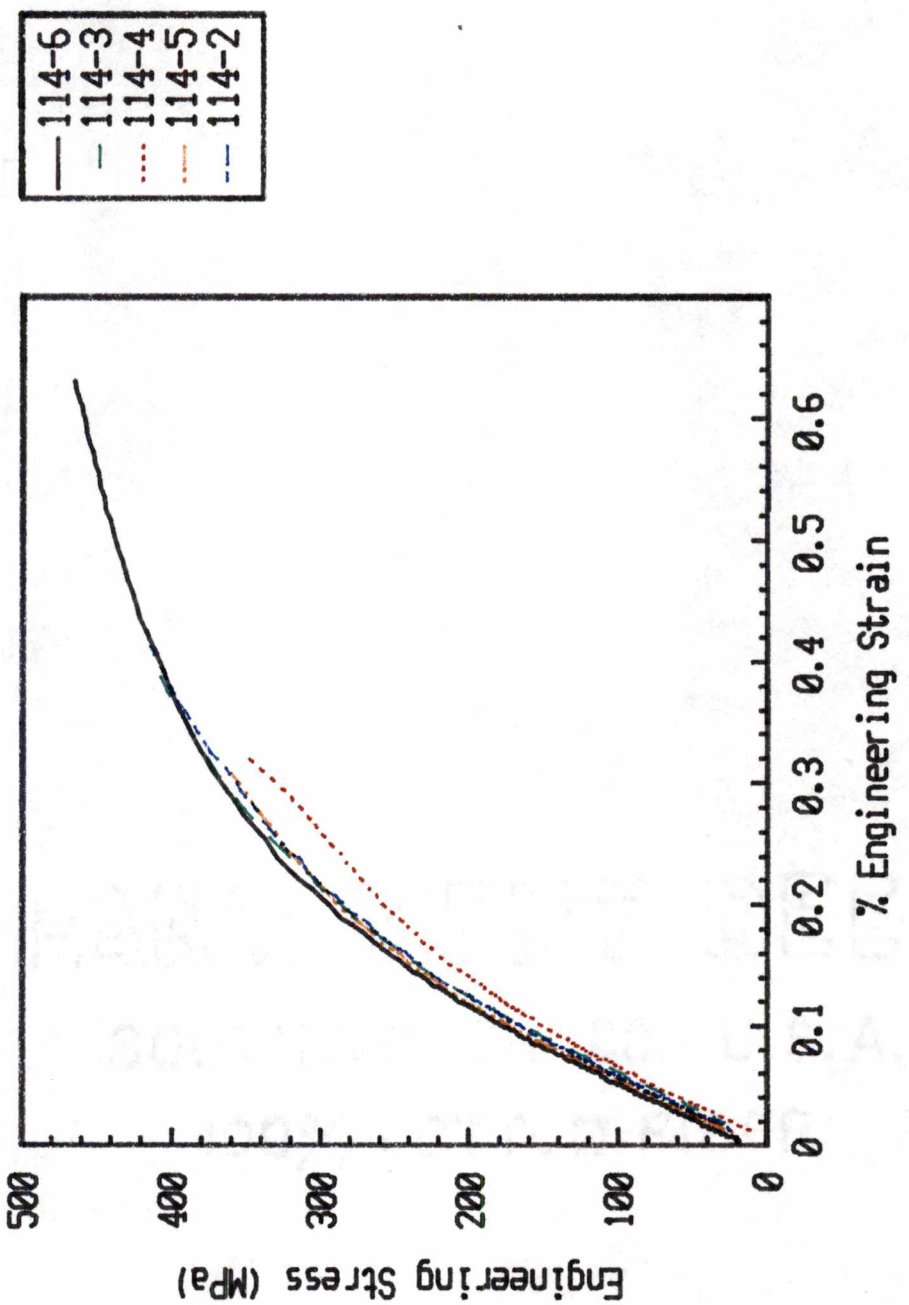


Figure 54. Engineering Stress (MPa) versus Percent Engineering Strain for Four Point Bending of Ti-52/Al-48. Strain Measured via Strain Gages.

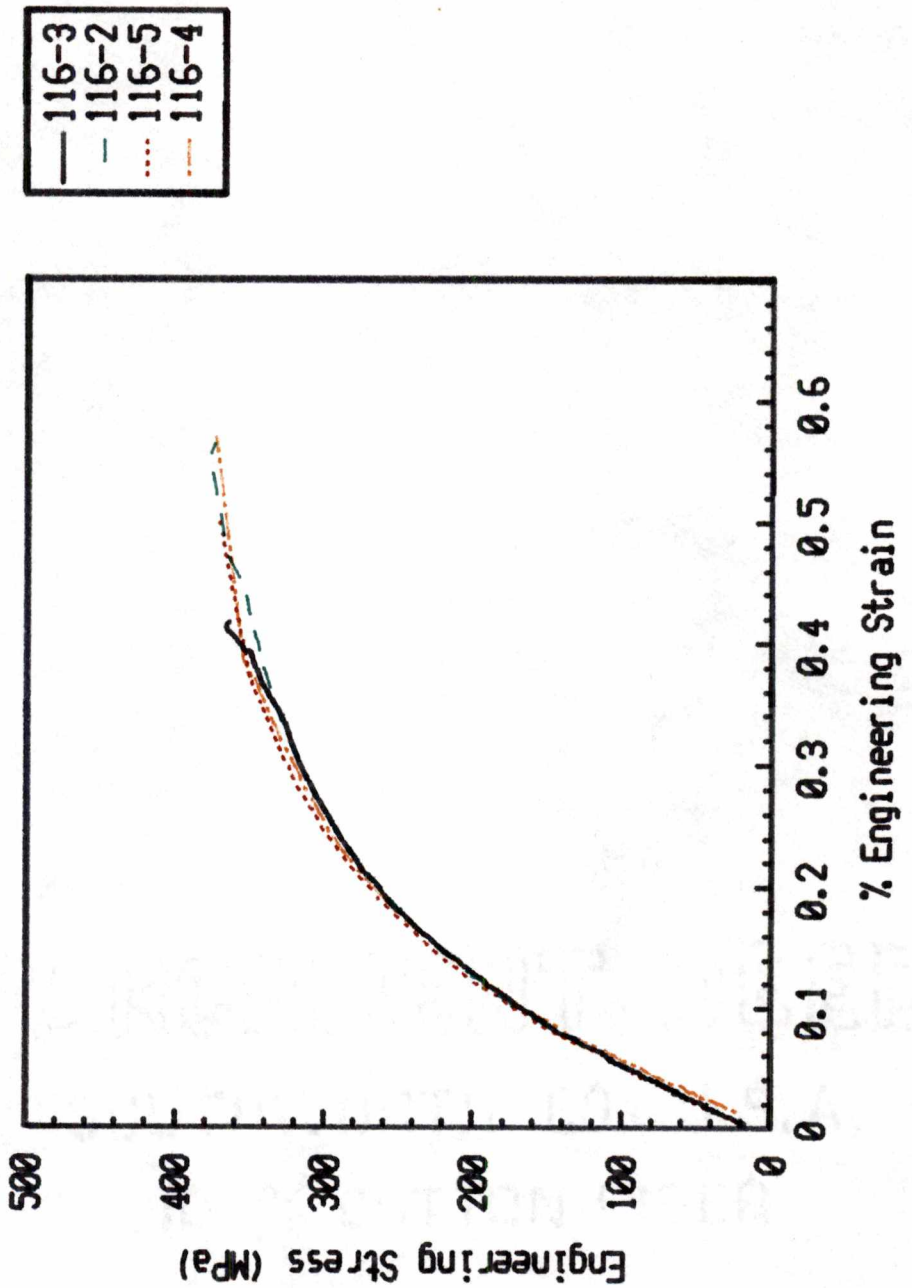


Figure 55. Engineering Stress (MPa) versus Percent Engineering Strain for Four Point Bending of Ti-49.5/Al-49.5/Cr-1. Strain Measured via Strain Gages.

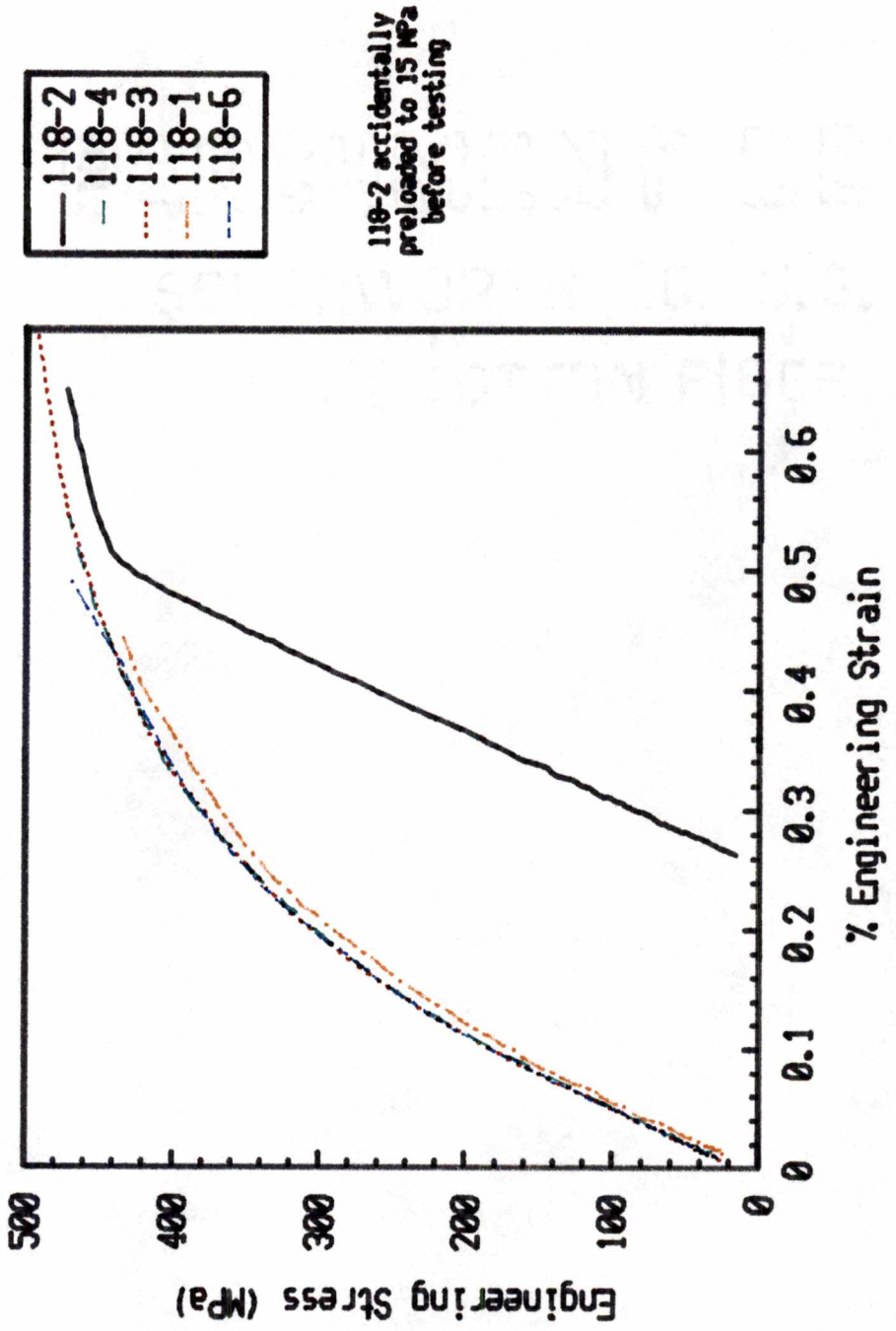


Figure 56. Engineering Stress (MPa) versus Percent Engineering Strain for Four Point Bending of Ti-48.5/Al-48.5/Cr-1/Mn-2. Strain Measured via Strain Gages.

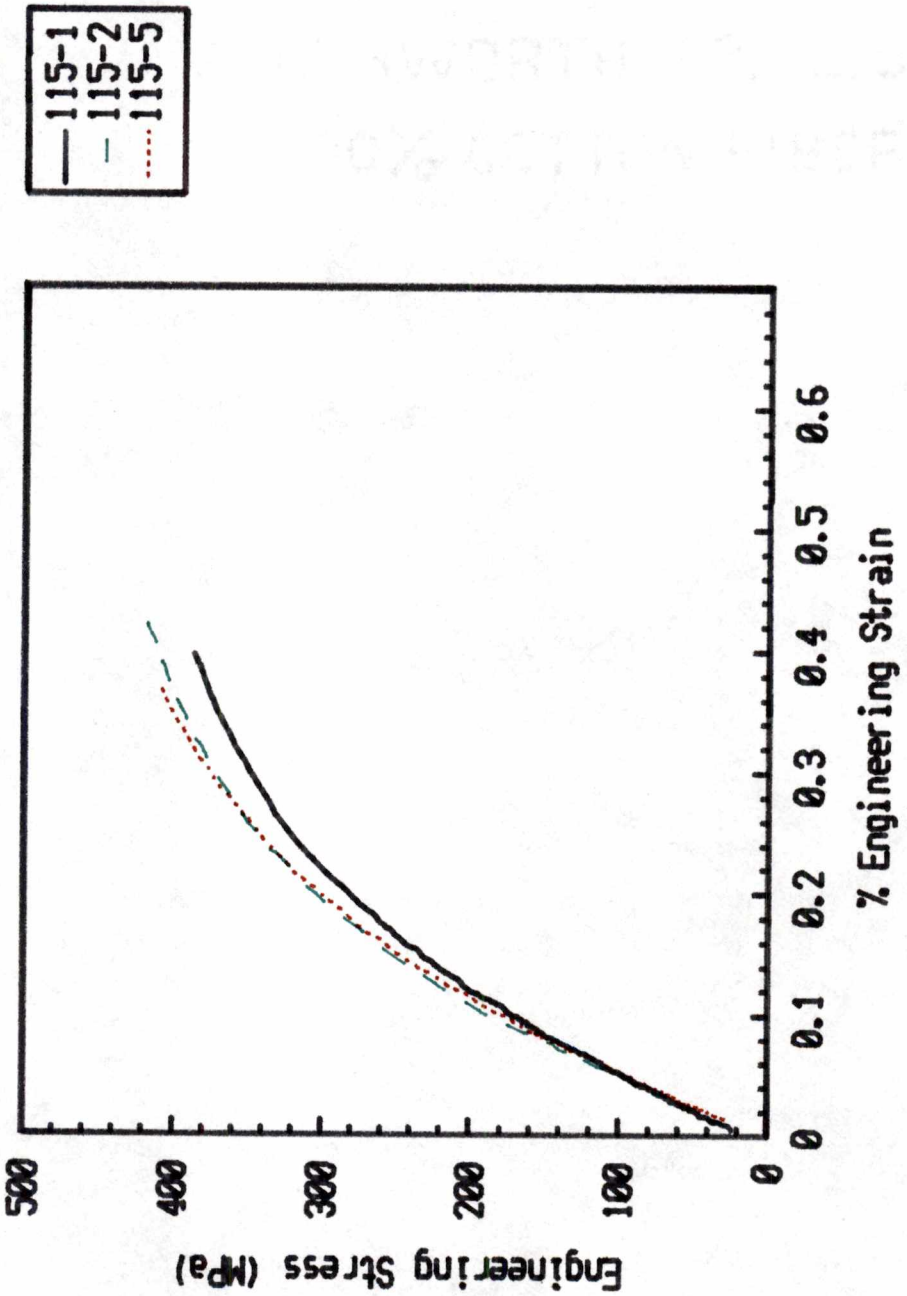


Figure 57. Engineering Stress (MPa) versus Percent Engineering Strain for Four Point Bending of Ti-48.5/Al-49.5/Cr-1/Zr-1. Strain Measured via Strain Gages.

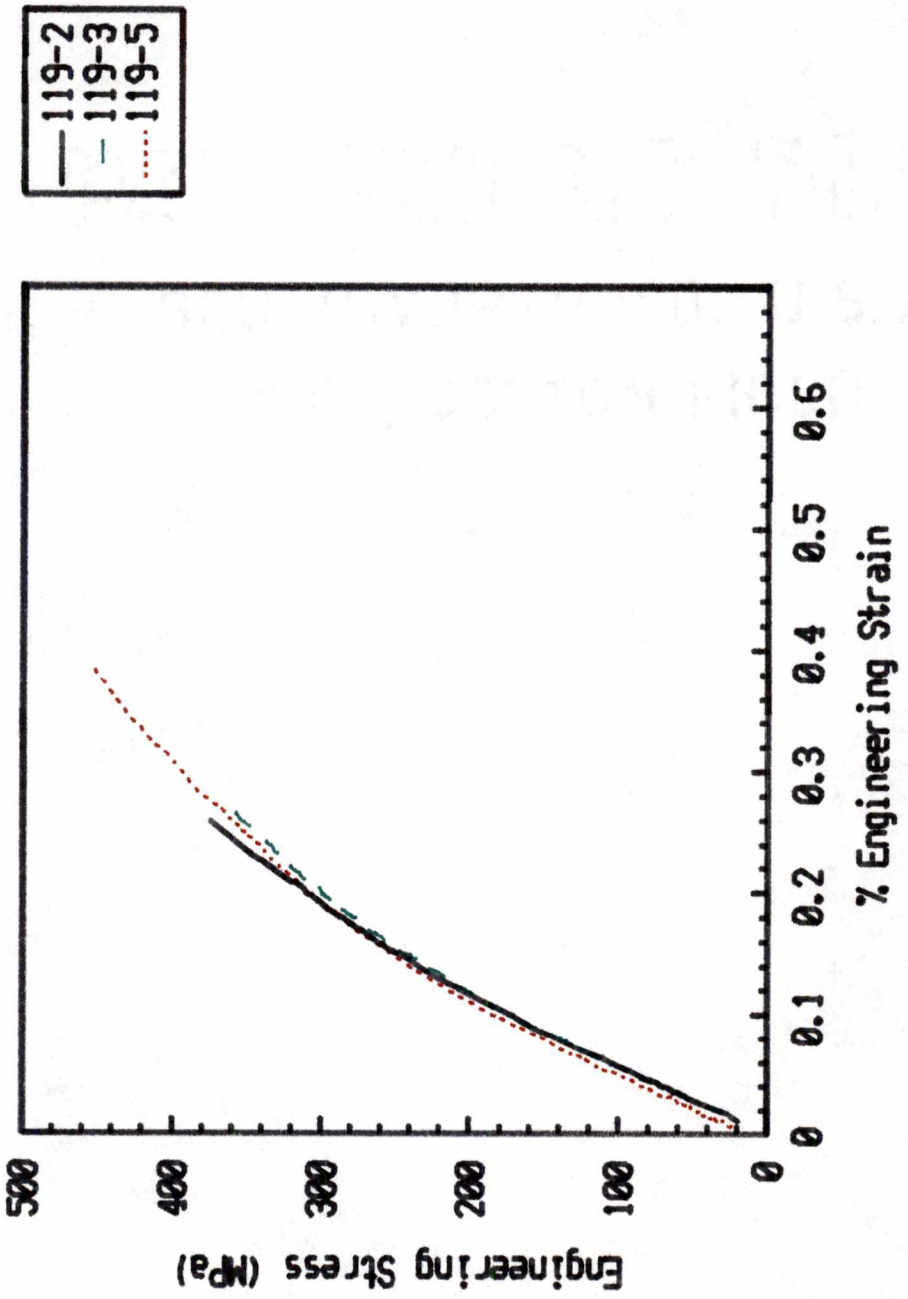


Figure 58. Engineering Stress (MPa) versus Percent Engineering Strain for Four Point Bending of Ti-48/Al-48/Mn-2/Zr-2. Strain Measured via Strain Gages.

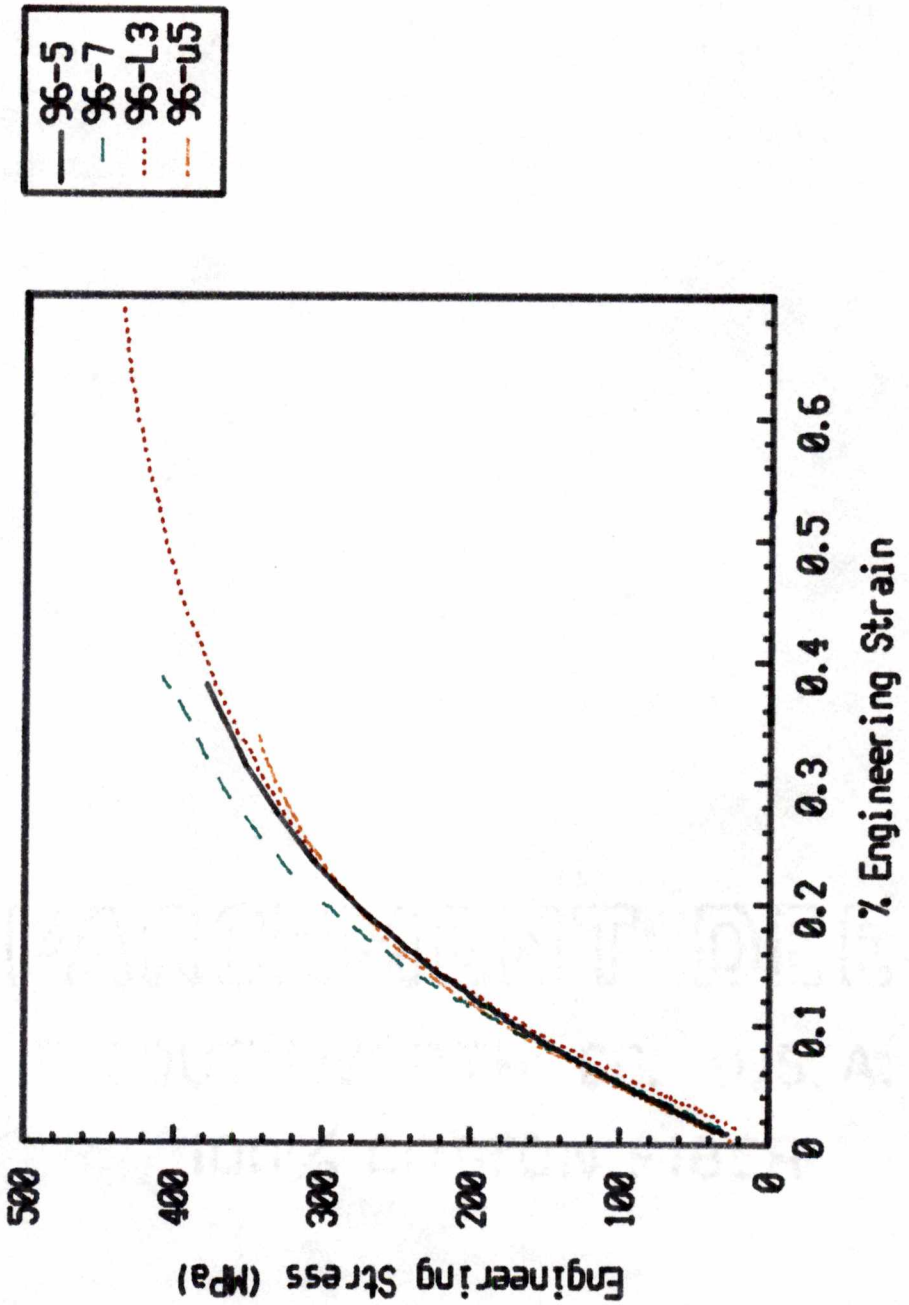


Figure 59. Engineering Stress (MPa) versus Percent Engineering Strain for Four Point Bending of Ti-48.5/Al-48.5/Ga-2/Mn-2. Strain Measured via Strain Gages.

VITA

Robert Reviere was born in Memphis, Tennessee on January 24, 1963. At the age of three, his family and he moved to Greeneville, Tennessee, where he received his education prior to college. In September of 1981 he entered the University of Tennessee as a Chemical Engineering major. After co-oping several quarters with Olin Chemical in Charleston, Tennessee, he changed his major to Metallurgical Engineering and also changed his co-op assignment to TRW in Rogersville, Tennessee.

In June of 1986, he received a Bachelor of Science degree in Metallurgical Engineering. That same month he began study toward a Master's degree in the same field and completed this in August 1988. The following Fall semester he began a Ph. D. program in Metallurgical Engineering at the University of Tennessee. In December 1992 this degree was awarded. In January of 1993, he started work as a post doctorate fellow at the *Max Planck Institut fur Eisenforschung* in Dusseldorf, Germany.

Publications:

Reviere R., Oliver B., and Bruns D.; Mat. Manuf. Proc.,4 (1), 103-131, (1989).

Chen X., Reviere R., Oliver B., Brooks C.R.; Scripta Met. et. Mat., 27, 45-49, (1992).

Reviere R., Noebe R., Oliver B.; Mat. Let., 14, 149-155, (1992).

Whittenberger J., Reviere R., Noebe R., Oliver B.; Scripta Met. et Mat., 26, 987-992, (1992).

Johnson D., Joslin, S., Reviere R., Oliver B.; "Containerless Automated

Processing of Intermetallic Compounds and Composites", ASM/TMS Proceedings, Chicago, IL., (1992).